Di-J/ψ Studies, Level 3 Tracking and the DØ Run IIb Upgrade

Philip John Vint

Imperial College London

A thesis submitted for the degree of
Doctor of Philosophy
of the University of London
and the Diploma of Imperial College.

February, 2010

Di-J/ψ Studies, Level 3 Tracking and the DØ Run IIb Upgrade

Philip John Vint
Imperial College London

February, 2010

ABSTRACT

The DØ detector underwent an upgrade to its silicon vertex detector and triggering systems during the transition from Run IIa to Run IIb to maximize its ability to fully exploit Run II at the Fermilab Tevatron. This thesis describes improvements made to the tracking and vertexing algorithms used by the high level trigger in both Run IIa and Run IIb, as well as a search for resonant di-J/ψ states using both Run IIa and Run IIb data.

Improvements made to the tracking and vertexing algorithms during Run IIa included the optimization of the existing tracking software to reduce overall processing time and the certification and testing of a new software release. Upgrades made to the high level trigger for Run IIb included the development of a new tracking algorithm and the inclusion of the new Layer 0 silicon detector into the existing software. The integration of Layer 0 into the high level trigger has led to an improvement in the overall impact parameter resolution for tracks of $\sim$50%. The development of a new parameterization method for finding the error associated to the impact parameter of tracks returned by the high level tracking algorithm, in association with the inclusion of Layer 0, has led to improvements in vertex resolution of $\sim$4.5 μm.

A previous search in the di-J/ψ channel revealed a unpredicted resonance at $\sim$13.7 GeV/c^2. A confirmation analysis is presented using 2.8 fb^{-1} of data and two different approaches to cuts. No significant excess is seen in the di-J/ψ mass spectrum.

Acknowledgements

I would like to thank...

Rick Jesik and Gavin Davies for being my supervisors and for all their help, advice and friendship.

Per Jonsson for his friendship, advice, help on Level 3 matters and for proof reading my Level 3 chapters.

The Imperial College DØ group, both past and present, for all their help and advice over the years.

Anyone else at Imperial or Fermilab who helped me with my thesis.

My parents for sticking by me, putting me up whenever I needed a roof over my head and for encouraging me when I was down about it all.

The rest of my family for always being there for me when I needed them.

My friends on both sides of the Atlantic for being there for me, and distracting me from working with offerings of beer, chat and games. A special thank you goes out to Mike, Phil, Mark O and Roy for putting up with me as a flatmate over the past few years.

Sneha for helping me though it all and being with me for the past 3 years. Without her help, guidance and love I don't know where I'd be right now.

Contents

List of Figures

List of Tables

Preface

This thesis describes work performed by the author as a member of the DØ Collaboration on the DØ experiment between February 2005 and September 2008, taking in both the Run IIa and Run IIb running periods. The work comprised of three main areas: improvements and developments to the Run IIa Level 3 online triggering software, developments and integration of the Level 3 software relating to readout and use of the Layer 0 detector in Run IIb, and a search into the di-J/ψ mass spectrum.

The author's work in the Level 3 trigger algorithms group has been mostly based around improving and helping to maintain the tracking and vertexing algorithms, and the associated Level 3 tools for those algorithms. Work on Level 3 began with the author helping to reduce the tracking processing time on the existing online Level release, p16. Through investigation of the usefulness of the dead fibre file and of the existing track cuts used in the trigger list, large timing savings were made for a minimal loss in efficiency. This was followed up by a full certification of the tracking and vertexing software for the next release of Level 3, p17.

p17 ran online until the end of Run IIa in 2006, when the DØ Run IIb upgrade took place. This upgrade involved, amongst other things, the installation of a new silicon sub-detector, Layer 0, and its integration into the existing silicon readout systems, as well as the design and implementation of new Level 3 tracking software to replace the ageing and time consuming Run IIa algorithms. The new Run IIb Level 3 tracking software, `L3TCFTTrack`, is at least as good at track finding as its predecessor whilst only requiring a fraction of the processing time of the Run IIa algorithms. The author's work on the new software involved in-depth studies of the tracking

performance, in particular with respect to improving the impact resolution, and helping to find and identify potential problems that could occur once the software went online. Good track impact parameter errors are required to ensure that the vertexing algorithms work correctly with the new tracking algorithms. The author led the effort to obtain these errors by parameterizing them in terms of the number of silicon hits and in terms of p_{scat} (transverse track momentum, p_T, modified by the stereo pitch angle of the track). In addition, the author led the integration of Layer 0 into the existing Level 3 silicon readout software, `L3TSMTUnpack`, and certified it for use online, and derived a new set of track impact parameter errors in conjunction with the Layer 0 changes. Though the Layer 0 changes were completed well in advance of the detector installation, they would not be placed online until the Run IIb tracking software had been fully validated and was fully understood under known conditions.

The author initially joined the DØ B physics group to help work on the B_s mixing measurement in the hadronic decay mode $B_s \to D_s^- \pi^+$, where work proceeded on producing a more accurate Monte Carlo sample for use in the analysis, and on expanding the amount of data used in the analysis. However, this was short lived, with measurements of B_s mixing by both the DØ [1] and CDF [2] collaborations, and the author was soon working on an analysis of the di-J/ψ mass spectrum. The di-J/ψ channel is important as it is a possible search channel for various new phenomena and also for validating theories about fragmentation production in QCD processes. This work was also conducted in order to confirm or deny a previously result obtained by another DØ collaborator. By searching for two J/ψs coming from the same primary vertex, where each has decayed to two muons, a di-J/ψ object is obtained and after analyzing 2.8 fb^{-1} of data, a di-J/ψ mass spectra is obtained which is used to question the previously obtained result. The di-J/ψ analysis was conducted whilst blind to the final di-J/ψ mass, and went through two iterations before a result was presented. The second iteration was deemed necessary after the first set of analysis cuts were found to be too tight.

The thesis has the following structure:

- Chapter 1 is a brief review of the Standard Model and Higgs theory, quark mixing and B_s and B_d mixing, charmonium and resonant and non-resonant di-J/ψ production mechanisms.

- Chapter 2 briefly describes the Fermilab accelerator complex and the DØ detector in both Run IIa and Run IIb.

- Chapter 3 introduces the various Run IIa tracking and vertexing algorithms relevant to the work described in this thesis and covers work performed in order to help reduce the overall Level 3 processing time in the p16 release. It also describes in detail the p17 certification performed on the tracking and vertexing tools.

- Chapter 4 describes the new Run IIb Level 3 tracking software, `L3TCFTTrack`, and demonstrates its performance against the older Run IIa tracking algorithms. It also details the parameterization process used to derive a new set of track impact parameter errors that are used to calculate a primary vertex for an event. Also detailed are the certification and testing processes used to validate the new errors.

- Chapter 5 describes the changes made to the existing Level 3 software to incorporate the new silicon detector, Layer 0. This chapter also covers the new track impact parameter error parameterization that was undertaken once the Layer 0 changes were incorporated into the tracking systems. The certification of both the Layer 0 changes and the new error parameterization is also covered here.

- Chapter 6 details both iterations of the author's di-J/ψ analysis. A comparison of the final iteration of the di-J/ψ analysis and the original analysis is then presented and conclusions obtained.

- Chapter 7 provides a summary and outlook.

Chapter 1

The Standard Model and di-J/ψ production

1.1 Preface

This chapter introduces the Standard Model (SM) and its role in describing fundamental physics as it is known today. The SM provides experimentally testable theories about the properties of fermions and three of the four forces and their associated gauge bosons. Fermion and boson masses are accounted for in the SM through the Higgs mechanism. Discussion of the SM is followed by a brief overview of the CKM matrix and its importance in quark mixing, and by an overview of B_d and B_s meson mixing. A more complete description of the SM can be found in [3, 4].

Details of charmonium ($c\overline{c}$) production follow, looking in detail at direct QCD production, fragmentation production through the color singlet and color octet models and $c\overline{c}$ production through the decay of B mesons. This is followed by details of di-J/ψ production, looking at both resonant and non-resonant di-J/ψ production, and how the di-J/ψ can be used to test both SM and beyond the SM theories.

1.2 The Standard Model

The Standard Model is currently the best description of the fundamental physics that underlies three of the four interactions and the fundamental particles which

undergo those interactions. Those three forces are the electromagnetic, the weak and the strong nuclear forces. Fundamental particles are split into half-spin particles (fermions), and their corresponding antiparticles, and integer spin particles (bosons). The Standard Model is, and has been, very successful. Its predictions agree with experimental measurements to a very high degree of accuracy.

The fermions are split into leptons and quarks which are the fundamental building blocks of matter, whilst the bosons are the force carriers, known as gauge bosons. The three forces the SM describes can be split into two main components: Quantum Chromodynamics (QCD), which describes the strong force and its gauge boson the gluons; and Electroweak (EW) [5], which describes the unison of the weak force, and its gauge bosons the $W^{\pm}$ and the Z^0, and the electromagnetic force, in the form of Quantum Electrodynamics (QED) and its gauge boson the photon, γ.

There are currently 12 known varieties of fermions, each with its own corresponding antiparticle. The distinction of whether the fermions are quarks or leptons is decided by the type of charge they carry. The currently known quarks, in ascending mass order, are the up, down, strange, charm, bottom and top quarks, whilst there are three different types of lepton - electron, muon and tau - each with its own corresponding neutrino. Both the quarks and the leptons are further grouped together to form 3 generations. Between the generations corresponding particles exhibit similar physical properties to one another, for example the d, s and b quarks all have a charge of $-\frac{1}{3}$, whilst the u, c and t quarks all have a charge of $+\frac{2}{3}$. The masses of the fermions in each generation are higher than the previous generation, and only the particles in the first generation are stable, making up all visible matter within the Universe. The higher mass fermions decay with a short half-life into lower mass fermions. Further details on the properties of the twelve fermions can be seen in table 1.1.

In addition to electrical charge and weak isospin, quarks also carry color charge (red, green and blue, and the associated anticolors) and interact via the strong force. Due to color confinement from the strong force, quarks are never observed on their own, only in color neutral confined states known as hadrons. Hadrons contain either

Generation	Leptons			Quarks		
	Name	Charge	Mass (MeV)	Name	Charge	Mass (MeV)
I	e	-1	$0.511\pm1.3\text{x}10^{-9}$	u	$+\frac{2}{3}$	1.5 - 3.3
	ν_e	0	$< 2\text{x}10^{-6}$	d	$-\frac{1}{3}$	3.5 - 6.0
II	μ	-1	$105.7\pm4\text{x}10^{-7}$	c	$+\frac{2}{3}$	$1.27^{+0.07}_{-0.11}\text{x}10^3$
	ν_μ	0	$< 2\text{x}10^{-6}$	s	$-\frac{1}{3}$	104^{+26}_{-34}
III	τ	-1	$1776\pm1.7\text{x}10^{-1}$	t	$+\frac{2}{3}$	173.1 ± 1.3 x 10^3 [6]
	ν_τ	0	$< 2\text{x}10^{-6}$	b	$-\frac{1}{3}$	$4.20^{+0.17}_{-0.07}\text{x}10^3$

Table 1.1: Table showing the 12 leptons and quarks that make up the Standard Model. They are arranged by generations and give each particle's mass and charge. Masses are from [7] except where otherwise labelled.

three quarks, known as a baryon, or a quark-antiquark pair, known as a meson. In addition there have been recent particle discoveries which could be more exotic forms of matter such as pentaquarks, glueballs and quark-gluon hybrids. It should be noted though quarks are the only fermions that can interact through the strong force, but they are not limited to only that interaction and also interact through the electroweak force.

The connection between symmetries and conservation laws has been key to the development of physics throughout history and the formulation of the SM is no exception. As in classical mechanics, the invariance of the SM under a group of transformations (symmetry) places tight constraints on the physics it can describe, and leads to the existence of one or more conserved quantities associated to the given transformations; this is known as Noether's theorem [8]. This principle has led to the use of local gauge invariance to produce the current SM which has a $SU(3)_C \otimes SU(2)_L \otimes U(1)_Y$ gauge symmetry. The $SU(2)_L \otimes U(1)_Y$ symmetry comes from EW theory and it is describing the invariance of weak and electromagnetic processes under weak isospin ($SU(2)_L$) and weak hypercharge ($U(1)_Y$) transformations. Isospin, I, is analogous to spin but for hadrons and, like spin, has isospin projection, I_3, to differentiate particles with the same isospin state. For example, the three pions, π^+, π^0 and π^-, are all part of the same isospin triplet and have I_3 values of +1, 0 and -1 respectively. Hypercharge, Y, relates the electrical charge, Q, and I_3 component together through the relation $Y = 2(Q - I_3)$. Hypercharge represents the

mixing of QED and weak forces to produce the Z and the γ. The $SU(3)_C$ symmetry describes strong processes taking place through color charge transformations.

As previously mentioned, the gauge bosons are the force carriers in the Standard Model, details of which can be seen in table 1.2. Whilst the photon and gluons are non-massive, the $W^{\pm}$ and Z^0 gauge bosons do have mass. Unfortunately the Standard Model does not allow for massive gauge bosons whilst still remaining gauge invariant. So to obtain masses for the W and Z bosons a new mechanism known as spontaneous symmetry breaking is used, and in particular the Higgs mechanism [9, 10, 11].

Gauge Boson	Force Mediated	Charge	Mass (GeV)	Relative Strength
Photon, γ	Electromagnetic Force	0	0	$\sim 10^{-2}$
$W^{\pm}$	Weak Force	$\pm$ 1	80.398 $\pm$ 0.025	$\sim 10^{-9}$
Z^0	Weak Force	0	91.1876 $\pm$ 0.0021	$\sim 10^{-9}$
Gluon, g	Strong Force	0	0	1

Table 1.2: Table showing the gauge boson properties for the three forces integrated into the Standard Model. Relative force strength estimates are scaled relative to the strong force, and are assuming a low interaction energy. Values taken from [7].

Spontaneous symmetry breaking works by introducing a new self interacting scalar field, which is gauge invariant under transformations similar to those that can be used in QED. The scalar field, ϕ, incorporates a potential term, $V(\phi)$, which is dependent upon a coupling term, λ, and on a mass term, μ, or more accurately on μ^2, where μ^2 can be either positive or negative. If μ^2 is positive, then the minimum of $V(\phi)$ is at zero and the potential merely describes a scalar field with mass μ. However, if μ^2 is negative then $V(\phi)$ has a local maximum at zero and a set of minima located at a v, where v is the vacuum expectation value. This is illustrated in figure 1.1.

A perturbative expansion, which allows for further predictions to be made from the model, must be performed around the minimum. For the case where μ^2 is negative this means performing the expansion around v, and by doing so the symmetry is broken. One consequence of this symmetry breaking is that the final Lagrangian produced contains an unphysical term, and hence cannot be used to describe a

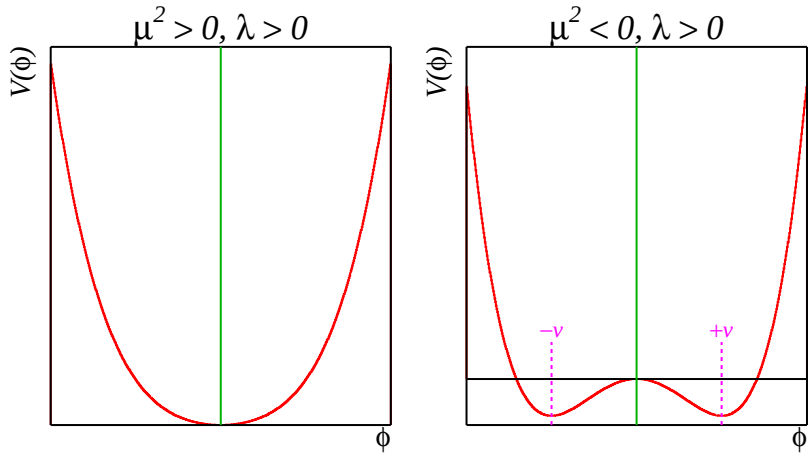

Figure 1.1: The Higgs potential, $V(\phi)$, for both positive and negative values of μ^2. When $\mu^2 < 0$, the minima of the potential lie at v, whilst a local maximum lies at $V(\phi) = 0$ [12].

physical situation. However, through the use of the Higgs mechanism the unphysical term is replaced by the Higgs field, h. Interactions of h with the electroweak model leads to massless photons but massive $W^{\pm}$ and Z^0 bosons, thus adding mass into the Standard Model. Similarly, interactions between the fermions and h gives mass to the quarks and leptons in the Standard Model.

1.3 The CKM matrix

Couplings between the fermions and the Higgs field allow for masses to be generated in electroweak interactions. However, the physical mass eigenstates are not equal to the weak eigenstates. The weak eigenstates are rotated versions of the physical mass eigenstates. These rotations allow for inter-generation mixing between the quarks through terms like $V_u^{\dagger}V_d$ which details the flavor changing process between a up type quark and a down type quark. The relevant flavor changing processes are detailed in the unitary Cabibbo-Kobayashi-Maskawa (CKM) matrix which is shown in equation 1.1 [13]. Equation 1.1 also shows the Wolfenstein parameterization of the CKM matrix [14]. This redefines each of the amplitudes in terms of 4 real parameters, λ, A, ρ and η.

$$V_{CKM} = \begin{pmatrix} V_{ud} & V_{us} & V_{ub} \\ V_{cd} & V_{cs} & V_{cb} \\ V_{td} & V_{ts} & V_{tb} \end{pmatrix} = \begin{pmatrix} 1-\frac{\lambda^2}{2} & \lambda & A\lambda^3(\rho - i\eta) \\ -\lambda & 1-\frac{\lambda^2}{2} & A\lambda^2 \\ A\lambda^3(1-\rho-i\eta) & -A\lambda^2 & 1 \end{pmatrix} + \mathcal{O}(\lambda^4) \tag{1.1}$$

Where V_{ij} represents the amplitude of the flavor changing process $u_i \rightarrow d_j$, and i and j are indices over the up and down type quarks. Current experimental measurements place the measurements for each of the matrix elements can be seen in equation 1.2 [7].

$$V_{CKM} = \begin{pmatrix} 0.97419 \pm 0.00022 & 0.2257 \pm 0.0010 & 0.00359 \pm 0.00016 \\ 0.2256 \pm 0.0010 & 0.97334 \pm 0.00023 & 0.0415^{+0.0010}_{-0.0011} \\ 0.00874^{+0.00026}_{-0.00037} & 0.0407 \pm 0.0010 & 0.999133^{+0.000044}_{-0.000043} \end{pmatrix} \tag{1.2}$$

The requirement that the CKM matrix is unitary requires that the rows and columns within the matrix are orthonormal. This leads to six expressions representing the said orthogonality which can further be represented as triangles in the complex plane. The most commonly used expression is:

$$V_{ud}V_{ub}^* + V_{cd}V_{cb}^* + V_{td}V_{tb}^* = 0 \tag{1.3}$$

The resultant triangle can be seen in figure 1.2 and is known as the'unitary triangle'. If the SM is consistent then the sum of the angles within the triangle should be 180 °.

1.3.1 B_d and B_s mixing

The Standard Model allows for mixing of B_i - $\overline{B_i}$, where $i = d, s$ to occur through second order flavor changing diagrams, such as those shown in figure 1.3. This causes oscillations between the two flavor eigenstates, B_i and $\overline{B_i}$, since an initially produced B_i will evolve into a superposition of both the B_i and $\overline{B_i}$ eigenstates.

The time evolution of an initially tagged B_i will change as a function of two 2x2 matrices, the mass, M_i and the decay, Γ_i. Mixing occurs when the matrices M_i and

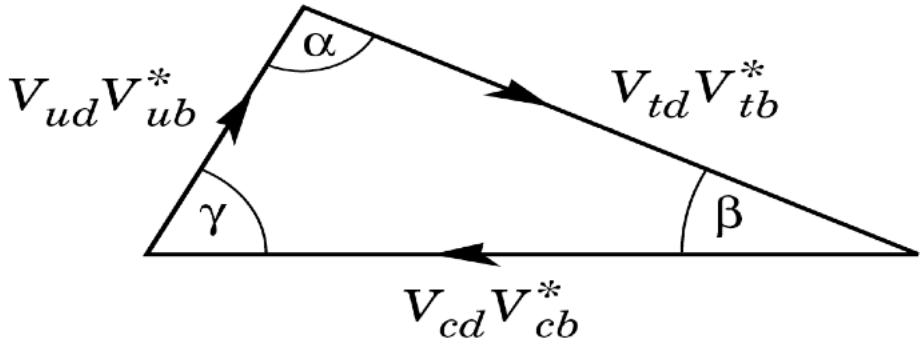

Figure 1.2: The Unitary Triangle. Each of the sides represents one of the terms shown in equation 1.3. If the Standard Model is consistent then the sum of the angles will equal 180 ° [7].

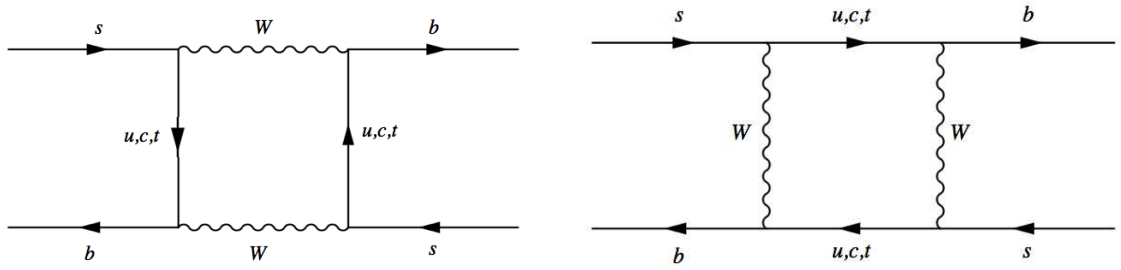

Figure 1.3: Standard Model Feynman diagrams for B_s mixing. The B_s is always on the left of the diagrams, whilst the $\overline{B_s}$ is always on the right. The exchange of a t quark dominates. The diagrams for B_d mixing are analogous to this.

Γ_i have off diagonal elements and the mass eigenstates are not equal to the flavor eigenstates. The superposition of the B_i and $\overline{B_i}$ states leads to interference effects between the two states.

The current world averages for mixing in the B_s and B_d systems are (from [2] and [15] respectively):

$$\Delta M_s = 17.7 \pm 0.12\text{ps}^{-1*} \qquad \Delta M_d = 0.507 \pm 0.005\text{ps}^{-1} \tag{1.4}$$

There are two main ways of observing B_i mixing, semi-leptonically and hadronically. The semi-leptonic mode suffers from the presence of a neutrino in the decay and hence the B_i decay cannot be fully reconstructed. The hadronic decay of B_i, on the other hand, can be fully reconstructed and hence provides better resolution for ΔM_i. However, the branching fraction for this decay is small (for example the branching fraction for the decay $B_s \rightarrow D_s^- \pi^+$ is 3.3 $\pm$ 0.5 x 10^{-3} [7]), and so the results for these decays will be limited by statistics. Accurate measurement of both ΔM_s and ΔM_d can be used to help constrain the unitary triangle, and hence can be used as a such for new physics. This is due to the ratio $\Delta M_s / \Delta M_d$ providing a direct measurement of $|V_{td}|$ [13].

1.4 Charmonium production at the Tevatron

Charmonium ($c\overline{c}$) production from $p\overline{p}$ collisions is dominated by two main processes, the direct production of a colorless $c\overline{c}$ pair and the decay of a B meson into a ψ meson, of which J/ψ is the lowest spin state in the ψ system. Both of these processes are covered below. Figure 1.4 shows the charmonium mass spectrum. This figure shows the different masses split by the spatial portion of the angular momentum wave function. The S, P, D and F waves are analogous to those used in atomic physics with, for example, the S wave representing the $L = 0$ and $J = 0$ or 1 states and the P wave designating those with $L = 1$.

*The measurement of ΔM_s at the Tevatron occurred during the time of this thesis work.

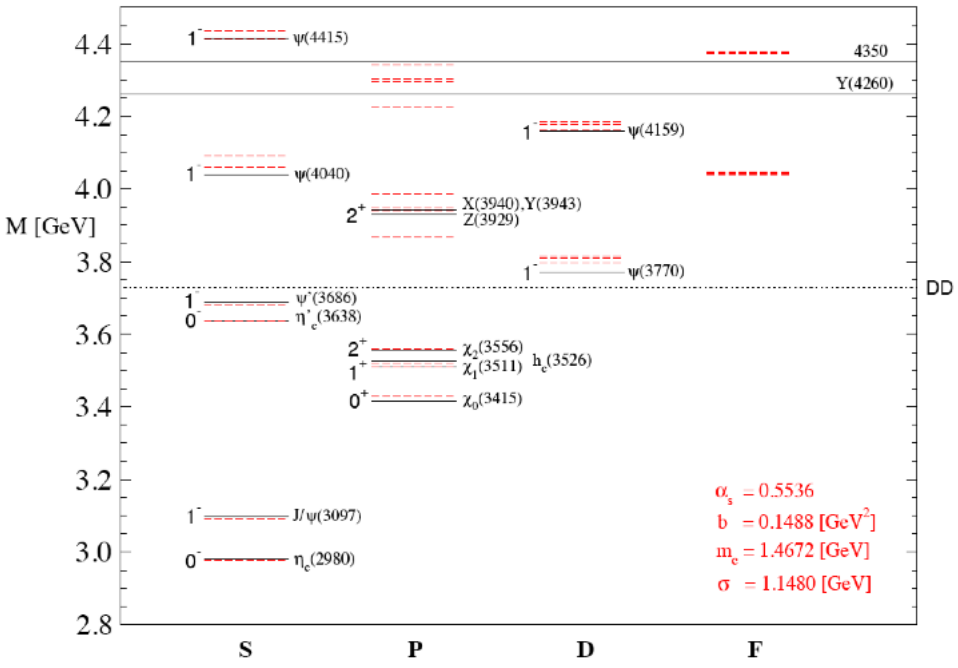

Figure 1.4: The charmonium mass spectrum. Experimentally measured masses are indicated by solid lines whilst theoretical predictions are indicated by dashed lines. The horizontal line at 3.73 GeV indicates the mass threshold where charmonium will decay to $D\overline{D}$ final states [16].

1.4.1 Direct production

The leading order diagram for direct ψ production can be seen in figure 1.5. Here the $c\bar{c}$ quarks are produced in a color-singlet state, and all stages of the diagram, except the final hadronization of the quarks into a $c\bar{c}$ meson, can be calculated. A similar production mechanism which contributes only to J/ψ production also exists. This involves the $c\bar{c}$ pair producing a χ_c state, which can then decay into a J/ψ and a photon. All currently known χ_c states have masses below that of the $\psi(2S)$ state, or above the threshold for decay into charmed mesons, so this mechanism benefits J/ψ production only. The ψ states can decay to a lepton-antilepton pair, and this clean signal provides critical tests of QCD and can be used for calibration and testing purposes, and also provides for an important handle for many results in High Energy Physics.

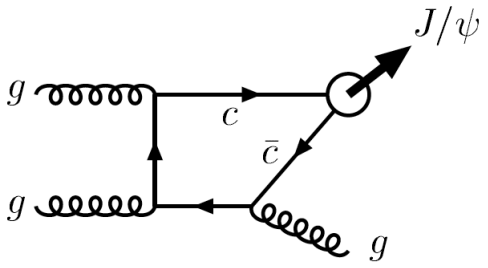

Figure 1.5: Leading order Feynman diagram for $c\bar{c}$ production through gluon-gluon fusion. In this case the $c\bar{c}$ hadronizes into a J/ψ.

The cross-section for ψ state production was measured to be much greater than the predicted cross-section from processes like those shown in figure 1.5 taking into account ψ production from B meson decays and J/ψ production from χ_c decays [17]. The ψ cross section for direct production can be enhanced through fragmentation through the color singlet [18, 19] and color octet production mechanisms. Under normal circumstances the process shown in figure 1.5 would dominate $c\bar{c}$ production ($\sim \mathcal{O}(\alpha_s^3)$, where α_s is the strong coupling constant), and fragmentation effects (as seen in figure 1.6) would be minimal ($\sim \mathcal{O}(\alpha_s^5)$). However, if the ψ has a large transverse momentum, $p_T \gg m_\psi$, then the diagram is enhanced by a factor of $(p_T/m_\psi)^2$, and given a high enough p_T the fragmentation effects will dominate ψ

production [18, 19]. This process is known as the color singlet model (CSM), as the fragmentation process produces a color singlet $c\bar{c}$ pair.

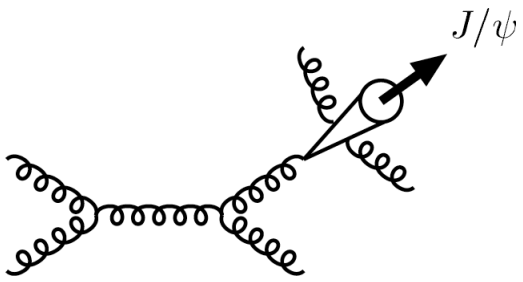

Figure 1.6: Leading order Feynman diagram for ψ production through fragmentation production using the color singlet model.

It is also possible for the fragmentation process to produce a color octet $c\bar{c}$ pair through a process known as the color octet model (COM). This theory uses non-relativistic QCD (NRQCD) [20], which is an effective potential model inspired by Heavy Quark Effective Theory (HQET) [21, 22, 23, 24, 25]. This theory is based on the fact that the quarks inside a charmonium state will have a relatively slow speed, $v_c^2 \approx 0.25$, and thus means that the color-octet diagram is dependent upon both α_s and v_c. Terms of higher order in α_s may be of lower order in v_c and vice versa, so that which terms dominate the cross section depends upon the power of both α_s and v_c. Analysis of this mechanism leads to one or more of the gluons radiated from the $c\bar{c}$ pair being removed from the hadronization and being radiated before this stage happens (as shown in figure 1.7). The gluon is treated as being extremely soft and is thus approximated by the gluon carrying no energy, only color charge.

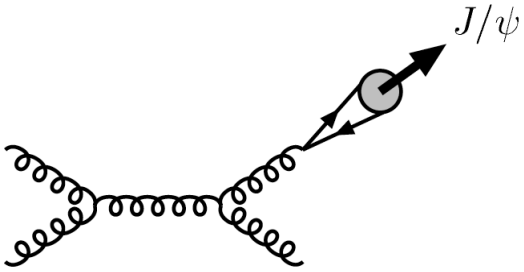

Figure 1.7: Leading order Feynman diagram for ψ production through fragmentation production using the color octet model.

1.4.2 B meson decays

Charmonium production can also come from B meson decays. A b quark is produced from QCD processes, which fragments into a B hadron, which will subsequently decay and can produce a $c\bar{c}$ pair, which can then further become a ψ or χ_c state, as well as other particles. This decay is shown in figure 1.8. The decay of a B hadron into a ψ or χ_c state is suppressed relative to the decay $B \to DX$ however, where X represents all possible daughter particles. This is due to the requirement that the mediating W boson must decay into $\bar{c}s$ in order to produce a ψ or χ_c, whereas the W may decay by all possible modes for the decay $B \to DX$. Also, the requirements that the $\bar{c}$ and the c have the same color charge and be of similar momenta to form a bound state, further suppress this decay. The overall branching ratio for the B decay to produce a J/ψ state is $\mathcal{B}(B \to J/\psi X) = 1.13 \pm 0.07\%$ [7], and to produce a $\psi(2S)$ state it is $\mathcal{B}(B \to \psi(2S)X) = 0.34 \pm 0.05\%$ [7]. Whist a small branching ratio, the clean and simple dimuon signature from the ψ decay make $B \to \psi X$ decays easy to trigger on and important to study.

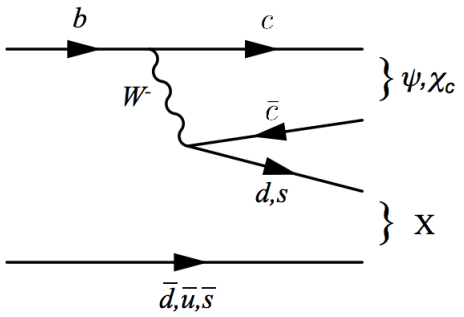

Figure 1.8: Leading order Feynman diagram for the decay of a B meson to a ψ or χ_c state.

1.5 Di-J/ψ production

Di-J/ψ production can be thought of as occurring in two main ways, through non-resonant QCD processes similar to those used for Charmonium production, and through resonant processes such as the decay of an η_b meson. This section will describe both types of di-J/ψ production.

1.5.1 Non-resonant QCD production

Non-resonant QCD processes can produce two J/ψ states instead of one. Similar processes to those described in section 1.4 can also produce a di-J/ψ final state, that is direct QCD production and fragmentation production through the CSM and COM processes. Leading order production mechanisms for di-J/ψ production are shown in figure 1.9.

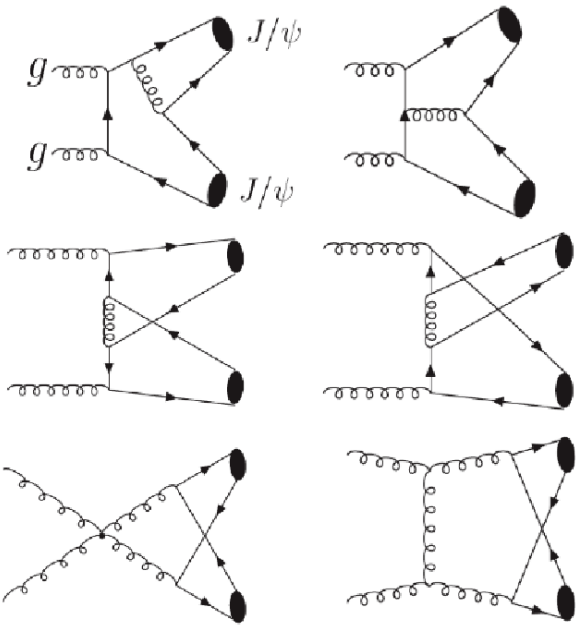

Figure 1.9: Leading order Feynman diagrams for di-J/ψ production in $p\overline{p}$ collisions [26].

The di-J/ψ channel is an important test of the color octet model. The dependence on the p_T of the resultant J/ψ on the cross-section for fragmentation production is different for both the CSM and COM processes, and this can been seen in figure 1.10. This figure shows the theoretical predictions for the di-J/ψ production cross section as a function of p_T, and shows that at high p_T the COM dominates [26]. Although only di-J/ψs are considered here, the model can be extended for other charmonium states, such as $\psi(2S)$ pairs.

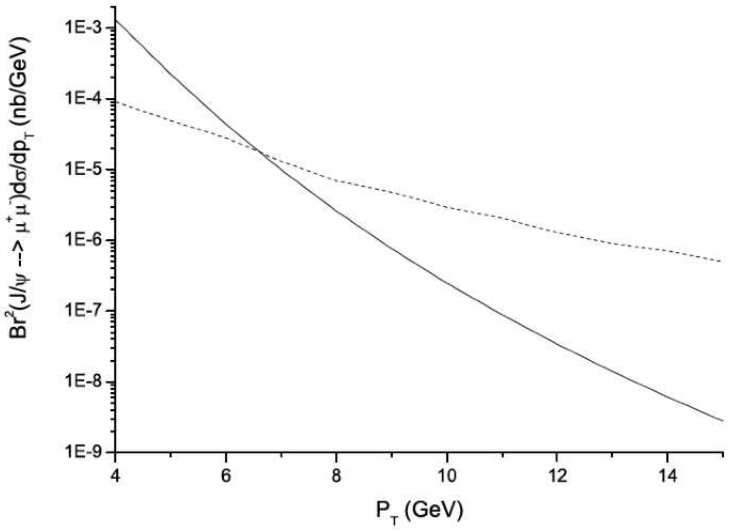

Figure 1.10: The theoretical cross-section for di-J/ψ production versus p_T for both the CSM (solid line) and COM (dashed line), from [26].

1.5.2 Resonant di-J/ψ production

It is also possible for di-J/ψ states to be produced from the radiative decays of other heavier particles, and since a J/ψ can decay to two leptons, specifically to two muons in this case, this makes di-J/ψ production an interesting channel in which to search for new particles.

One such particle that can be searched for using the di-J/ψ channel is the $b\bar{b}$ state $\eta_b(1S)$. Though the η_b has recently been observed by the BaBar collaboration through the decay $\Upsilon(3S) \rightarrow \gamma\eta_b(1S)$ [27] the η_b has yet to be seen at a hadron collider. In a hadronic environment, however, the decay of an $\Upsilon(3S)$ would not be an ideal way to search for evidence of the η_b meson due to larger backgrounds in $p\bar{p}$ collisions. Thus, an alternative strategy for this search is required, the decay of the η_b into a di-J/ψ state. As previously mentioned, the decay of each of the J/ψs into $\mu^+\mu^-$ makes this a possible search channel for the η_b. However, the current branching ratio for the decay $\eta_b \rightarrow J/\psi J/\psi$ has been calculated to be small (between $\sim 10^{-4}$ [28] and $\sim 10^{-8}$ [29]), so a large data sample is required to see this particular decay mode.

The coupling of the Higgs boson to another particle is proportional to the mass of the

latter, thus it is normal to look for Higgs boson decays in the heaviest kinematically allowed particles. However, fits to electroweak parameters favour a low mass SM Higgs such that the mass of the mass of the Higgs, M_H, is $< 2M_W$, where M_W is the W mass [30], and so SM Higgs decays to $b\bar{b}$ and $\tau^+\tau^-$ are dominant. Direct SM Higgs decays to di-J/ψ states, however, are very unlikely given the very small branching ratio this decay will have. Outside of the SM, supersymmetric (SUSY) theories predict the presence of four additional Higgs bosons on top of the Higgs predicted by SM Higgs processes. Although there are many different SUSY theories, NMSSM theory [31] predicts the decay of the lightest neutral CP-even Higgs boson, h to a pair of neutral pseudo-scalar Higgs bosons, a, both with masses $<\sim 10$ GeV. If $M_a > 2M_\tau$, where M_a is the mass of the a and M_τ is the mass of the τ, then the a will decay primarily to $\tau\tau$ pairs, however if M_a is below this threshold then it can decay to $\mu\mu$ pairs. Thus, searches in the 4μ channel [32] around the J/ψ mass could be used to find the h.

The di-J/ψ production mechanisms are very similar to those used for single J/ψ production, and indeed the majority of $c\bar{c}$ states; direct QCD production and fragmentation production (using either the color singlet or color octet models). A study into the di-J/ψ channel can be used to test the validity of the color octet model through examination of the cross-section as a function of p_T, as well as to search for new particles predicted by both the SM and beyond the SM theories. Preliminary di-J/ψ studies are covered in detail in chapter 6 of this thesis.

Chapter 2

The Tevatron and the DØ detector

The accelerator complex at the Fermi National Accelerator Laboratory (Fermilab) located just outside of Chicago, USA, has grown significantly in size and complexity since its inception in 1967. The Tevatron accelerator began colliding 900 GeV proton and antiproton beams in 1985. Run I was undertaken between 1992 and 1996 at a centre of mass energy of 1.8 TeV, with 6 bunches of protons and antiprotons with a bunch spacing of 3500 ns. During Run I DØ collected 120 pb^{-1} of data, resulting in many important results, including the discovery of the top quark [33].

To improve the physics reach of both the accelerator and the detector, a major upgrade was undertaken in preparation for Run II. This included the installation of a new intermediate accelerator, the Main Injector, and an antiproton storage device, the Recycler, as well as significant upgrades to the Tevatron itself. These upgrades allowed for the number of proton and antiproton bunches to each be increased to 36, the bunch spacing decreased to 396 ns and the centre of mass energy increased to 1.96 TeV.

The DØ detector also underwent significant upgrades in preparation for Run II. These included the installation of a new tracking system, consisting of an inner silicon vertex detector and an outer scintillating fibre tracker both surrounded by a 2 T superconducting solenoid, the addition of preshower detectors and an upgrade to the muon system. In addition to this the readout and triggering electronics were

also substantially upgraded to deal with the increased performance of the Tevatron. DØ Run II consists of two stages: Run IIa and Run IIb. Run IIa started in spring 2001 and ended in February 2006. During the following 14 week shutdown the Run IIb upgrade took place. At DØ this upgrade involved the installation of a new inner silicon layer, Layer 0, an upgrade to the CFT readout boards and an upgrade of the triggering electronics to help cope with the increased instantaneous luminosity being delivered by the Tevatron. Run IIb started in June 2006 and is planned to continue until at least 2010.

2.1 The Fermilab accelerator complex

The Fermilab accelerator complex can be sub-divided into two main components, proton and antiproton production, including the storage of antiprotons inside the Recycler, and acceleration and injection of protons and antiprotons into the Tevatron itself. Once all the protons and antiprotons are injected into the Tevatron, the bunches are then accelerated to 980 GeV, and after cleaning of the bunches to remove the proton and antiproton halos, are then made to collide at two interaction points. It is at these interaction points that the two experiments lie, the Collider Detector at Fermilab (CDF) and DØ. The layout of the Fermilab accelerator is shown in figure 2.1.

2.1.1 Proton and antiproton production

The accelerator chain begins with proton production. Negative hydrogen ions are accelerated to 750 keV by a Cockcroft-Walton accelerator and are then further accelerated to 400 MeV within the Linac. From there the H^- ions are stripped of their electrons and the remaining protons are injected into the Booster where they are accelerated to 8 GeV and passed onto the Main Injector. The Booster is a synchrotron with a 75 m radius and is also used to provide 8 GeV protons for the MiniBooNE [35] and SciBooNE [36] neutrino experiments. The Main Injector is a 3 km synchrotron which accelerates the 8 GeV to either 120 GeV for antiproton

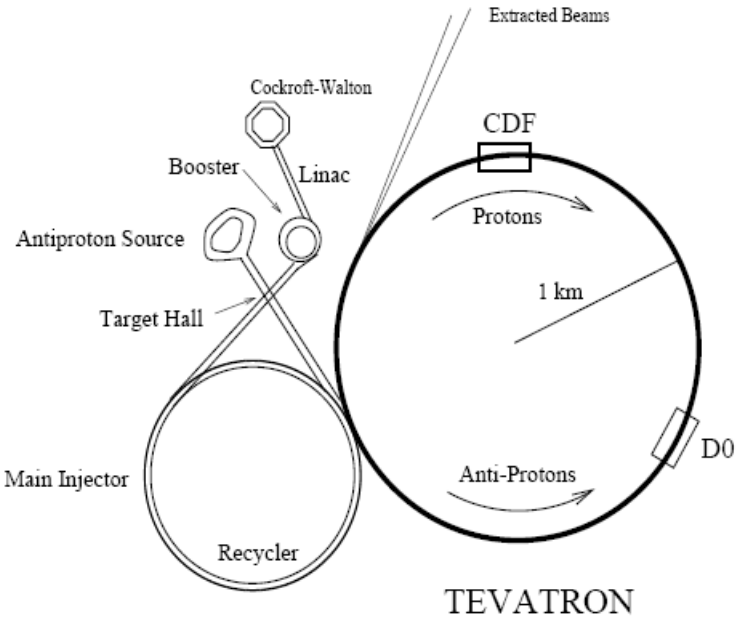

Figure 2.1: The Fermilab accelerator complex [34].

production, the NuMI neutrino experiment [37] and other fixed target experiments, or to 150 GeV ready for injection into the Tevatron.

Antiproton production begins with the 120 GeV proton beam from the Main Injector. This is fired onto a Nickel alloy target from which a secondary spray of particles is formed. A Lithium lens is used to focus the spray and it is passed through a bending magnet in order to select 8 GeV antiprotons. These are collected first in the Debuncher, which cools the antiprotons [38] and, once cooled enough, passed onto the Accumulator, which further cools the antiprotons and temporarily stores them ready for transfer to the Recycler. The Recycler is a fixed energy storage ring located in the Main Injector tunnel, designed for holding large numbers of 8 GeV antiprotons for a long period of time whilst further cooling the antiprotons [39].

2.1.2 The Tevatron

The Tevatron is currently the world's highest energy particle accelerator. It is a 6.3 km circumference synchrotron with superconducting magnets, which accelerates the protons and antiprotons to 980 GeV each, with both beams traveling within the

same pipe. The two beams are brought to focus at the two experiments, DØ and CDF. Table 2.1 details the operational parameters for the Tevatron for both Run I, Run IIa and Run IIb.

	Run I	Run IIa	Run IIb
Energy $p\overline{p}$ (GeV)	900	980	980
Proton bunches	6	36	36
Protons per bunch	2.3x10^{11}	2.7x10^{11}	2.7x10^{11}
Antiproton bunches	6	36	36
Antiprotons per bunch	5.5x10^{10}	3.0x10^{10}	8.7x10^{10}
Bunch spacing (ns)	3500	396	396
Peak luminosity ($cm^{-2}s^{-1}$)	0.16x10^{32}	1.2x10^{32}	3.2x10^{32}
Luminosity (pb^{-1}/week)	3.2	17.3	54.6
Interactions per crossing	2.5	2.3	4.8

Table 2.1: The operational parameters for the Tevatron in both Run I, Run IIa and Run IIb [40].

2.1.3 Current status of the accelerator

During Run IIa the Tevatron delivered ∼1.6 fb^{-1} of data. Improvements made to both antiproton production and storage, have led to much higher peak luminosities being reached in Run IIb than in Run IIa (as seen in figure 2.2). The rapid rise in peak luminosities and the ability to run for longer before needing to reload both protons and antiprotons have both contributed to the increased luminosity delivered per week between Run IIa and Run IIb. Figure 2.3 shows the total integrated lumiosity for all of Run II. Currently it is planned to keep running the Tevatron until at least 2010, and work is proceeding on trying to further increase the lifetime of each load of protons and antiprotons.

2.2 The Run IIa DØ detector

The DØ detector, shown in figure 2.4, has a cylindrical structure which is common to many modern high energy physics experiments. The equal energy of the proton and antiproton beams in the Tevatron means that the detector is symmetrical about the interaction region. The detector consists of three main subsystems: central tracking

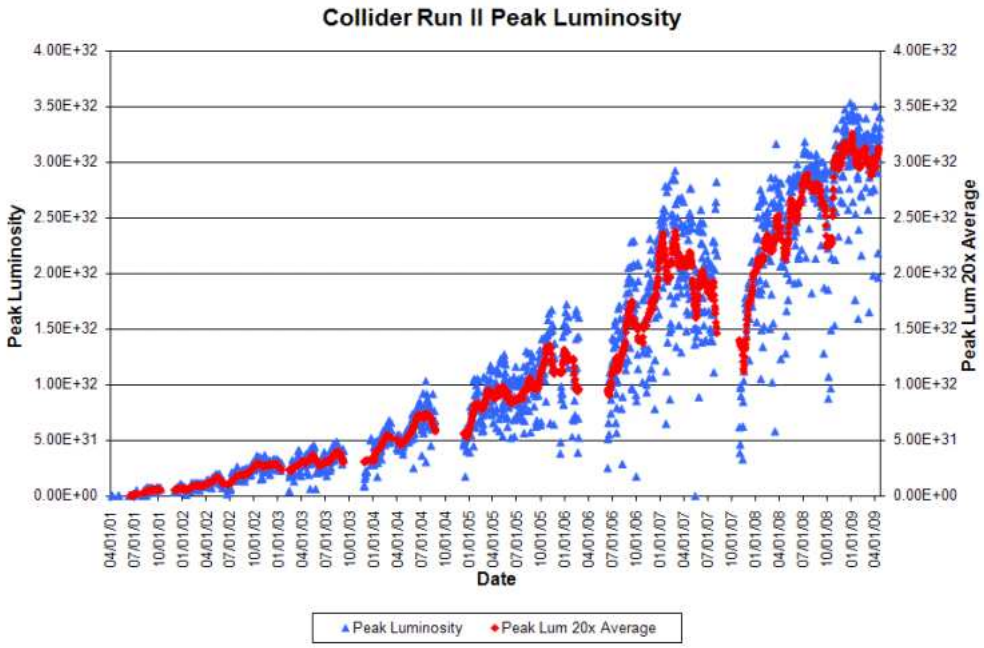

Figure 2.2: The peak luminosities reached by the Tevatron accelerator over Run II to date [41].

detectors for the identification of tracks and vertices, a calorimeter to measure the energy of photons, leptons and hadrons, and a muon spectrometer to identify and track muons. The three subsystems are organized concentrically with the tracking detectors at the centre and the muon subsystem on the outside of the detector. All subsystems are described in more detail in the following sections, and full details can be found in [43].

A right hand global detector co-ordinate system is used throughout this thesis. This co-ordinate system is orientated with the z-axis pointing along the beampipe in the proton direction, the y-axis pointing upwards towards the top of the detector and the x-axis pointing towards the centre of the Tevatron. This is more usually considered in terms of polar co-oridinates though, with the angles ϕ and θ representing the azimuthal and polar angles respectively ($\theta = 0$ along the proton beam direction), and r being the perpendicular distance from the beampipe. At DØ the polar angle θ is replaced by pseudo-rapidity, η, defined as:

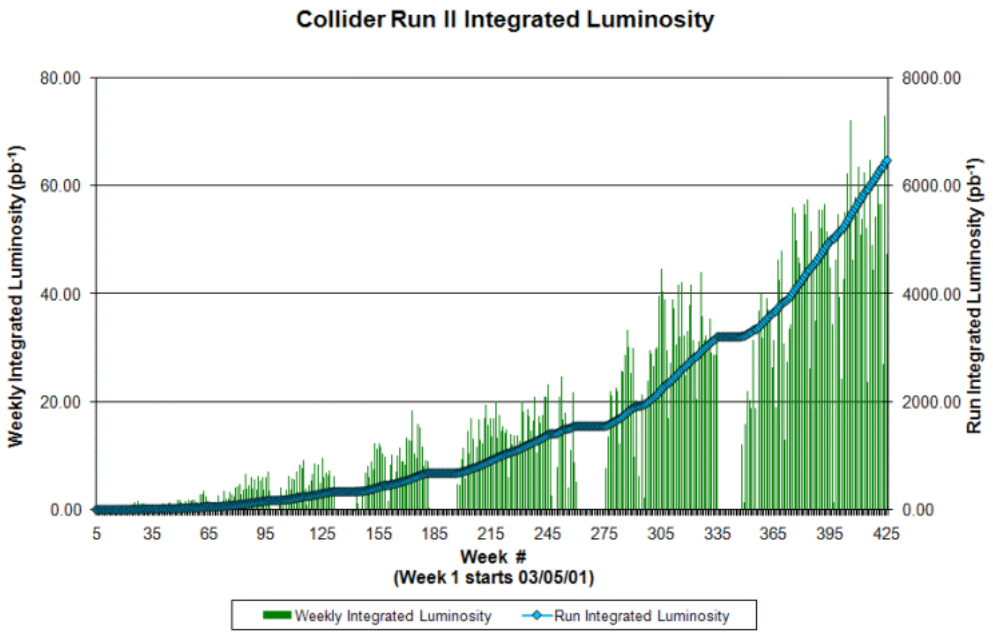

Figure 2.3: The total integrated luminosity delivered by the Tevatron throughout Run II so far [42].

$$\eta = -\ln\left(\tan\left(\frac{\theta}{2}\right)\right) \tag{2.1}$$

This is an approximation to the true rapidity in the limit that $\frac{mc^2}{E} \to 0$.

2.2.1 Central tracking

Good particle tracking and vertexing is essential for physics analysis, and in order to get the best quality final tracks and vertices possible. The tracking subsystem at DØ, shown in figure 2.5, consists of the Silicon Microstrip Tracker (SMT) surrounded by the Central Fibre Tracker (CFT), both of which are encased within a 2 T superconducting solenoid. Between the solenoid and the calorimeter sections are the preshower detectors.

The tracking systems described here are for the Run IIa detector, the upgrades made for Run IIb are described in section 2.3.

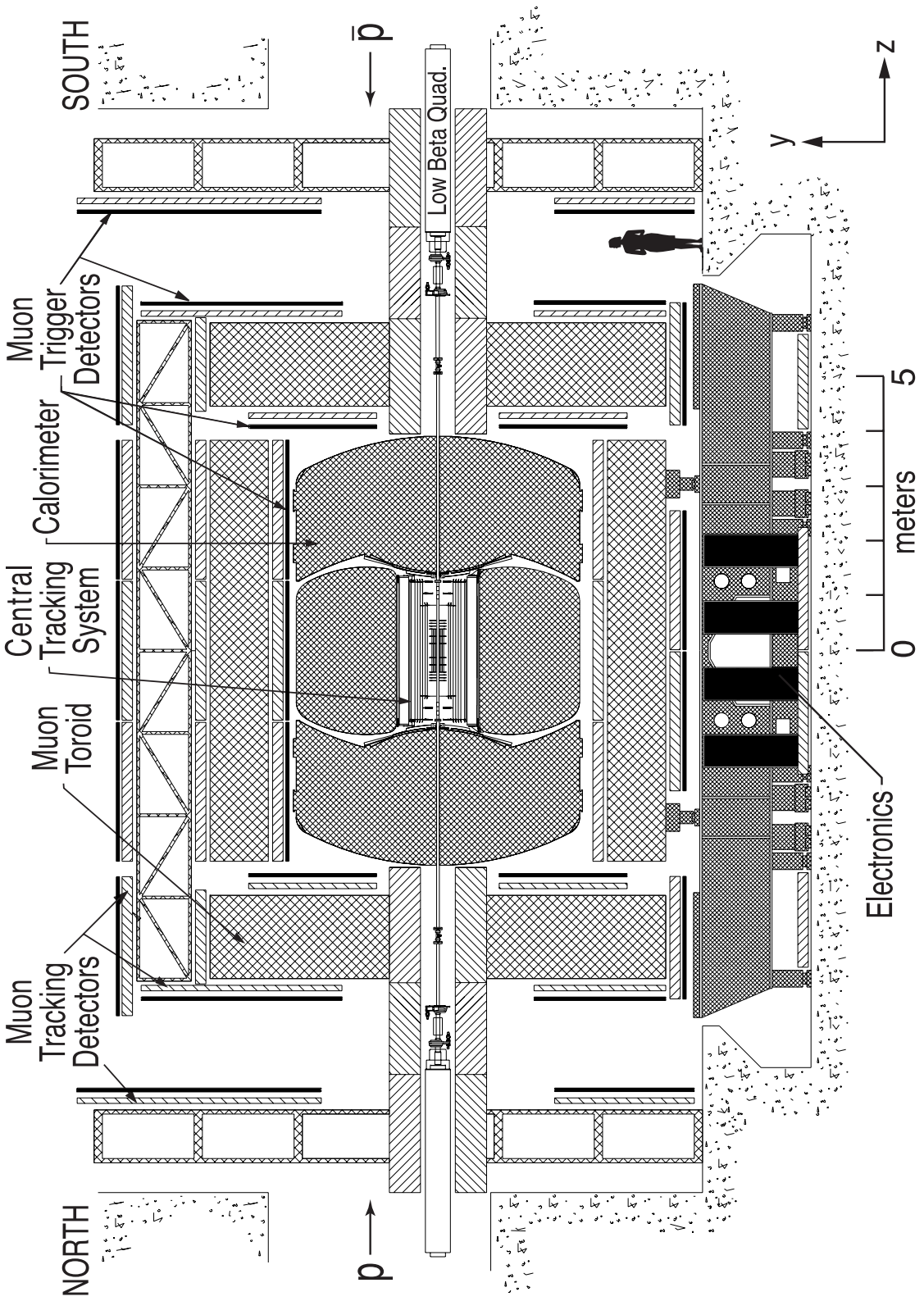

Figure 2.4: Side view of the DØ detector.

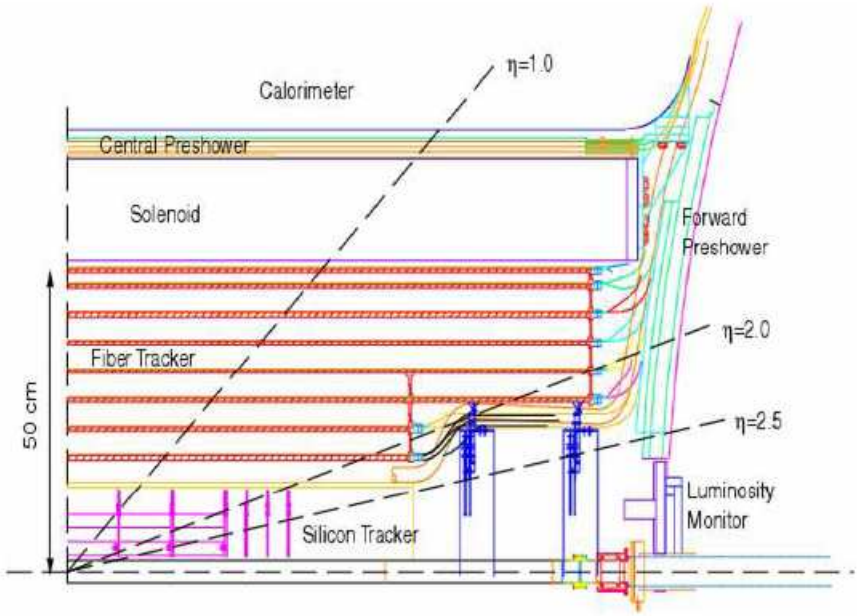

Figure 2.5: The DØ tracking subsystem.

Silicon Microstrip Tracker

The Silicon Microstrip Tracker (SMT) provides both tracking and vertexing over nearly the full η coverage of the calorimeter and muon systems. Its design, shown in figure 2.6, is dictated by the accelerator environment, it must account for the large interaction region ($\sigma_z \approx 25$ cm) and the silicon must be radiation tolerant. The Run IIa SMT is split into 3 subdetector types: the central barrels, the F-disks and the H-disks.

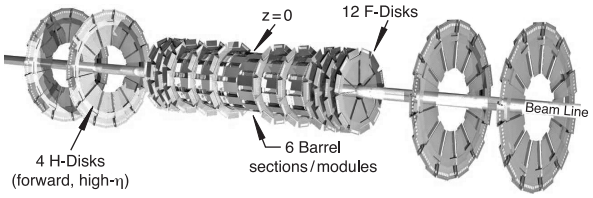

Figure 2.6: The DØ Run IIa Silicon Microstrip Tracker.

The barrels are primarily used to measure the $r - \phi$ coordinate, whilst the disks can measure both the $r - \phi$ and $r - z$ coordinates. There are 6 barrel detectors in total, with 3 on either side of the origin. Each barrel is comprised of 4 layers

of rectangular shaped silicon modules known as ladders and each of the ladders is double sided. There are 12 ladders in the inner two layers and 24 ladders in the outer two layers. Each barrel has a length of 12.0 cm with an inner radius of 2.7 cm and an outer radius of 10.5 cm to provide total silicon coverage within the region $|z| < 38$ cm and $|\eta| < 2.4$.

Each F-disk contains 12 double sided trapezoidal silicon modules called wedges. There are 12 F-disks in total, 6 capping the high $|z|$ of each barrel and 2 triplets of F-disks spaced at 5, 10 and 15 cm from either end of the barrel. The 4 H-disks are designed for high η coverage and are located about 1 m from the interaction point. Each H-disk is comprised of 12 wedges, and each wedge is composed of two back to back single sided silicon modules. The H-disks extend the silicon tracking up to $|\eta| < 3.0$.

Each ladder or wedge contains readout modules, most with a 50 μm pitch, known as strips. These provide a hit resolution of $\sim$ 10 μm. In total there are 912 strips with $\sim$ 800,000 channels. These provide a signal to noise ratio ranging from 12:1 to 18:1 depending on the detector type. The Run IIb upgrade introduced an additional inner layer of silicon inside the existing barrel modules, and this is covered in more detail in section 2.3.1.

Central Fibre Tracker

The Central Fibre Tracker (CFT) provides tracking in the region $|\eta| < 1.6$. It is composed of scintillating fibres mounted on eight concentric cylinders around the beampipe. The fibres are grouped into ribbons of 256 fibres, divided into two layers of 128 fibres offset by half the fibre diameter, known as doublet layers. These doublet layers are located on eight concentric support cylinders with radii ranging from 20.04 cm to 52.15 cm. Each of these cylinders has an axial layer (with ribbons pointing along the beam axis) and a stereo layer (with ribbons arranged $\pm 2^\circ$ to the beam axis), with the stereo layers alternating between these two angles.

The fibres themselves are constructed from doped polystyrene surrounded by a double cladding with a total diameter of 835 μm. The doping of the polystyrene helps

to both increase light yield and increase transmission efficiency. The fibres are connected to clear polystyrene waveguides which transmit the light signal to the visible light photon counters (VLPC) which are housed in a cryostat kept at 9 K. The VLPCs convert the light into an electrical signal and are capable of detecting single photons. The VLPCs also provide fast response, excellent quantum efficiency ($\geq$ 75%) and high gain (22,000 to 65,000).

Solenoid

The 2 T superconducting solenoidal magnet lies between the CFT and the preshower detectors and is designed to optimize the momentum resolution. The dimensions of the solenoid are largely determined by the space available and it is 2.73 m long, 1.42 m in diameter and is 1.1 radiation lengths thick. Inside the tracking volume the field is homogeneous to within 0.5%.

Preshowers

The preshower detectors aid in electron and photon identification, background rejection in both offline reconstruction and online triggering and in matching central tracks to calorimeter clusters. There are two preshower detectors: the central preshower (CPS) and the forward preshower (FPS). The CPS detector covers the region $|\eta| < 1.3$ and lies between the solenoid and the central calorimeter. The two FPS detectors cover the region $1.5 < |\eta| < 2.5$ and are attached to the inner faces of the end calorimeters. The locations of the CPS and FPS detectors is illustrated in figure 2.5. Both detectors are composed of interlocking triangular strips of doped polystyrene scintillator. These are connected by waveguides to VLPCs in the same way as the scintillating fibres in the CFT are.

Current performance

The Run IIa combined tracking subsystem can locate the primary vertex for a given event with a resolution of about 35 μm, and a b-tagging resolution of 15 μm for

central tracks with $p_T > 10$ GeV/c. The combined p_T resolution is $\Delta p_T/p_T = 0.0015 p_T$ where p_T is in GeV/c.

Currently there are about 15% of the SMT readout modules disabled and around 2% of the CFT and preshower detectors dead [44]. In the case of the SMT readout most problems are caused by defects on the boards, however the Layer 1 barrel sensors are beginning to show signs of signal to noise degradation due to the high integrated radiation dose they have received. In the case of the CFT and preshower detectors the problems lie in damage to the VLPCs. In addition, the solenoid is operating at ∼96% of its design current to allow continuing safe operation of the magnet.

2.2.2 Calorimeter

The DØ calorimeter, shown in figure 2.7, measures the energy of electrons, photons and jets out to $|\eta| \approx 4$. The calorimeter is comprised of three sections: the central calorimeter (CC) and two end caps (EC). The CC provides coverage up to $|\eta| \sim 1$ and the EC provide coverage up to $|\eta| \sim 4$. It is a liquid argon sampling calorimeter using depleted uranium, copper and stainless steel absorbers. The depleted uranium acts a compensation medium to allow the calorimeter to respond almost equally to both electromagnetic and hadronic showers. The ratio of electromagnetic and hadronic response ranges from 1.11 at 10 GeV to 1.04 at 150 GeV. The presence of liquid argon as the ionizing medium requires that it be kept at a temperature of about 80 K.

Central calorimeter

The CC is divided into three sections corresponding to concentric cylinders around the beampipe and tracking subsystems. These three sections are the electromagnetic (EM), the fine hadronic (FH) and the coarse hadronic (CH) with the EM the innermost and the CH the outermost section. The EM layers are designed to collect most of the EM energy, the FH layers most of the hadronic energy and the CH layers any leakage. The EM section has 4 layers and a total depth of 20 X_0, where X_0 is

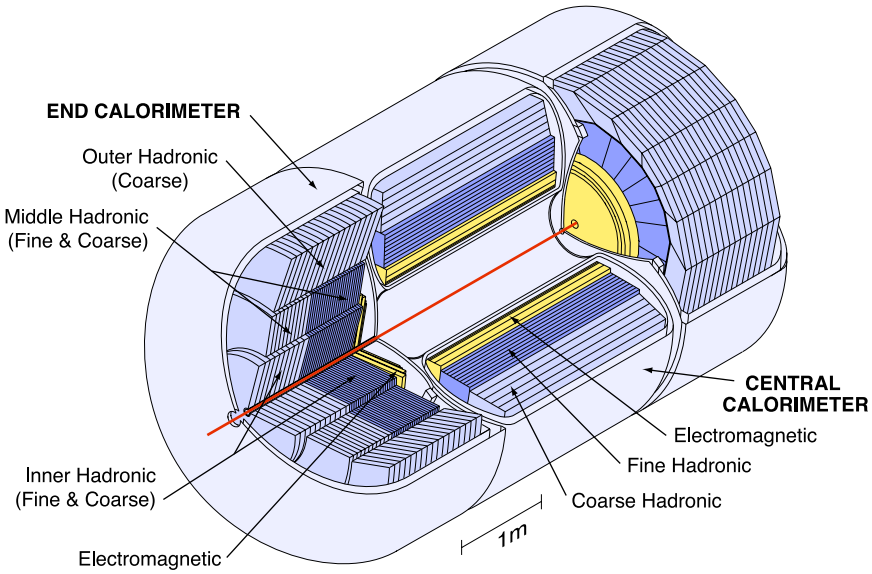

Figure 2.7: The DØ calorimeter.

the electromagnetic absorption length, the FH 3 layers and a depth of 3.1 λ_A, where λ_A is the nuclear absorption length, and the CH is a single layer providing a depth of 3.6 λ_A. Each layer is subdivided into cells approximately 0.1×0.1 in $\Delta\eta \times \Delta\phi$, where ϕ is in radians, except for the third EM layer (where the maximum EM energy deposit occurs) which has a finer granularity of 0.05×0.05.

End calorimeters

The two EC calorimeters are each divided into four sections: electromagnetic (EM), inner hadronic (IH), middle hadronic (MH) and outer hadronic (OH). The IH and MH have both fine and coarse regions, whilst the OH is coarse. The EM section consists of 4 layers with a total depth of 21.4 X_0, the IH section has 4 fine granularity layers with a depth of 4.4 λ_A and 1 coarse layer with a depth of 4.1 λ_A, the MH section also has 4 fine layers but with a depth of 3.6 λ_A and 1 coarse layer with a depth of 4.6 λ_A, and the OH is only 1 coarse layer with a depth of 6.0 λ_A. Each of the layers are subdivided into cells as in the CC except that the finer segmentation in layer 3 of the EM section is only present up to $|\eta| < 2.6$. In addition, beyond $|\eta| > 3.2$, the segmentation increases in both $\Delta\eta$ and $\Delta\phi$.

Intercryostat detector

The region $0.8 < |\eta| < 1.4$ has incomplete coverage from the calorimeter and substantial unsampled material, so to provide additional sampling in this region and improve the energy resolution the intercryostat detector (ICD) is introduced. This consists of an array of 16 scintillating tiles which are mounted on the face of both end cryostats to provide region coverage of $1.1 < |\eta| < 1.4$. The tiles are subdivided into readout cells of 0.1×0.1 in $\Delta\eta \times \Delta\phi$ to produce a total of 384 channels. Optical fibres carry the scintillation light to phototubes located outside the magnetic field.

Current performance

The calorimeter is currently operating with 99.8% of the 48,000 channels operational. The calorimeter performance was measured in test beam studies [45] and the response found to be:

$$\begin{aligned} \text{EM}: \quad & \frac{\sigma_E}{E} = \frac{0.15}{\sqrt{E}} + 0.003 \\ \pi^{\pm}: \quad & \frac{\sigma_E}{E} = \frac{0.45}{\sqrt{E}} + 0.04 \end{aligned} \tag{2.2}$$

2.2.3 Muon system

The muon system is the outermost layer of the detector and was upgraded for Run II to provide full coverage and triggering out to $|\eta| = 2$. There are two sections to this sub-detector, the central muon system up to $|\eta| < 1$, called the wide angle muon system, and the forward muon system covering the region $1 < |\eta| < 2$, called the forward angle muon system. Either proportional or mini drift tubes, depending on the location, are used for muon identification and scintillator counters aid in triggering and in background reduction. An exploded view of the muon drift tubes can be seen in figure 2.8. In addition a solid iron toroid magnet with a field of 1.9 T bends the muon trajectory in the $r - z$ plane.

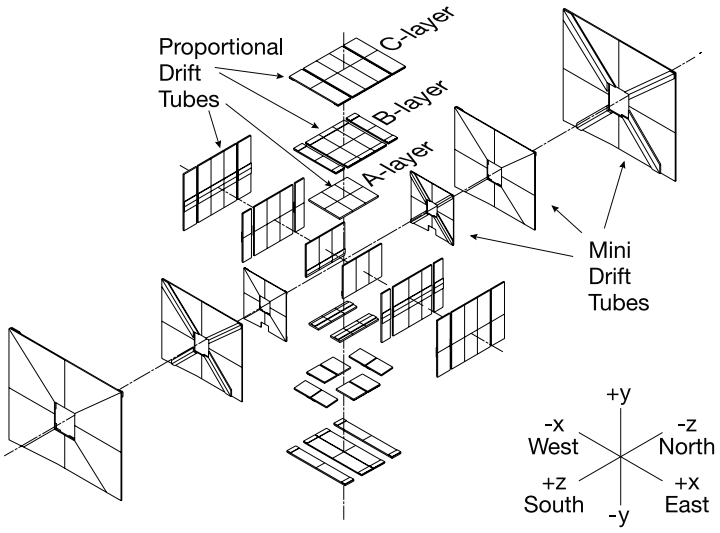

Figure 2.8: Exploded view of the DØ muon drift tubes.

Wide angle muon system

The wide angle muon system (WAMUS) consists of three layers of proportional drift tubes (PDTs), one of which is inside the toriod (A layer) and two of which are outside the toroid (B and C layers). The PDTs are made of rectangular extruded aluminium tubes and are typically 2.79×5.59 m^2. The PDTs are broken down into cells of 10.1 cm width with a gold clad, tungsten anode wire down the centre. The gas used is mostly argon with some methane and CF_4 mixed in and this provides a maximum drift time of 500 ns. The A layer contains 4 decks of cells and the BC layers contain 3 decks of cells. The hit resolution for the PDTs is ~ 1 mm. There are also two layers of scintillator counters, one between the calorimeter and the A layer of PDTs and one outside of the C layer, except on the underside of the detector, where due to the support structures the counters are on the outside of the B layer instead. The scintillator counters provide a time resolution of 1.6 ns and there are 986 counters in total.

Forward angle muon system

The forward angle muon system (FAMUS) consists of three layers of mini drift tubes (MDTs) which are arranged similarly to the PDTs in the WAMUS, with the A layer

inside the toroid and the BC layers outside the toroid. Aligned along the magnetic field lines there are four decks of cells in the A layer and three decks of cells in the BC layers. Each MDT is made from an aluminium extrusion comb with a stainless steel foil cover and is subdivided into eight 1×1 cm^2 cells, each with a gold-tungsten anode wire in the centre. The MDTs use CF_4 gas mixed with a small amount of CH_4, which is both radiation hard and fast, and this allows for a maximum drift time of 60 ns, which is less than the bunch crossing time. The overall hit resolution for the MDTs is 0.7 mm. The smaller maximum drift time in the MDTs means that scintillators are not required for matching drift tube hits to events, however they are still used to reduce backgrounds, such as cosmic rays, and to aid in triggering. There are three layers of scintillator counters corresponding to each of the MDT layers.

Current performance

The WAMUS system has a momentum resolution of:

$$\sigma(1/p) = \frac{0.36(p - 3.1)}{p^2} \oplus 0.03 \tag{2.3}$$

where p is in GeV/c. The FAMUS has a momentum resolution of around 20% for muons under 40 GeV/c. The momentum resolution of the muon system is defined by the central tracking system for muons up to 100 GeV/c, after this the muon systems improve the resolution.

The WAMUS has $\sim$ 98% of its PDTs still active, and 99.8% of the scintillation counters active. The FAMUS has $\sim$ 99% of its MDTs active and 99.9% of its scintillation counters active [46].

2.2.4 Luminosity monitor

The luminosity monitor (LM) is used to determine the Tevatron luminosity at the DØ interaction region by detecting inelastic $p\overline{p}$ collisions. The detector consists of

two arrays of 24 plastic scintillator counters, with PMT readout, located at $z\pm$ 140 cm. The LM is located just in front of the EC calorimeters and occupy the radial region between the beam pipe and the forward preshower detectors ($2.7 < |\eta| < 4.4$). By finding the average number of inelastic collisions per beam crossing, $\overline{N_{LM}}$, the total luminosity, $\mathcal{L}$, can be found from the following formula:

$$\mathcal{L} = \frac{f\overline{N_{LM}}}{\sigma_{LM}} \tag{2.4}$$

where f is the beam crossing frequency and σ_{LM} is the effective cross section taking into account the acceptance and efficiency of the LM detector.

2.2.5 The Run IIa trigger

The vast majority of $p\overline{p}$ collisions produce what are background events due to the high production cross section for elastic and inelastic proton scattering interactions. In comparison 'signal' events, that is those collisions that contain samples analysers are interested in studying, have much smaller cross sections, and so some way is needed to select the signal processes. The trigger is designed to find and retain the signal events from the overwhelming background.

DØ has a three level triggering system, each level more complex than the previous. Level 1 is hardware based and uses Field Programmable Gate Array (FPGA) chips to process its decisions, but only for each individual subsystem. Level 2 is also hardware based, but uses more advanced algorithms and allows for global detector decisions to be made. Level 3 is software based and uses dedicated code and full detector readout with which to perform a partial reconstruction of the event. Table 2.2 shows the trigger rates for each of the three levels of trigger. A program called `COOR` is responsible for handling the overall coordination and control of the trigger system, as well as providing an interface to the both the trigger framework (for Levels 1 and 2) and the data acquisition (DAQ) supervisor for Level 3. Figure 2.9 shows an overview of the DØ trigger and DAQ systems.

	Rate	Latency
Collisions	1.7 MHz	-
Level 1	1.6 kHz	3.6 μs
Level 2	800 Hz	$\sim 100\mu$s
Level 3	50 Hz	$\sim 200\mu$s

Table 2.2: Approximate trigger rates and latency for the DØ Run IIa triggering system.

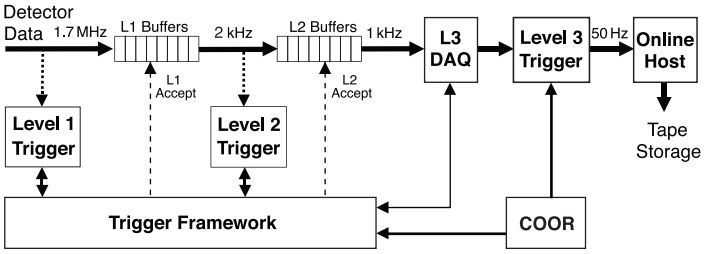

Figure 2.9: Schematic layout of the DØ triggering system in Run IIa. Trigger rates shown are limits for Level 1 and Level 2.

Level 1 trigger

The Run IIa Level 1 trigger utilizes a reduced form of readout for each of the calorimeter (L1CAL), CFT and preshowers (together known as the Central Track Trigger, L1CTT) and muon subsystems (L1MU). In the L1CAL transverse energy, E_T, as measured by the calorimeter cells, is summed together to form $\Delta\eta \times \Delta\phi \sim 0.2\times0.2$ trigger towers. A trigger decision is made based on either the total E_T of the trigger towers exceeding a preset value, or by counting the number of trigger towers exceeding a preset value. The L1CTT groups the CFT axial fibres into 4.5° sections, and then proceeds to match the resultant hits to pre-programmed track patterns representing different p_T thresholds. The L1CTT also performs a hit matching process to add preshower data to the CFT-only tracks. L1MU utilizes information from the muon scintillator counters and the muon wire chambers and then combines them with tracks from the L1CTT to look for patterns consistent with muons passing through the detector. The scintillators and drift tube chambers in layers A, B and C are matched to those sectors of the CFT where tracks have been found by L1CTT.

The results from each of the separate Level 1 triggers are logically combined into a maximum of 128 different triggers, the output of which is called a trigger bit. Each subdetector stores its readout for the event temporarily within a buffer waiting to see if a Level 1 trigger has passed. Should all the requisites for a given trigger bit be satisfied then that trigger is said to have 'fired' and the event is passed on to the Level 2 trigger.

Level 2 trigger

The Level 2 trigger takes the trigger information from Level 1 and further refines it through the use of more advanced algorithms, and adds in information from the SMT. For every Level 1 trigger bit there can be several corresponding Level 2 bits. The Level 2 triggering system consists of preprocessors for each subdetector, that is the calorimeter (L2CAL), tracking (L2CTT), preshowers (L2PS) and muon systems (L2MU), and a global processor (L2Global) which makes the trigger decision based upon the output from the preprocessors. The preprocessors process the data from the individual subdetectors to produce physics objects (such as muons, jets, tracks and electrons) which are then sent to L2Global.

The tracking processor, L2CTT, combines information from both L1CTT and information from the Level 2 silicon track trigger (L2STT) to create more accurate tracks. The L2STT performs pattern recognition in the data from the SMT. This allows for tracks to be reconstructed with the much finer spatial resolution of the SMT rather than using the L1CTT alone. L2STT starts with the tracks found by the L1CTT and defines a road around each track, it then tries to add hits in the axial strips of the silicon ladders, which define points in the $r-\phi$ plane. The tracks found by the L2STT are then sorted into two lists by L2CTT, one sorted by p_T and the other sorted by impact parameter, and the final track lists passed on to L2Global.

L2Global creates global physics objects from one or more of the subdetector objects, for example matching a track to an EM object to make an electron. The resultant global physics objects can then be used for triggering decisions, such as specific

object cuts or the calculation of kinematical variables from multiple objects. Each Level 1 trigger bit corresponds to one or more Level 2 triggers, and for any fired Level 1 trigger bit the corresponding Level 2 triggers are processed. If any of the Level 2 trigger thresholds pass then the event is passed on to Level 3 and the entire detector read out.

Level 3 trigger

The Level 3 trigger is fully software based and has access to the full detector read out with which to partially reconstruct the event. The Level 3 trigger runs on a farm of standard PCs running Linux, with each PC running an independent instance of the Level 3 software, or more than one instance should the PC contain more than one CPU. Each instance of the software processes complete events sequentially and if accepted the event is written to tape.

There are three types of tool in use at Level 3: unpacking tools, data tools and physics tools. Unpacking tools are used to both read in the data and then to convert it into a form that can be used by either the data or physics tools, examples are the SMT and CFT unpackers. The data tools perform most of the computation needed at Level 3, examples of data tools are the tracking and vertexing tools. The physics tools are used to create physics objects, such as jets, muons or electrons, that can be used for triggering upon. Tools can call other tools as needed, and the results are cached to ensure that the tool is only run once per event. Each tool has a set of parameters to control the behaviour of the tool's algorithms, and are assigned upon instantiation of the tool. There are a limited number of parameter sets for each tool, and these are the only instances of the tool which the trigger can call. Chapters 3,4 and 5 of this thesis detail work completed on some of the unpacking and data tools used at Level 3.

Each Level 2 trigger bit corresponds to at least one Level 3 trigger, and should a Level 2 trigger bit be set then the corresponding Level 3 triggers are processed. Each Level 3 trigger is made up of a 'filter script', which continas one of more "filters". Filters define a condition that must be met for the trigger to fire, should there be

more than one filter in use by a filter script then each must pass their set conditions. The Level 3 software interface is called `ScriptRunner`. At the beginning of a run `ScriptRunner` parses a 'trigger list' and initialises all the required tools and sets all necessary filter scripts needed for the run according to the trigger list.

There are two types of filters in use at DØ, these are physics filters and relational filters. Physics filters are used to compare the physics objects produced by the physics tools to thresholds set by the trigger list through `ScriptRunner`. Relational filters are used to execute other filters and to combine individual filter results together. At the end of a filter script, a check is made to see if there is at least the minimum number of objects required to satisfy the script requirements, and if so then the event passes Level 3 and is written to tape.

2.3 Run IIb and the DØ detector

During the 2006 shutdown the DØ detector underwent the Run IIb upgrade. The upgrade involved both the addition of a new inner layer of silicon to the existing barrel detectors, Layer 0, and also substantial upgrades to the triggering system, particularly at Level 1. Both of these upgrades are described below, and in more detail in [47].

2.3.1 The Layer 0 detector

The Run IIa silicon detector was built to withstand 2 to 4 fb^{-1} of integrated luminosity. The advent of Run IIb and the possibility that a total integrated luminosity of over 8 fb^{-1} will be delivered by the Tevatron, will result in vastly degraded performance from the existing inner layers of the silicon detector due to radiation damage. Original plans called for a complete replacement of the Run IIa SMT with a new upgraded version for Run IIb, however due to funding concerns these plans were changed to a simpler, but no less important design for the Run IIb SMT. These new plans involved the installation of a new silicon detector inside of the Run IIa SMT. This new silicon detector, called Layer 0, was based on the design plans for the

original RunIIb SMT replacement, and improves the impact parameter resolution of the tracker. Further details on the design of Layer 0 can be found in [48, 49].

The requirement that Layer 0 fit inside of the existing SMT places stringent limits on the size of the new detector. In addition to this, the ability to interface Layer 0 with the existing triggering and read out framework, as well as the need for the chips and sensors to be radiation hard, sets constraints on the electronics design. The result of these design constraints is shown in figure 2.10.

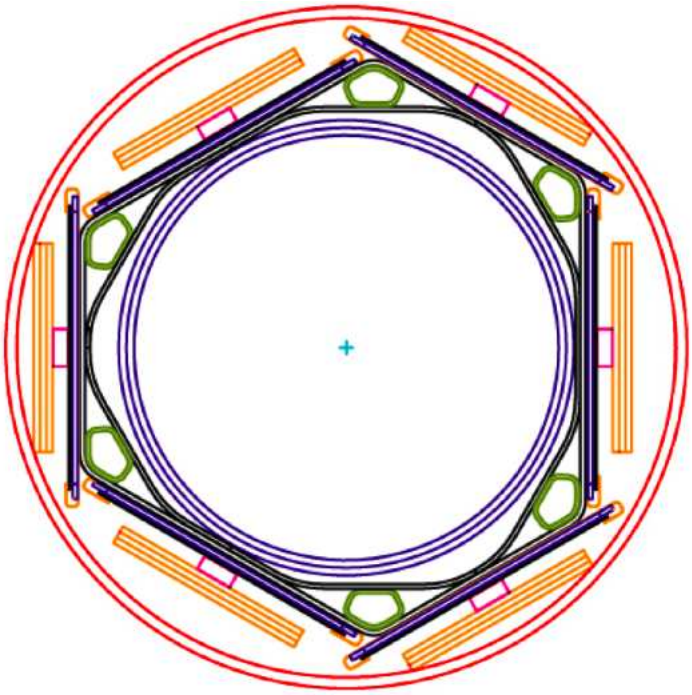

Figure 2.10: Axial view of the Layer 0 detector. The silicon sensors are shown in blue surrounding the beampipe in the centre [48].

Unlike the Run IIa barrel detectors, the readout chips are not mounted on the sensors themselves, instead analogue cables carry the signals to chips located on separate boards. This is due to both the tight space constraints and the need to minimize the amount of material in between Layer 0 and the existing SMT. The tight space constraints have also necessitated the design and installation of a new smaller beryllium beampipe to carry the proton and antiproton beams through the experiment, as Layer 0 now sits where the previous Run IIa beampipe was located. Also, due to a lack of spare cables to carry data from both the existing and new

detector and no space to install more cabling, the outer H-disks were removed from the existing SMT.

Layer 0 contains 8 barrels, each with 6 ladders of single sided silicon sensors. The emphasis on improving the impact parameter resolution in the $r-\phi$ plane, combined with the limited space available, led to the decision to concentrate on single sided modules only. The sensors are mounted on a carbon fibre support structure, and each sensor has 256 channels and a pitch of 70 to 75 μm, with a total of 48 modules in use, each with 2 chips, for detector readout. The overall detector has a radius of $16.0 < r < 22.0$ mm, with the sensors located at $r \sim 17$ mm. The 8 barrels are symmetrical around $z = 0$, with those barrels closest to the centre point being shorter in length (70 mm) than those further away (120 mm). This results in a signal to noise ratio for the new detector of 15:1 for the $\sim$ 12,000 new channels, and a factor of 1.5 improvement in the overall impact parameter resolution.

2.3.2 Run IIb trigger upgrades

The triggering system also underwent substantial upgrades during the shutdown period, in particular to Level 1 [50]. The majority of the Level 1 Run IIb upgrades focused on upgrading the L1CAL to better handle the increasing luminosity without the need for large prescales to be applied to the calorimeter triggers [51]. Prescales are a 'quick and dirty' method of reducing rates for a given trigger by only allowing 1 in x possible events to be processed by the trigger, where x is the prescale, and as such are highly undesirable but sometimes necessary. The upgrade to L1CAL2b involved replacing the majority of the L1CAL algorithm boards with new boards designed around a more detailed object identification algorithm known as the 'Sliding Windows' algorithm [51]. The sliding windows algorithm allows for L1CAL2b to trigger on clusters of trigger towers in $\eta - \phi$ space. Each of the different calorimeter objects, jets, electrons and taus, will produce different cluster signatures, and by searching for these signatures using the sliding windows technique L1CAL2b has a much improved background rejection over the Run IIa L1CAL. In tests on the same trigger list, L1CAL2b was found to reduce the Level 1 rate by nearly a factor of

two compared to the Run IIa L1CAL. By improving the background rejection, cuts on individual triggers can be lowered, and thus improve the physics yield for all analyses which use L1CAL triggers.

To accompany the upgraded L1CAL2b system, a new Level 1 triggering system has been added for Run IIb, L1CalTrk. L1CalTrk is based upon the final stage of the L1MU systems, where identified muon hits are matched to tracks found by L1CTT, and allows for the matching of L1CAL2b objects to tracks found by L1CTT. By doing so, L1CalTrk helps to further improve background rejection for all calorimeter objects, and in high luminosity situations is vitally important at keeping trigger rates within limits [50]. The L1CTT also underwent an upgrade for the Run IIb run with the replacement of the hardware which performs the track pattern matching with a more powerful version. Combined with new improved track equations, this upgrade allows for the L1CTT to make better use of the granularity of the CFT axial fibres and hence reduce the fake rate (and thus the trigger rate) [52].

Level 2 also saw minor upgrades to its hardware and software. The hardware upgrades involved modifications to the L2STT to incorporate Layer 0 and firmware upgrades to the preprocessors themselves to allow for parallel processing of subdetector data to allow for more complex algorithms to be used for object creation [50]. In addition to this the facility to perform the OR-ing of Level 2 triggers was also added to the existing system. This allows for more than one Level 2 bit to be assigned to each Level 1 trigger bit and thus allow for more complex triggers to be designed to improve physics yield. Level 3 also underwent upgrades, particularly with respect to the software tools relating to tracking, but also in some of the physics filters too, to help Level 3 with event processing times. In addition, the Level 3 farm has also been expanded for Run IIb to enable more Level 3 instances to run simultaneously. The Level 3 Run IIb tracking upgrades are covered in detail in chapters 4 and 5 of this thesis. The overall trigger rates for Run IIb are shown in table 2.3.

	Rate	Latency
Collisions	1.7 MHz	-
Level 1	1.8 kHz	3.6 μs
Level 2	900 Hz	$\sim 100\mu$s
Level 3	100 Hz	$\sim 200\mu$s

Table 2.3: Approximate trigger rates and latency for the DØ Run IIb triggering system.

2.4 Software

The reconstruction (d0reco) and programmable trigger (Level 2 and Level 3) software is written in C++, and both reconstruction and Level 3 utilize an object-orientated structure. All data for an event are stored in the DØ event data model (EDM) as a collection of 'chunks'. For example, the raw data for an event are stored in the `RawDataChunk`, whilst the Level 3 output is stored in the `L3Chunk`. The input to the reconstruction software comes from previously created chunks already stored in the event data, and writes its output as a new chunk into the EDM data for that event, for example the d0reco tracking algorithms store their output within a `GTrack` chunk.

2.4.1 Code version numbering

Different versions of the DØ code have been used throughout this thesis, both for Level 3 reconstruction and for offline reconstruction and data analysis. The various versions are referred to by the terminology pXX, where XX is an integer describing the version number, and is increased by one for each major revision of the code. The trigger lists also have their own numbering scheme, vXX, where XX is an integer describing the next major trigger list version. Four different versions of code have been used in particular during the work described in this thesis - the following describes the use for each code version:

- **p16** - Level 3 code version designed for the v13 trigger list

- **p17** - Speed optimized Level 3 code designed for the v14 trigger list; Reconstruction version used for Run IIa processing; Run IIa Monte Carlo generation
- **p19** - Level 3 code version for Run IIb and designed for the v15 trigger list
- **p20** - Reconstruction version used for Run IIb processing; Run IIb Monte Carlo generation

Chapter 3

Level 3 p16 speed increases and p17 tracking and vertexing certification

3.1 Preface

This chapter details work conducted on the Level 3 online tracker in two different software production releases, p16 and p17, as well providing a brief introduction to the Run IIa Level 3 software tracking algorithms, the tracking algorithms used in the DØ reconstruction program, d0reco, and the Level 3 vertexing software. Work performed on both p16 and p17 was conducted whilst the new Run IIb tracking software was in development as short-term solutions to timing problems and tracking inefficiencies. p16 ran from June 2004 to June 2005, whilst p17 ran from June 2005 to February 2006.

Increased peak luminosities delivered to the DØ detector led to timing problems with the p16 version of the Level 3 trigger. The increase in luminosity results in more minimum bias interactions on average per event, and hence there are more tracks to reconstruct, thus more time needed to reconstruct the event. Studies of these timing problems revealed that one of the major culprits was the tracking software. Detailed in this chapter is work performed to improve tracking processing time without requiring a rewrite of the software. This includes a trimming of the

dead fibre file, which is used to improve hit pattern recognition in the CFT by artificially turning on non-responsive fibres, and the viability of raising the minimum tracking p_T cuts for various Level 3 filters. The result of these studies led to the implementation online of a trimmed dead fibre list and the raising of the the p_T cut to 3 GeV/c for the z vertex finding tool.

Once the timing situation in the p16 software was stabilized, work proceeded on the certification of the Level 3 software in the new production release, p17. This software version includes improvements within both the tracking algorithm and the SMT unpacker. Due to the substantial code changes, a thorough study of the tracking performance compared to p16 was required. Studies were also done of the performance of the Level 3 software tracker in various specific situations, including the effect of high energy jets on tracking performance and the viability of the processor intensive dead fibre file, in particular with respect to high p_T tracks. The p17 software was found to be substantially improved in terms of tracking efficiency compared to p16, whilst requiring similar processing times.

3.2 Run IIa Level 3 tracking

The Run IIa Level 3 (L3) track finding tool, `L3TGlobalTracker`, was built to attempt to balance both track finding efficiency and speed [53]. The tight time budget at Level 3, of 250 ms per event on average - with a 3 second maximum, means that a slow but efficient tracking algorithm is undesirable, as is a fast but inefficient tracker which merely finds lots of fake track candidates. Good tracking efficiency will directly help in many of the other Level 3 tools, for example the b-tagging, lifetime and track-matched muon tools, and hence is crucial for the overall trigger efficiency.

The software works with the clusters returned by the Level 3 CFT and SMT clustering and unpacking tools, `L3TCFTUnpack` [54] and `L3TSmtUnpack` [55] respectively. The tracking algorithm can then further be reduced down to axial and stereo components with the axial algorithm being run first. Each of the components will be described here. It should be noted that at Level 3 only the SMT barrels are used

for track finding, the F-disks and H-disks are ignored by the tracker to help reduce processing time. This of course means that the Level 3 tracking software only concentrates on central tracks ($|\eta| < 1.5$) as the full tracking fiducial volume is not used. The tracks themselves are assumed to be helical and are defined by five defining parameters (shown in figure 3.1), three axial and two stereo:

- DCA - impact parameter
- ϕ_0 - ϕ angle of track to beamspot
- R_{inv} - the inverse of the track radius, used to find p_T
- Z_0 - z displacement of track to beamspot
- $\tan(\lambda)$ - the stereo pitch angle of the track

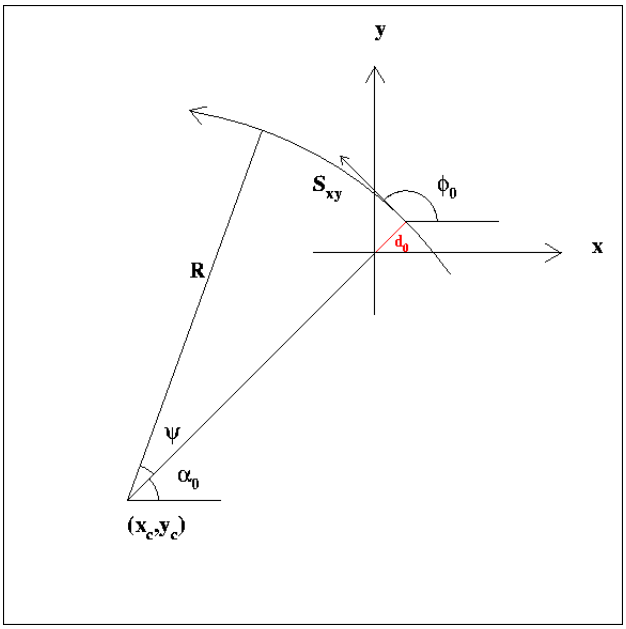

Figure 3.1: Illustration of the five helical parameters used in describing tracks from both the Level 3 and d0reco tracking software. R is used to calculate $1/p_T$, d_0 is the DCA, $\tan(\lambda)$ is the ratio of the rate of change of z with respect to the distance traversed in the $x-y$ plane, Z_0 is the z at d_0 and ϕ_0 is the ϕ at d_0.

The axial algorithm begins by looking at the two outermost layers of the CFT and then making potential tracks between all pairs of hits found in those two layers,

and keeping any candidates which then pass a p_T threshold cut. The remaining candidates are then propagated into the the remaining CFT layers, and then the SMT barrels, finding clusters that are consistent with the track's predicted position at each layer. New track candidates are then created if the χ^2 of the new track is found to have increased by less than 10. After removal of tracks which miss more than one layer of the CFT, the 3 or 4 tracks with the best quality are kept (the number depending on layer). The final step in the process involves the identification of tracks which share more than two hits, and the discarding of the worse of the two candidates. A simplified circle fitting algorithm is then used to obtain the axial track parameters.

The stereo tracking algorithm uses a fast histogramming method, based on Hough transformations [56], to determine which stereo clusters are associated to a particular axial track. Hough transformations allow for hits and tracks observed in the cartesian space (that is in terms of x, y and z) to be transformed into the track parameter space (that is in terms of the helical track parameters DCA, ϕ_0, R_{inv}, Z_0 and $\tan(\lambda)$), where they can be more easily handled. An example of a simple 2D Hough transform of tracks from (x, y) to (ϕ_0,ρ) is shown in figure 3.2. Here tracks become points and hits become lines in (ϕ_0,ρ) space (where ρ represents the parameter R_{inv}) , as opposed to tracks being helices and hits being points in (x, y) space.

In the tracking algorithm, the transform is made from (x, y, z) space to $(Z_0, \tan(\lambda))$ space such that intersections between the hits, described as lines, are where tracks can be found. Since a stereo cluster lies on an infinite number of possible stereo tracks, in `L3TGlobalTracker` a 2-D histogram in Z_0-$\tan(\lambda)$ space is filled with all the possibilities from all the stereo clusters associated to an axial track. The most populated bin in said histogram will then normally correspond to the parameters of the correct stereo track. The stereo clusters in that bin are then used in a fitter algorithm to calculate the best stereo track fit.

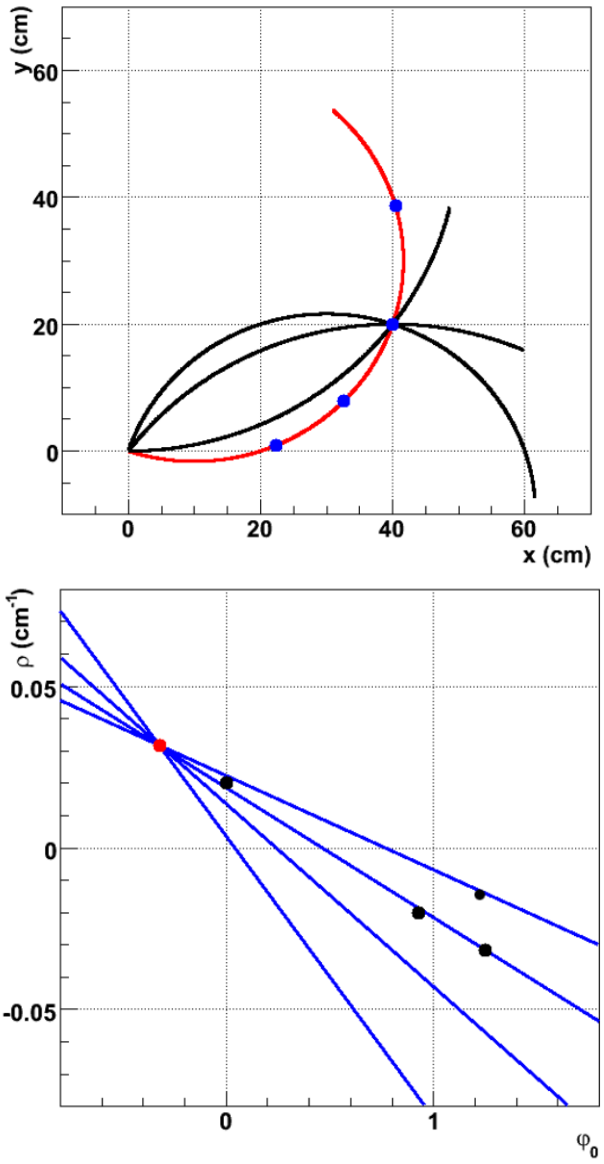

Figure 3.2: Example of a simple 2D Hough transformation from (x, y) space (top) to (ϕ_0, ρ) space (bottom). The lines on the (x, y) graph become the dots on the (ϕ_0, ρ) graph, whilst the points on the (x, y) graph become the lines on the (ϕ_0, ρ) graph. The parameter ρ here represents the parameter R_{inv} [57].

3.3 Run IIa d0reco tracking

The d0reco [58] tracking algorithm uses two different algorithms to perform pattern recognition and then another algorithm to filter the patterns and choose good quality track candidates with which to make tracks from. The two pattern recognition algorithms are AA [59] and HTF [57] and each will be described below. The GTrack fitter [60] then takes the patterns from AA and HTF and then uses these as seeds for a Kalman filter [61] with which to locate tracks, taking into account variations in the magnetic field, multiple scattering and energy loss. It should be noted that any of these three tracking algorithms can be run independently of one another, however, their best performance is only achieved when all three are combined together.

3.3.1 AA tracking

As previously stated, the AA algorithm [59] is one of the two algorithms responsible for taking the CFT and SMT hits (from the relevant unpackers) and performing pattern recognition to create possible track hypotheses which can then be passed onto the final filtering stage. The initial track hypotheses are constructed from 1-D clusters in the SMT barrels and disks, starting with the innermost layer and working out, allowing for stereo and axial hits to be considered separately. The track hypotheses are then extrapolated into the outer SMT and CFT layers and any hit that lies within a given expectation window is added to the track hypothesis if the resultant χ^2 is less than a predetermined maximum. If more than one suitable hit lies within the window then multiple track hypotheses are created.

Each of these hypotheses have only one axial projection, but can have many stereo projections, although the majority of these are removed due to missing hits in the stereo layer. Once a track reaches the last tracking layer, or once more than 2 layers have been found without suitable hits, the resultant hypothesis is saved if the track passes some basic quality cuts. The saved tracks are then ordered in terms of track quality (in order of number of hits, number of misses and track χ^2). Tracks which share hits are then considered independently and the worst quality track is removed.

Since this method uses the SMT as a seed for its track finding this means that any CFT only tracks will be missed, and so a second pass is conducted starting with the innermost CFT layer, and working outwards in the CFT before adding SMT hits, in order to recover missing tracks.

3.3.2 HTF tracking

The other pattern recognition algorithm run as part of the overall DØ data reconstruction process is the HTF algorithm [57]. This algorithm is based on the principle of Hough transformations [56] between (x, y) space and (ρ, ϕ_0) space, where ρ is the curvature and ϕ_0 the initial angle of the track.

The HTF algorithm uses this by performing searches starting in the axial CFT layers and then extending them into the stereo CFT layers and finally the SMT. The axial CFT tracks are found through histogramming the detector hits in (ρ, ϕ_0) space and the bins with the highest occupancy correspond to seeds for track finding. Axial CFT tracks that possess more than 7 hits then proceed to stereo CFT track finding and finally extrapolation into the SMT. Independently of the 'CFT into SMT' pass, the algorithm then runs a 'SMT into CFT' pass. This uses (ρ, ϕ_0) histogramming of the axial SMT hits to seed tracks and then both stereo SMT information and requirements on the number of SMT hits (≥ 4) to reduce the number of seeds and impose track quality cuts. The final selected SMT tracks are then extended into the CFT. The tracks from both passes are then combined together and duplicates removed. The resulting track candidates are combined with those from the AA tracking and passed onto the GTrack fitter for final filtering and fitting using Kalman filters.

3.4 Level 3 vertexing

The location of the primary vertex is an important input parameter for many Level 3 filters. The jet filters, for example, use the z coordinate to sharpen the jet trigger turn-on curves (that is to provide improved response at lower jet energies) and the

full 3-D vertex is used as input to the b-tagging filters [62]. The Level 3 vertexing algorithms are divided into two parts, a z vertexer and a $x-y$ vertexer [63]. The z vertexer, `L3TCFTVertex`, is run first, and provides a seed z position for the $x-y$ vertexer, `L3TXYVertex`. When combined together, these separate vertexers create a 3-D Level 3 vertex which is then used in the partial event reconstruction upon which triggering decisions are made. The $x-y$ vertexer is much more processor intensive than the z vertexer and requires the Level 3 tracking algorithms to reconstruct tracks down to a much lower momentum threshold than the the z vertexer, and so this particular tool is only run for select triggers. As in the case of the Level 3 tracking software, the vertexer must operate within the Level 3 time budget and so any algorithms used must be as fast as possible. A brief overview of each of these vertexers will be provided here.

The z vertexing algorithm uses a p_T weighted histogramming approach to find the location of the primary vertex in the z direction. All good quality tracks returned by the Level 3 tracking algorithms are binned in a histogram representing z, with the range -100 to 100 cm and a bin width of 1 cm, according to the Z_0 of the track. The number of tracks in each bin, n, is then multiplied by the total p_T of the tracks in each bin, $\sum p_T$. This results in each bin containing a value of $n\sum p_T$, the highest value of which corresponds to the most probable location of the z vertex. The hard scatter can be distributed over 1-2 cm and so the z vertex returned is the mean Z_0 value of the maximum bin and the two bins adjacent to it. The application of p_T weighting allows for the correct vertex to be chosen amongst any other minimum bias vertices. However, to avoid fake high p_T tracks from biasing the weighting, a maximum p_T weight of 10 GeV/c is imposed. An example of this vertexing technique can be seen in figure 3.3. This histogramming method will only return one primary vertex.

By approximating the tracks to straight lines, whilst in the vicinity of the primary vertex, it is possible to use an impact parameter minimisation algorithm in order to calculate the $x-y$ vertex position. The tracks which are found to be associated to the z vertex will then have to pass track quality cuts to improve the error on the $x-y$ vertex, and which will then be passed onto the vertexing algorithm itself.

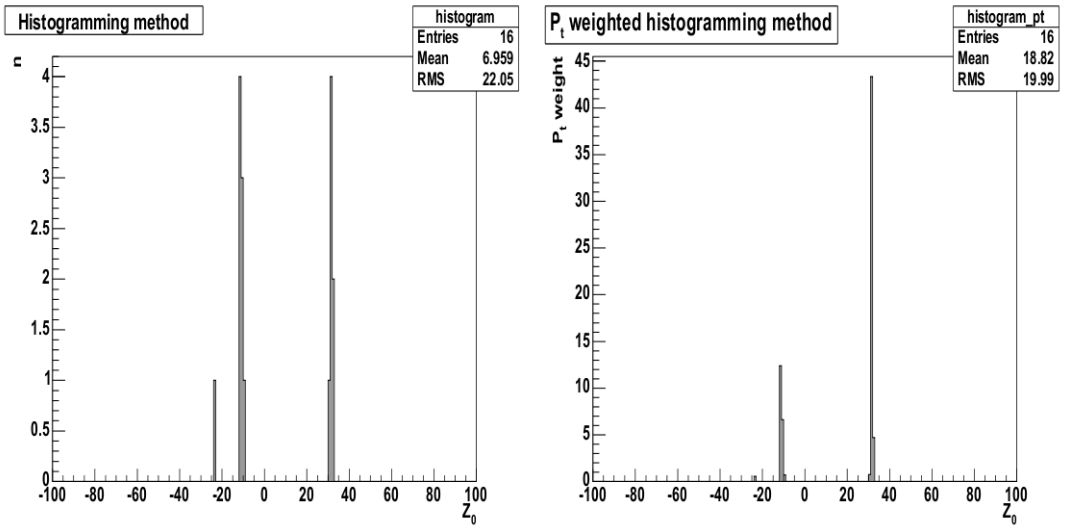

Figure 3.3: Comparison of the histogramming and p_T weighted histogramming techniques for the same sample $B_s \rightarrow D_s\pi$ Monte Carlo event. The Monte Carlo has had additional minimum bias events added with the probability following a Poisson distribution with mean = 0.8. The x axis displays the track Z_0 in 1 cm bins in the range -100 to 100 cm, whilst the y axis shows the number of tracks, n, for the histogramming method (left) or $n\sum p_T$ for the p_T weighted method(right). Without the p_T weight, the histogramming method finds the minimum bias vertex ($z \sim -10$ cm) rather than the hard scatter vertex ($z \sim +30$ cm) [63].

By transforming the system so that the beamspot is the origin, the minimisation method can be simplified to a simple 2x2 matrix dependent upon the angle θ_a, which is the angle between a given candidate track and the x axis as defined in the detector geometry. Details of the final position and error matrices can be seen in reference [63].

3.5 p16 Level 3 tracking speed increases

As the luminosity delivered to the DØ detector increases, the chance of two or more collisions occuring at the same time increase. This means that the tracking software will run slower at high luminosities due to the increased number of tracks, and hence we need to find ways of speeding it up so that the total Level 3 processing time remains within the 250 ms guideline.

A preliminary study of the tracking code indicated two possible ways of speeding up tracking by adjusting the input variables alone. These included both the reduction or

elimination of the dead fibre file in the CFT unpacker, which describes the location of broken fibres within the CFT and then artificially produces hits at these locations, and an increase of the p_T threshold with which the tracker is run. Both of these are brute-force methods of speeding up the tracker, but they can be applied online with relative ease.

3.5.1 The dead fibre file

The CFT is made up of over 70,000 scintillating fibres; however, not all of these are working, for example due to the failure of the waveguide fibres in the cryostat. The tracking algorithm works by taking clusters of hits from the CFT and then tracing the hit clusters back through the SMT to the primary vertex. If there are not enough hits within a region then a cluster will not be formed. Since the broken fibres will not register any hits, there may not be enough hits to create a cluster, particularly in regions with a large number of dead fibres. The dead fibre list contains the locations of the individual broken fibres and then turns these fibres back 'on' and hence if there are enough hits on adjacent fibres a cluster can be formed. This leads to an increase in the tracking efficiency. However, the inclusion of the dead fibre list also increases the time taken to process each event, and an investigation into the increase in tracking efficiency against the mean time taken per event was undertaken.

This was accomplished through the use of the DØ Level 3 tracking analysis software [64], and then investigating the effects of using the default dead fibre list, no dead fibre list and a reduced or stripped version of the dead fibre list to see where timing improvements can be made.

It was noticed from an analysis of the dead fibre list that there were a lot of consecutive dead fibres. This can be seen in figure 3.4. However, it was proposed that it may not be necessary to include all of the consecutive dead fibres due to there possibly being enough good fibres with hits on them to allow for the clustering to take place. This was accomplished by the removal of every other fibre in groups of two or more fibres.

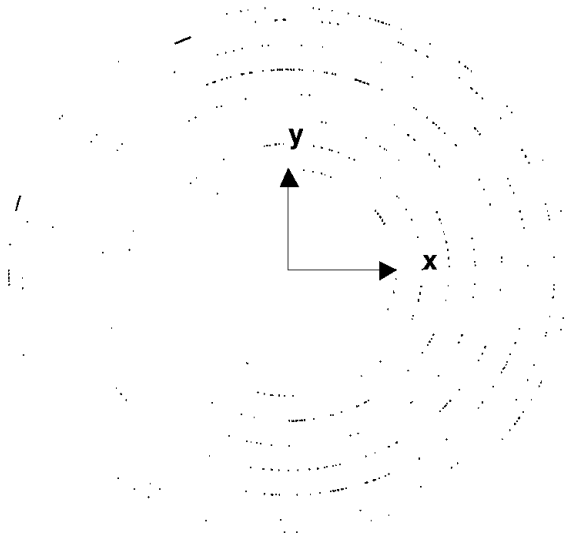

Figure 3.4: Diagram showing the axial location of the dead fibres in the the Central Fibre Tracker (CFT).

In this study the efficiency is defined as the tracking efficiency for the data sample averaged over all the dependent variables, (for example p_T, η and ϕ). The efficiency is defined in equation 3.1. Similarly the purity is defined as the tracking purity for the data sample averaged over all the dependent variables, and is given in equation 3.2.

$$\text{Tracking Efficiency} = \frac{\text{Number of good L3 tracks}}{\text{Number of findable reco tracks}} \tag{3.1}$$

$$\text{Tracking Purity} = \frac{\text{Number of good L3 tracks}}{\text{Number of L3 tracks found}} \tag{3.2}$$

A χ^2 test is used to match Level 3 tracks to d0reco tracks. The d0reco tracks used in the track matching process first need to pass the track quality cuts shown in table 3.1. These cuts are imposed to limit the d0reco tracks used in the matching process to those that could be found by the Run IIa tracker. Should a Level 3 track be successfully matched to a d0reco track then that track is said to be a good Level 3 track.

The data shown in table 3.2 correspond to a run that has previously passed the triggers and filters at Level 3, and has an instantaneous luminosity of $\sim 0.9\text{x}10^{32}$ $\text{cm}^{-2}\text{s}^{-1}$. Though rerunning on data which has already been triggered on will introduce a slight bias to the results, the scale of the bias is very minimal due to the nature of the test being conducted. Since only the tracking tool and SMT and CFT unpackers are being tested here, without any trigger conditions beyond p_T threshold, and the only the track results are being recorded. The tracking results presented here compare like-for-like tracks irrespective of physics content or trigger origin. In addition, when these studies were conducted no suitable Monte Carlo or unbiased data samples available. However, once other Level 3 components are added, or trigger-like quantities evaluated, then these biases need to be considered.

It can be seen in table 3.2 that the time taken changes significantly (217 ms to 279 ms) in going from the no dead fibres case to the case where the full dead fibre list is used. This corresponds to a small gain in the tracking efficiency from 0.428 ± 0.005 to 0.442 ± 0.005. The purity for these two cases is similarly affected. Now looking at a comparison between the stripped dead fibre list and the case where there are no dead fibres, an increase in the computing time from 217 ms to 262 ms for the stripped dead fibre list is observed. This corresponds to a tracking efficiency increase of 0.013 to 0.441 ± 0.05 from the no dead fibre case. It should be noted here that the actual timing values are dependent upon the type of CPU being used, and that when used in the Level 3 farm they will be reduced. However, the relative timings between the different dead fibre cases should be valid.

The small increase in efficiency with either the full or trimmed dead fibre files is outweighed by the longer tracking time required to process the increased number of CFT clusters. As a result of this study it was decided not to run the dead fibre file for the remainder of Run IIa.

14 total CFT hits required per track
0 SMT hits required per track
0 CFT axial hits required per track
Track must match to the primary vertex

Table 3.1: Table showing the cuts imposed on offline tracks used for track matching.

	Timing (ms)	Efficiency	Purity
No Dead Fibre List	217	0.428 ± 0.005	0.441 ± 0.005
Full Dead Fibre List	279	0.442 ± 0.005	0.410 ± 0.005
Trimmed Dead Fibre List	262	0.441 ± 0.005	0.411 ± 0.005

Table 3.2: Table of the results obtained from using the different dead fibre settings, with a p_T cut of 0.5 GeV/c.

3.5.2 Vertexing and p_T cuts

Another way of saving processing time is to simply reduce the number of tracks that will have to be processed by increasing the p_T cut used by the tracking algorithm. This would have the effect of removing all the track candidates with a p_T less than the specified value early on in the algorithm and hence reduce the overall computing load. The vertexing algorithm works by first finding a z vertex, and then using this to find a vertex in the $x - y$ plane. This then allows for the full 3-D vertex to be reconstructed. In addition the z vertex is used as the seed location for the jet tools [65]. The default setting is a p_T cut of 0.5 GeV/c. Through variation of the minimum track p_T an investigation into how vertexing efficiency and timing are affected can be conducted. For this study minimum p_T cuts of 0.5, 1, 2, 3 and 5 GeV/c are used. The vertex efficiency is calculated as shown in equation 3.3 below.

$$\text{Vertex Efficiency} = \frac{\text{Number of events with a vertex found}}{\text{Total number of events}} \tag{3.3}$$

The results for the z vertex efficiency study can be seen in figure 3.5. This was run on the same data set as was used for the dead fibre tests. In this case it can be seen that the vertex efficiency drops from 0.999 to 0.993 when going from 0.5 GeV/c to 1 GeV/c, and the timing decreases significantly, from 286 ms to 203 ms. This large timing decrease for only a small drop in the vertex efficiency means that following this course of action is plausible. As the p_T cut increases even further more and more vertices are lost for a large time saving, but the loss in vertex efficiency soon became unacceptable. Based on this information the p_T cut for the z vertexer was

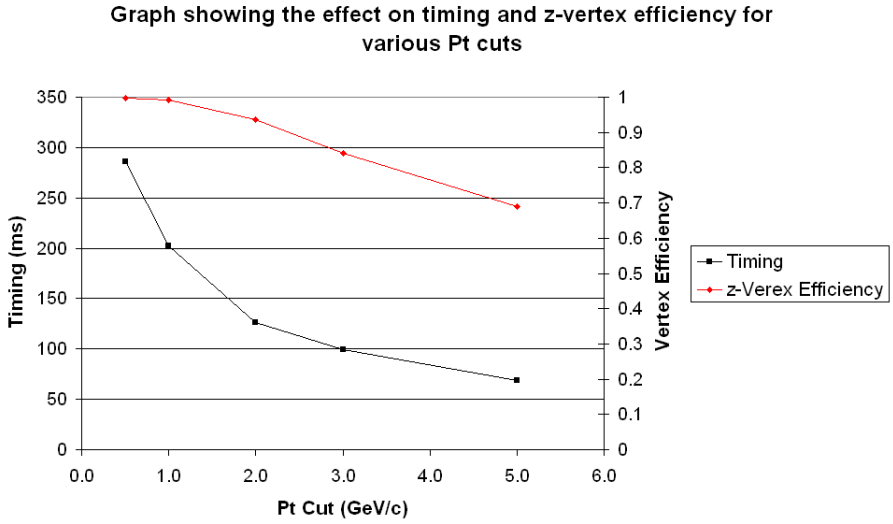

Figure 3.5: Graph to show the effect on timing and z vertex efficiency for various p_T cuts.

increased from 0.5 GeV/c to 3 GeV/c, which reduced the processing time by 188 ms for a ∼15% drop in efficiency.

The next step is to consider what happens to the $x-y$ vertexing when the same p_T cuts are used. Since this is dependent upon the z vertexing this means that a cumulative effect on the number of vertices located will be seen. However, due to the nature of the Level 3 algorithm there may not always be an $x-y$ vertex found for every z vertex previously found. Should this happen, then that event is assigned the run's beam-spot measurement as its Level 3 vertex. The results of this can be seen in figure 3.6.

As can be seen from figure 3.6 there is a very large drop in timing, as before, when going from the 0.5 GeV/c cut to the 1 GeV/c cut, 286 ms to 203 ms. However, this time there is also a large drop in the efficiency, from 0.814 to 0.673. This trend continues when the p_T cut is increased still further. This large drop in the efficiency comes from the fact that a lot of the vertices found when considering the z direction appear to have no corresponding $x-y$ vertex. At the lowest p_T cut used this effect is far less noticeable as all the vertices are still present. However, as the p_T cut increases a lot of the tracks are lost and hence a lot of the vertices cannot be reconstructed correctly.

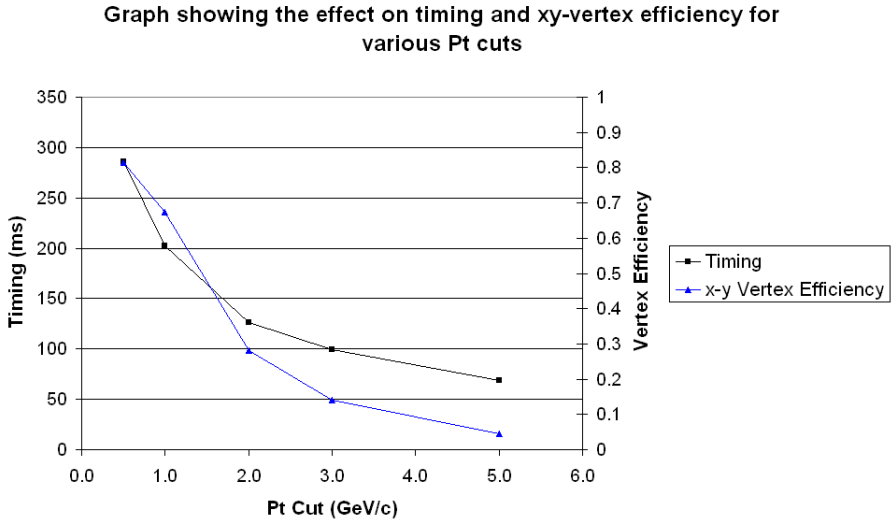

Figure 3.6: Graph to show the effect on timing and x-y vertex efficiency for various p_T cuts.

On the basis of this evidence, the decision was made to run the tracker at a p_T threshold cut of 3 GeV/c when only the z vertexer is required by the jet tool to help improve the sharpness of the turn-on curve. However, the decision was made to leave the p_T threshold at 0.5 GeV/c when the tracker is required for filters that use the $x-y$ vertexer, the observed large rapid drop in vertexing efficiency means that to run the tracker at a higher p_T threshold will adversely affect the trigger yields obtained.

3.6 p17 Level 3 tracking certification

The p17 release was designed to operate at higher Run IIa luminosities than p16 and as such needed certification for use on the Level 3 farms.

Several tracking related changes were made in p17 compared to the p16 release. These included a new, more efficient SMT cluster finding algorithm and an improved handling of the SMT clusters in the tracker itself. The SMT clustering algorithm was modified to include 'hot' chip killing (that is to reject any readout chip that reads as having $> 25\%$ occupancy), improved pedestal treatment, the merging of clusters (which allows for faulty strips to be accounted for), and improved clustering errors

and cluster splitting (which allows for two hits located close together to be read as separate smaller clusters rather than one large cluster) [66]. The improvements made to the tracker itself involved the inclusion of SMT 'barrel prediction'. This process uses the existing CFT stereo tracking algorithm to point towards the SMT barrels that will most likely contain silicon hits relevant to the track. This results in a reduced number of SMT hits per track, but an increase in track finding efficiency due to the removal of SMT clusters coming from an incorrect barrel [67].

The certification process tests and verifies that the software is suitable for use online. This requires a comparison between the p17 and p16 software and then an investigation into how each variable affects the new software, and an investigation of any further possible speed-up changes. These include looking in more detail at changing the p_T thresholds, and investigating whether or not the dead fibre file is needed. In addition to this, a small study was made into what effect, if any, the inclusion of jet criteria would have on tracking efficiency and vertexing. This needs to be completed using both data and Monte Carlo. For the certification results below data was used throughout.

3.6.1 p16 and p17 comparison

In order to see how the p17 tracking software compares to p16, the results obtained from running the p17 tracking algorithms need to be compared to those obtained using the p16 algorithms for the same data set. The results shown below use a (then) high luminosity run ($\sim$ 0.9x10^{32} cm^{-2}s^{-1}) and 5,000 events to obtain a reasonable number of statistics over which to run. They also use a p_T threshold of 0.5 GeV/c and both use the trimmed dead fibre list. The results can be seen below in table 3.3.

As can be seen in table 3.3, the p17 software is an improvement since it has a higher efficiency with only a slight increase in the time taken.

The vertexing efficiency does not change much between p16 and p17 as at a p_T of 0.5 GeV/c a z vertex is found nearly 100% of the time. This means that in order to

	p16 Results	p17 Results
Timing (ms)	265	288
Tracking Efficiency	0.433±0.002	0.535±0.002
Tracking Purity	0.412±0.002	0.410±0.002
Number of Tracks Found	23961	29616
z Vertexing Efficiency	0.9992	0.9996
$x-y$ Vertexing Efficiency	0.7745	0.8137

Table 3.3: Table showing the results of the comparison between p16 tracking software and the new p17 tracking software.

Luminosity Level	Run Number	Luminosity ($cm^{-2}s^{-1}$)
High Luminosity	206813	$0.95x10^{32}$
Medium Luminosity	206163	$0.55x10^{32}$
Low Luminosity	206333	$0.27x10^{32}$

Table 3.4: Table showing the instantaneous luminosities recorded for each of the luminosity levels used for the luminosity vs. p_T study.

study the effect of the increased number of tracks tests at higher p_T thresholds will be required. The efficiency for finding the $x-y$ vertex was found to increase going from p16 software to the newer p17 release. This is due to the larger number of tracks being found in p17 resulting in increased vertex efficiency, especially for the $x-y$ vertexing tool. In addition to this the z vertex efficiency is slightly increased and hence, since the $x-y$ vertexing tool is highly dependent upon the efficiency of the z vertexing tool, this means a slight increase will be seen here also.

3.6.2 p_T thresholds and luminosity

In order to further understand the effect of varying the p_T threshold with the new p17 software, studies of how the tracker performs on lower luminosity runs are needed. In addition to using a high luminosity run, medium and low luminosity runs were also used (see table 3.4). The results can be seen in figures 3.7 to 3.11.

As can be seen from the graph in figure 3.7 the timing plots all look similar for the different luminosities; that is that the tracker takes longer to run at the lower p_T values than at the higher ones. This is to be expected due to the higher number of

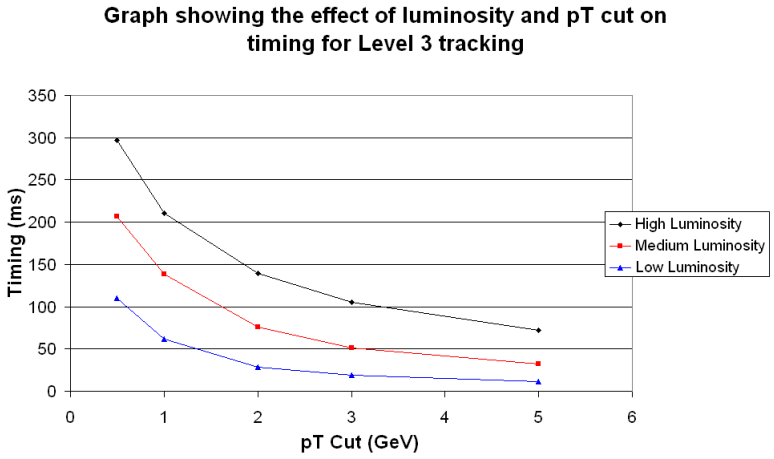

Figure 3.7: Change in tracking time as a function of luminosity and p_T.

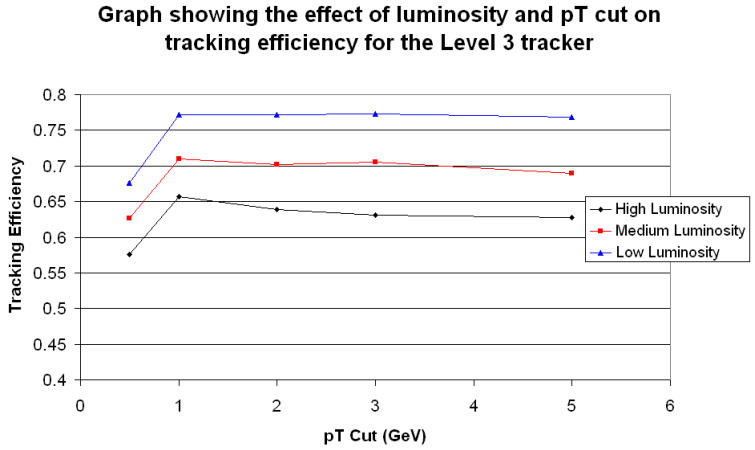

Figure 3.8: Change in tracking efficiency as a function of luminosity and p_T.

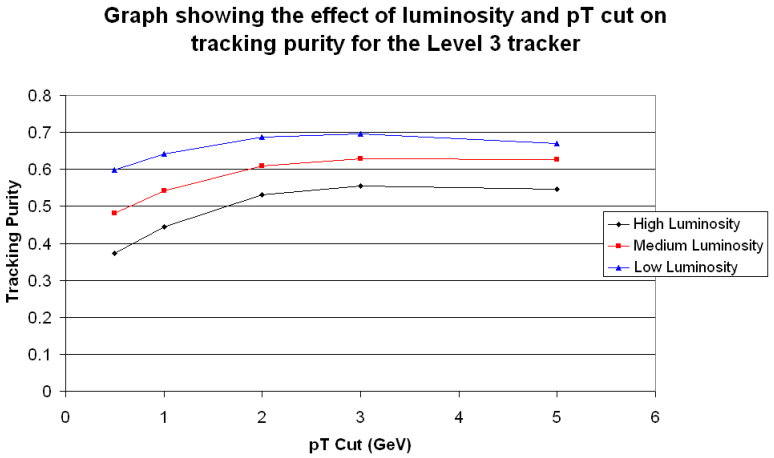

Figure 3.9: Change in tracking purity as a function of luminosity and p_T.

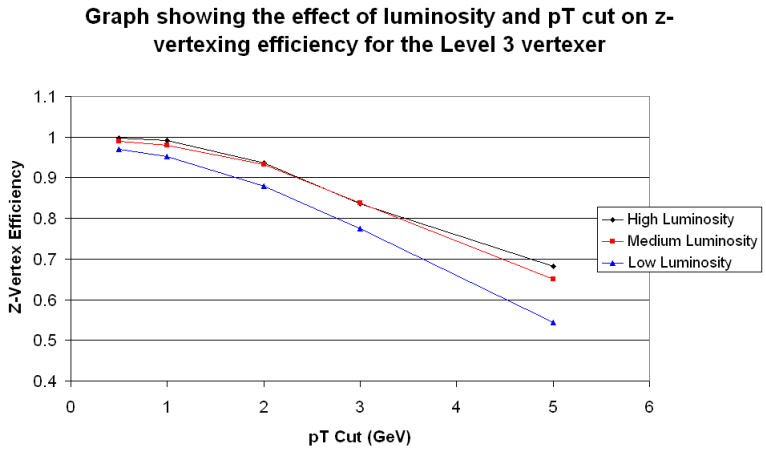

Figure 3.10: Change in z vertex efficiency as a function of luminosity and p_T.

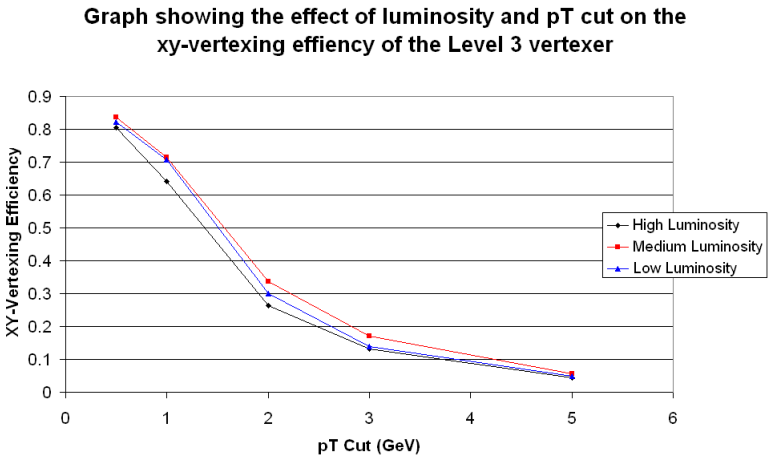

Figure 3.11: Change in $x - y$ vertex efficiency as a function of luminosity and p_T.

tracks that will pass the p_T threshold at lower values. In addition to this it can also be seen that, as expected, the lower luminosity runs take less time than those with higher luminosities. This effect can be seen in the tracking efficiency graph in figure 3.8 where the lower luminosity runs have a higher efficiency than those with higher luminosity. This is due to there being fewer hits in the lower luminosity runs and so the tracks will be easier to find. The same is true for the tracking purity in figure 3.9.

For the vertexing, it can be seen from the z vertexing efficiency (figure 3.10) that there is little difference in the efficiency when going from a high luminosity run to a medium one, and a slight decrease when moving to the low luminosity run. This is due to a decrease in the total number of tracks found at lower luminosities and hence the vertexing tool has a harder time finding the vertex with a reduced number of tracks. The $x-y$ vertexing efficiency, in figure 3.11, on the other hand is near identical for all three luminosities; this is again due to the high dependence the $x-y$ vertexing tool has on whether a z vertex is found or not. The slight differences in vertex efficiency are also partly due to the relative ease with which the $x-y$ vertexer can locate a vertex in lower luminosity runs. However, this is offset slightly by a reduced total number of tracks returned in lower luminosity conditions with which it can attempt the minimization stage of the vertexing algorithm.

3.6.3 The dead fibre list and high p_T

High p_T tracks are required for a lot of new phenomena physics, for example Higgs or Supersymmetry searches, and so as high an efficiency as possible is needed as new physics will most likely occur at a small rate. One way of increasing the tracking efficiency is to run the tracker with a reintroduction of the dead fibre file. Though the effects of the dead fibre file with an increased p_T threshold of 1 GeV/c had been previously looked at, a study of how it performs at higher p_Ts had not been.

By taking the ratios of both the efficiency and purity as a function of p_T for the case when the dead fibre file is used, and the case where it is excluded, graphs of the resulting ratio for each of the p_T bins can be produced. The ratio is defined

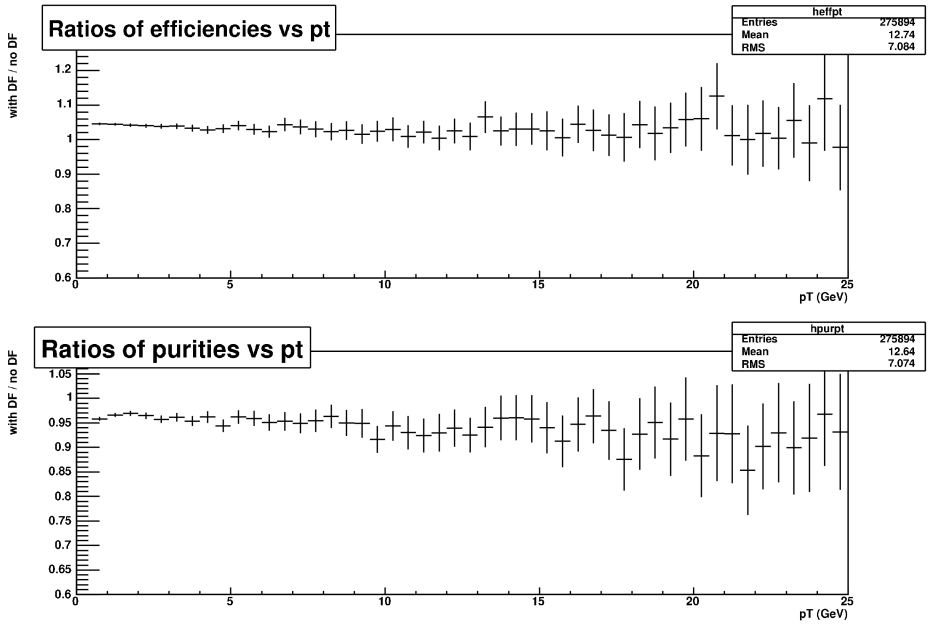

Figure 3.12: Graph showing the ratios, as a function of p_T, of the results when dead fibres are included to the results where no dead fibres are included, for both efficiency (top) and purity (bottom).

as being the case with the dead fibre file divided by the case without the file. The results of this can be seen in figure 3.12. Here it can be seen that the ratios have a flat distribution for both the efficiency and purity with an offset from 1 of about 4% in either case, greater than 1 for the efficiency and less than 1 for the purity. Though the results are fairly ambiguous at higher p_T, it is clear to see that there is no major effect to the results at these high values. This result is to be expected as the dead fibre file is used within the unpacker tool for the CFT and merely adds in a hit on every fibre listed in the file to those hits found in the CFT. This means that the same number of dead fibre hits will be present regardless of what p_T threshold the Level 3 tracking software uses and hence it will mean a roughly constant offset is found when comparing the case where it is used against the case where it is not used.

3.6.4 Vertexing and high E_T jets

One other thing to look at when considering searches for new phenomena is what happens to the tracking and vertexing system when the requirement of high energy

	p_T Cut = 1 GeV/c	p_T Cut = 3 GeV/c
Tracking Efficiency	0.690±0.003	0.669±0.006
Tracking Purity	0.472±0.003	0.600±0.006
z Vertex Efficiency	0.6408	0.5048

Table 3.5: Table showing the effect on tracking efficiency, purity and z vertex efficiency for high E_T jet cuts and p_T cuts of 1 GeV/c and 3 GeV/c using data that has passed through Level 1 and Level 2 only and hence has not been subjected to trigger bias.

jets in the event is imposed. For this study, either one Level 3 jet [65] with an $E_T > 30$ GeV, or two Level 3 jets each with an $E_T > 12$ GeV is required in the offline reconstruction. In addition, the location of the primary z vertex should be < 35 cm ($|Z| < 35$ cm) for the Level 3 vertices, where 0 cm is the centre of the detector. This allows for the simulation of the L3 filters that are used to look for new phenomena. Of particular interest is the effect the implementation of this filter has on the z vertex efficiency, tracking efficiency and purity at differing values of p_T. Since a large proportion of the triggers used online require the presence of jets, data used for this study are taken from a special run taken with Level 3 turned off. This then produces data that has not passed through any triggers and hence there will be no trigger bias. The results can be seen in table 3.5.

Table 3.5 contains details on what happens when p_T values of 1 GeV/c and 3 GeV/c are used. These are the p_T values used for the jet triggers at Level 3. It can be seen that whilst the tracking efficiency does not change much when going from the 1 GeV/c case to the 3 GeV/c case, the purity and the z vertex efficiency both change when going from one case to the other; the purity going up as the p_T is increased and the z vertex efficiency going down. In addition to this the vertex purity, the fraction of Level 3 vertices found compared to offline vertices was found to be constant for the two p_T values. This is to be expected given the definitions of each of these quantities. Since the $x-y$ vertex efficiency was previously found to rapidly decrease as the p_T is increased, with the extra jet cuts added in the efficiency became near zero for both p_T cases. Online currently uses 3 GeV/c for z vertex finding and 0.5 GeV/c for $x - y$ vertex finding.

3.7 Conclusions

Several studies were conducted on the p16 trigger software release, in order to reduce the time taken for the Level 3 tracking software to run. A trimmed dead fibre file was made through the removal of all adjacent dead fibres within the list, which resulted in a small drop in efficiency of about 0.1% for a time saving of 17 ms on average, compared to the full listing, whereas removal of the file resulted in a 1.4% drop in efficiency for a 62 ms time saving on average, compared to the full listing. For online data taking the decision was made to remove the dead fibre file.

The p_T cut studies showed that for the z vertex efficiency, a tracking p_T cut of 3 GeV/c led to an average timing saving of nearly 200 ms for a 8% drop in efficiency compared to the previously used 0.5 GeV/c. This is useful when considering those Level 3 filters which require only the z vertex to be reconstructed, for example the jet and missing E_T tools. This change was also made for subsequent data taking. However, the $x-y$ vertexer was found to show too significant a drop in efficiency when the p_T cut was increased by even 0.5 GeV/c, and so filters using that particular tool will still use an instance of the tracker that is run with a p_T cut of 0.5 GeV/c. All of these results were implemented online and helped reduce the time taken per event at Level 3.

The p17 release included improvements to the SMT algorithm in the tracker in the form of a barrel prediction algorithm to improve hit matching, and also improvements to the SMT unpacker itself. These improvements resulted in an increase in tracking efficiency of about 10% for a slight increase in tracking time.

Studies into tracking and vertexing dependency upon both p_T and luminosity revealed that tracker timing is reduced for lower luminosities and higher p_T thresholds. Tracking efficiency peaks at about 1GeV/c for all luminosities, with about 10% difference in efficiency between highest and lowest luminosities, whilst tracking purity studies reveal a plateau around 3 GeV/c for all luminosities.

The z vertexing results show an improvement with increasing luminosities, due to the histogramming method used being more efficient with a higher number of tracks,

and hence higher luminosity, whilst the $x-y$ vertexer shows a sharp decline for all luminosities with increasing p_T cut. Studies into the dead fibre file show that the efficiency improvement provided by the inclusion of the file is constant for all values of p_T, and when considering the specific case of high E_T jets and the two filters used, one with a tracking p_T cut of 1 GeV/c and one with a cut of 3 GeV/c, it is observed that the z vertex efficiency (as used in the jet filter itself) drops by nearly 15%, whilst the tracking efficiency only falls by $\sim$2%. Shortly after these certification plots were approved, the p17 Level 3 tracking software went online and was used until the end of Run IIa.

Chapter 4

DCA error parameterization and the Run IIb Level 3 tracker

4.1 Preface

This chapter describes the necessary upgrade in the Level 3 tracking software from the Run IIa tracking software, `L3TGlobalTracker`, to the Run IIb tracking software, `L3TCFTTrack`, in order to deal with the increased luminosity of Run IIb. In order to increase vertex finding efficiency, and improve vertex resolution, the new software requires properly calibrated track errors, and DCA errors in particular.

The DCA errors are derived by parameterizing the errors in terms of the number of SMT hits and p_{scat}, where p_{scat} is the track p_T scaled by the stereo pitch angle of the track and accounts for multiple scattering within the detector (equation 4.2). Once a new set of errors has been derived, they are then tested on both Monte Carlo and data samples by investigating how the DCA significance varies as a function of both p_{scat} and the number of SMT hits, and by looking at how the vertexing performance is effected by use of the new errors.

4.2 Level 3 and Run IIb

The DØ detector underwent substantial upgrades between Run IIa and Run IIb. These upgrades, as previously mentioned, included improved Level 1 triggering hard-

ware, particularly for the calorimeter subsystem, and the inclusion of a new layer of silicon within the SMT, Layer 0. The Level 3 software trigger also underwent upgrades to its algorithms and farms as part of the overall Run IIb upgrade.

As seen in chapter 3, the Run IIa Level 3 tracking software, `L3TGlobalTracker`, was found to struggle greatly as the luminosity, and hence the event complexity, increases. As such, a new set of tracking algorithms were designed for use in Run IIb that would provide similar, or better, performance than the Run IIa algorithms but at a fraction of the total processing time. Combined with upgrades to the Level 3 farm itself, the tracking software upgrades are designed to allow the Level 3 triggering system to cope with the highest luminosities delivered by the Tevatron*. In addition to this the addition of new tracking hardware, in the form of Layer 0, would have meant substantial changes were needed to the Run IIa software in order to incorporate the new silicon, due to the current way the SMT is coded into the algorithms. The use of new tracking code allows for changes to the silicon to be included from the beginning to allow for easy switching between Run IIa and Run IIb silicon readout modes.

4.2.1 The Run IIb tracking software

The new tracking software, `L3TCFTTrack` [68], was based on an existing CFT only algorithm, using the existing code as a starting basis for the CFT algorithms and then adding in new code to allow for track extrapolation into the SMT barrels. Similarly to the Run IIa tracking software, `L3TCFTTrack` assumes the tracks to be perfect helices and neglects multiple scattering within the detector. It also begins the track finding process by seeding from the CFT axial layers as `L3TGlobalTracker` does, however, it does so differently.

The CFT axial algorithm, like the one used in the Run IIa Level 3 tracking software, uses the assumption that the tracks can be considered as being perfect helices that lie close to the Z axis of the detector. The algorithm first calculates all potential

*The Tevatron is currently producing peak instantaneous luminosities of $\sim 3.5\text{x}10^{32}\text{cm}^{-2}\text{s}^{-1}$.

links between 2 axial clusters within the CFT, using a specified minimum p_T to set the maximum difference in ϕ between clusters in adjacent CFT layers. Since the location of the clusters in each of the layers is known, a 2-D histogram of $d\phi/dR$ versus ϕ_0 can be made, and the algorithm then tries to combine all the different links together using the maxima found in the 2-D histogram as seeds for the combines. The link combinations, or roads, are then searched for one or more viable candidate tracks. The road searching allows for the more time-consuming track finding stage to be limited to regions in ϕ where tracks are most likely to be found. Tracks are made by starting in the outermost layer of the CFT and adding links whose outer cluster corresponds to the innermost cluster of the track, with new candidates being created if more than one link can be added. Missing links are accounted for by joining together shorter chains to account for hit inefficiency.

For track candidates with at least 6 CFT clusters a circle fit is attempted and for those candidates with less than 7 axial CFT hits an attempt is made to recover clusters using the circle fit to predict the ϕ location of potentially missing clusters, and the closest cluster to this prediction is included and the track refit. If the χ^2 of the modified track is below a given threshold, defined as needed by the user, then the modified track is saved, otherwise the original track is retained. Tracks which pass given quality cuts are then saved and passed onto the final stage of the axial track finding, the elimination of duplicate candidates. Tracks are sorted first by the number of associated clusters, then by lowest χ^2, and any tracks that share more than two clusters with previously accepted tracks are then discarded. The results of this are passed on to the CFT stereo tracking algorithm next.

The Run IIb tracking algorithm uses a histogramming technique, based on a Hough transform, of the candidate Z coordinates from the CFT stereo layers, similar to that used in the Run IIa version. By performing the Hough transform the stereo solution for a track, as found by the axial algorithm, corresponds to the intersection of up to 8 lines (one per CFT layer) in the $(\tan\lambda, z_0)$ plane. Due to the limited resolution of the fibre tracker these lines will not intersect at a precise point, so another way must be found of estimating the intersection point, and one which will find a solution in a reasonable processing time. The chosen method is to fill two separate $(\tan\lambda, z_0)$

histograms, offset by half a bin in each axis so as to represent the resolution of the detector. Any bins that are above a given maximum height are hence considered potential solutions for the track. These potential solutions are then used to define a road in Z for each stereo CFT layer, and the closest cluster found on each layer is used in a straight line fit in order to obtain appropriate stereo parameters. The cluster combination that provides the greatest number of hits (above a minimal limit of 3 hits) and lowest χ^2 is then kept as the stereo solution for the track.

By comparison, the extrapolation of the track into the SMT is much simpler than the CFT track finding. The CFT only track is projected into the SMT beginning with the outermost layer first and working its way inwards, using the stereo track information to point towards the barrel containing relevant clusters to the track. For each axial layer of the SMT the two closest clusters to the extrapolated track, within a ϕ window defined by the user, are tried as possible additional clusters and a new temporary track is created, circle and line fits performed and the result used to project into the next layer of the SMT. Any track whose χ^2 is within predefined limits is retained, otherwise the original input track is used for the layer projection. At each layer there may be one or two input tracks that can each be extended by two possible clusters, hence this can lead to up to four possible tracks as input to the next layer. To prevent this combinatorial effect from blowing up, and hence leading to 512 candidates by the time the track reaches the innermost layer, only the best two candidates are selected to project onto the next layer. Once the track reaches the innermost SMT layer, the algorithm returns the best track candidate as determined by the number of hits and the track χ^2. The number of layers that the SMT algorithm traverses is variable and is calculated from the silicon geometry as returned by the Level 3 SMT unpacker, this allows for the tracker to run with or without Layer 0 included.

For any layer that returns an SMT axial cluster, the SMT stereo tracking algorithm attempts to add stereo clusters to the track. The clusters are chosen in a very similar way to that used to find the axial clusters and, again, only the two best candidates at each layer are chosen to progress to the next layer. Once this process is completed the single best track candidate is returned, as determined by number of hits and fit

χ^2. This entire process, from stereo CFT through to stereo SMT cluster tracking, is run for every possible track candidate returned by the axial CFT algorithm, the final result being a collection of tracks that correspond to a given minimum in desired track p_T. This minimum p_T is defined in the trigger list and is variable depending upon which Level 3 tools and filters are required to run for a given event.

4.2.2 Comparison between Run IIa and Run IIb Level 3 tracking algorithms

One of the main reasons for the design of a new set of tracking algorithms in Run IIb was to help reduce the total time taken to run the Level 3 trigger suite at high luminosities. However, another design requirement for the tracking algorithms is that they are at least as efficient as the Run IIa algorithms, otherwise trigger efficiencies will drop and impact physics data taking, whilst at least maintaining the track parameter resolutions of the Run IIa algorithms. To ensure that these design requirements are met a comparison between the two tracking algorithms is shown below. This comparison follows the same procedure as detailed for the p16 versus p17 Run IIa tracking software comparison in section 3.6.1. The data used for this comparison consists of 5000 events from run 213821, which was taken under normal data taking conditions and which had an initial luminosity of 1.08x10^{32} $cm^{-2}s^{-1}$. The results are shown in table 4.1. For these tests a new Run IIb dead fibre list was used.

	Run IIa tracker	Run IIb tracker
Efficiency	0.639 ± 0.001	0.739 ± 0.001
Purity	0.349 ± 0.001	0.284 ± 0.001
Mean Tracking Time (ms)	357.1 ± 19	303.5 ± 17

Table 4.1: Comparison of tracking performance between the Run IIa and Run IIb Level 3 tracking algorithms. These results were made using 5000 events of medium luminosity data excluding Layer 0 readout.

As can be seen in table 4.1, the Run IIb tracking software performs better on this particular data sample in terms of both efficiency and timing. Even though the loss in purity will result in more fake tracks being produced in the new tracker, the 10%

increase in overall efficiency, that is a 10% increase in the number of correct tracks when compared to d0reco output, coupled with the time saving is a more than sufficient improvement in Level 3 tracking. It is also worth noting that the Run IIb software also reduces the number of events whose total tracking time exceeds 1 second. These outlying timings are another reason for the need to upgrade the online tracking software.

4.3 The need for DCA errors

Some of the most important tools in use at Level 3 are those based on the analysis of tracks not coming from the primary vertex but from a secondary vertex, for example the lifetime and b-tagging tools. The primary vertex is found using the vertexing methods described in section 3.4, whilst the lifetime and b-tagging tools use their own methods to locate which tracks come from a secondary vertex. The design of the Level 3 system is such that the replacement of the old Run IIa tracking algorithms with the new ones, as described above, is transparent to the vertexing software, and as such no modifications were made to the vertexing code in order for it to use the new tracking algorithms (or to use Layer 0 once it was enabled for use at Level 3).

The vertexer itself is split into two separate components, each run individually as required by the trigger system, the z vertexer and the $x-y$ vertexer. The $x-y$ vertexer takes the tracks returned by the tracking software as its main input to vertex finding (the z vertex and the DAQ beam spot estimation being the other inputs), and in particular the track DCA and DCA errors are used in the vertex finding algorithm. The tracking algorithms, however, do not return errors along with the calculated track parameters due to the time taken for parameter errors to be calculated. This means that an alternative way is required to obtain the errors, and this process involves parameterizing the DCA error in terms of track momentum and the number of axial SMT hits associated to a track.

The resolution of the $x-y$ vertexer is very dependent upon the track's DCA error, as well as upon the DCA itself. As such it is important to get the error parameterization

as accurate and as detailed as possible. An incorrect DCA error parameterization will result in a broader vertex resolution, and thus the resolution and efficiencies of those tools dependent upon vertex resolution will also be impacted. To test the dependency of the vertex upon the DCA errors, the previously calculated errors from the Run IIa tracking algorithms can be imported into the newer Run IIb algorithms and an investigation into the vertex results conducted.

Figure 4.1 shows both the x and y vertex resolutions, and figure 4.2 shows the number of tracks associated to the found vertex. This test was run using special Monte Carlo produced with a beamspot fixed at (0,0) in (x, y), as opposed to producing a randomly distributed beam spot as per normal Monte Carlo generation. This Monte Carlo is discussed in more detail in the next section. Only the tools necessary to run the $x - y$ vertexer will be used here, that is the unpackers, the tracking algorithms and the z vertexer, but those tools will be run using the parameters described in the trigger list. The tracking algorithms are run using a minimum p_T threshold of 0.5 GeV/c to obtain the maximum efficiency in the vertexing algorithm. The results here can be compared to those shown in figures 4.8 and 4.10 after new errors have been derived and implemented for the number of tracks and vertex resolutions respectively.

4.4 Deriving new errors

The DCA error parameterization process used for the Run IIb tracking algorithms is based upon the method used for the Run IIa algorithms [63], but with several improvements included to improve the quality of the errors obtained.

The dominant contributions to the track DCA error are the number of SMT hits and multiple scattering within the fiducial tracking volume. As such the DCA error will need to be parameterized in terms of these two variables. Multiple scattering in the plane transverse to the the beam is expected to be inversely proportional to p_T, where $p_T = p\sin(\theta)$ and θ is the polar angle relative to the z axis. In addition to this, multiple scattering is found to be proportional to the square root of the distance

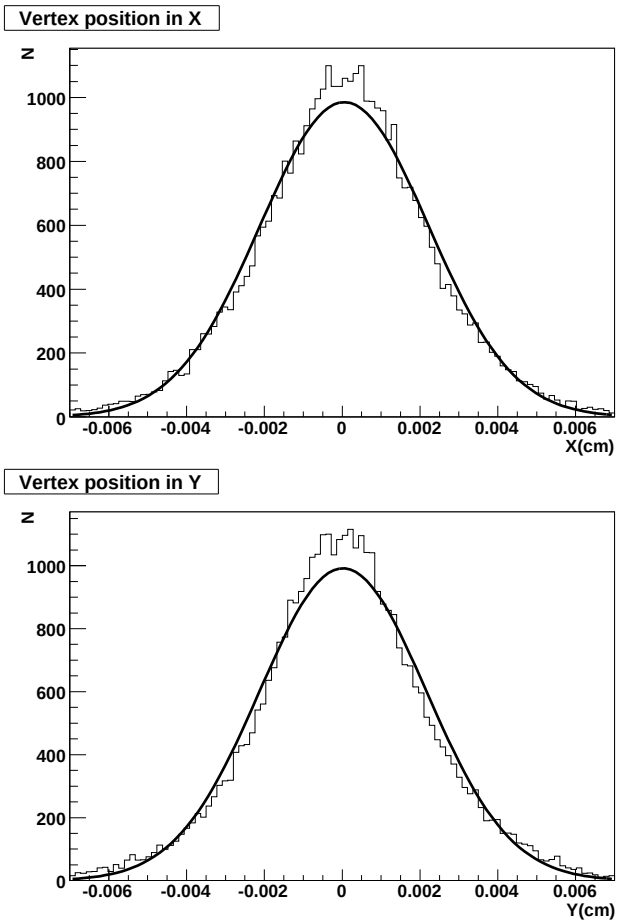

Figure 4.1: x (top) and y (bottom) vertex resolutions for QCD Monte Carlo made using the DCA track errors from the Run IIa tracking algorithms within the Run IIb algorithms. The x resolution is 21.7 $\pm$ 0.1 μm, and the y resolution is 21.4 $\pm$ 0.1 μm.

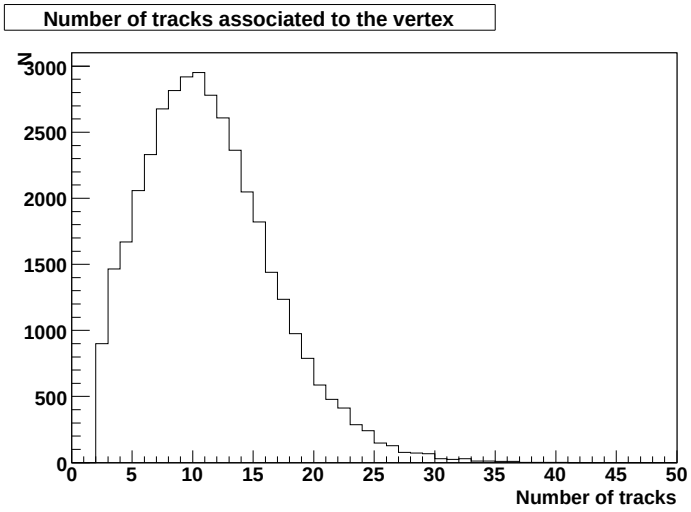

Figure 4.2: The number of tracks associated to the vertex in QCD Monte Carlo made using the DCA track errors from the Run IIa tracking algorithms within the Run IIb tracking algorithms. The mean number of associated tracks here is 10.90 ± 0.03.

travelled through the tracking medium [69]. The simplification that the material within the tracking volume is arranged into concentric cylinders aligned with the beam axis means that the multiple scattering distance is inversely proportional to $\sin\theta$.

By defining a new variable, p_{scat}, such that:

$$p_{scat} = p \sin^{3/2}(\theta) \tag{4.1}$$

it is found that multiple scattering is thusly inversely proportional to p_{scat}. Rewriting this in terms of the five helical track parameters, p_{scat} becomes:

$$p_{scat} = p_T \sqrt{\frac{1}{\sqrt{1 + (\tan(\lambda))^2}}} \tag{4.2}$$

The total DCA error, including the beam width in both x and y, σ_{beamx} and σ_{beamy} respectively, is given by:

$$\sigma^2_{DCA} = (\sigma_{nSMT})^2 F(p_{scat})^2 + \sigma^2_{beamx} + \sigma^2_{beamy} \tag{4.3}$$

where σ_{nSMT} is the error due to the number of SMT hits on the track. $F(p_{scat})$ is the unknown quantity that results from multiple scattering within the detector, and is what needs to be found in order to obtain correct DCA errors for vertexing purposes. The beam locations, tilts and widths are measured independently of the Level 3 triggering system by one of the DAQ examine programs, `vertex_examine` [70], and then passed to the Level 3 system periodically. The beam position in data is not only displaced in terms of x and y but also has a tilt component in the z direction. This is assumed to be linear and is expressed as:

$$x = X_0 + A_x z \qquad y = Y_0 + A_y z \tag{4.4}$$

where X_0 and Y_0 are the measured displacements from the origin and A_x and A_y are the measured beam tilts.

The previous error analysis found that at low p_{scat} there was a large error occuring from multiple scattering effects, and at higher values of p_{scat} the error from multiple scattering effects was reduced, due to the inverse proportionality between the two quantities. Additionally, at large values of p_{scat} it was noted that the DCA significance, given by DCA/σ_{DCA}, was offset from one [63]. Taking these conditions into consideration a functional form for $F(p_{scat})$ can be made:

$$F(p_{scat}) = \sqrt{c_0^2 + c_1^2/p_{scat}^2} \tag{4.5}$$

where c_0 and c_1 are constants. By binning track DCAs in both p_{scat} and the number of SMT hits and then fitting the resulting distributions with Gaussians thus obtaining the DCA resolution in that bin, empirical values for the constants can be derived from fits of DCA resolution versus p_{scat}. For this process p_{scat} bin widths of 1 GeV/c will be used starting from 0.5 GeV/c, and SMT hit bin widths of 1 will be used in a range from 0 hits to $\geq$5 hits. There are few tracks with >5 SMT hits, and there is very little change in the error obtained by adding >5 hits, and so all these tracks are added together into the 5 SMT hit bin. Since the distribution is

expected to converge asymptotically to c_0 at high values of p_{scat} an upper range of 20.5 GeV/c is used. The end result will be values for c_0 and c_1 for every SMT bin used and thus error functions for every SMT bin.

4.4.1 The testing sample

Equation 4.3 shows that the total error is dependent upon not only the SMT hit errors and multiple scattering effects but also upon error in the measurement of the beamspot. So, to obtain the components of the errors relating to the tracking, as defined in the previous section, the beam measurement will need to be well known.

Since the beamspot has a non-zero width in data, and given that there is always an uncertainty in beamspot measurement, these error studies are performed using Monte Carlo instead. The chosen Monte Carlo for the error parameterization was QCD background events, generated using Pythia [71]. These events were generated with the hard scatter vertex fixed at (0,0) in (x, y). This particular point is where the tracking algorithms assume all the tracks originate from when creating track hypotheses, and thus this vertex location should be used to obtain the most accurate DCA errors possible. A QCD sample was chosen due to QCD processes producing a lot of tracks of various momenta, as well as various other phenomena, including jets, with which tests can be run.

4.4.2 Sample selection

Since QCD processes produce many different types of event topology, selection cuts are needed to choose only the appropriate events. Of particular interest are the b-tagging tool and lifetime tool. These tools have similar selection criteria, and these criteria will be used to select suitable tracks and events from which to derive the DCA errors.

The selection criteria are split into two groups, event selection criteria and track selection criteria. The event selection criteria are as follows:

- z vertex within the SMT ($|z| < 35$ cm)
- ≥ 2 jets with an $E_T \geq 12$ GeV

Events which pass those criteria are then passed to the track selection. The track selection criteria relate the location of a particular track to both the z vertex (which is independent of track errors) and a nearby jet, as found by the relevant Level 3 tools. These criteria are:

- z_0 of the track within 2 cm of the z vertex
- Track must be within a 45° cone of the nearest jet

All tracks which pass the criteria will then have their DCA value binned into the appropriate p_{scat} and SMT bin.

4.4.3 Fitting the DCA distributions

Once all tracks have been selected, and appropriate candidates binned into the correct p_{scat} and SMT bin, each of the bins can then be fit to in order to extract a DCA resolution for that particular p_{scat} range and SMT value.

A double Gaussian function is used to fit the DCA distribution, as shown by the example distribution and fit in figure 4.3 for the bin containing tracks with 2 SMT hits in the p_{scat} range from 2.5 to 3.5 GeV/c. The mean width of the two Gaussians, both with a mean value of 0 cm, weighted by their respective normalization constants, is then taken as the DCA resolution for that p_{scat} and SMT bin.

4.4.4 Fitting the overall distribution

Now that all the bins have been fit by Gaussians, in order to obtain DCA resolutions, a DCA resolution versus p_{scat} plot can now be made for each SMT bin, so as to extract values of c_0 and c_1 for each SMT bin.

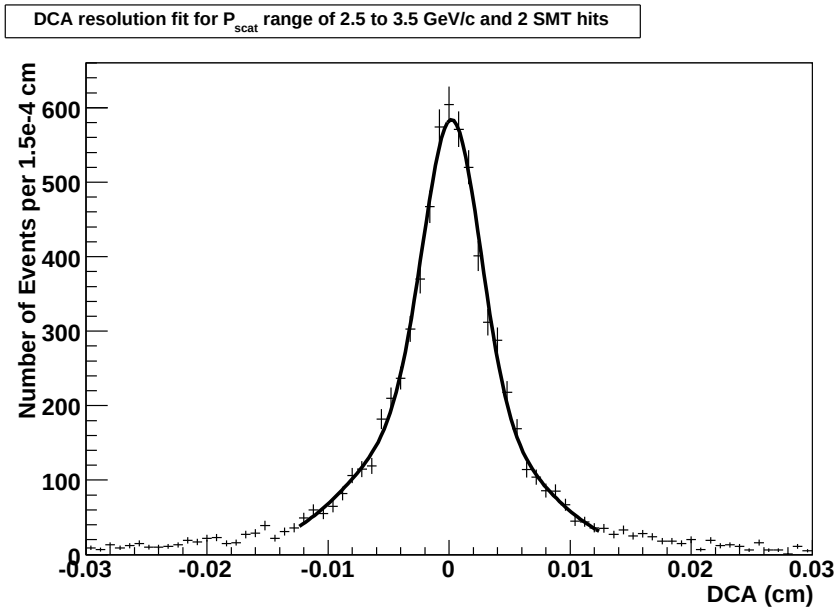

Figure 4.3: Sample DCA distribution fit for a p_{scat} range of 2.5 to 3.5 GeV/c and 2 SMT hits. A double Gaussian function has been fit to this distribution and the weighted mean width of the two Gaussians was found to be 37.7 $\pm$ 3.1 μm.

Before the final distribution is obtained though, each of the Gaussian fits must pass loose quality cuts for the corresponding DCA resolution to be included in the graph. This involves cutting on the χ^2/NDF of the fit, where NDF is the number of degrees of freedom for the fit, and removing those fits which fail the cut. A further attempt is then made to refit the distribution and the χ^2/NDF condition is tested again. The χ^2/NDF cut used is $\chi^2/NDF < 10$. An additional check is made to ensure that the DCA resolution, and the error on said resolution, are within reasonable limits, that is to say the DCA resolution is < 1 and the error is < 0.1. The limited number of events provided by the Monte Carlo sample will mean that some bins, especially those with higher values of p_{scat} and lower number of SMT hits, will not have sufficient statistics to enable a fit to converge properly.

The resultant DCA resolution versus p_{scat} graph can be seen in figure 4.4. Due to the differences in scales between 0, 1 and 2+ SMT hits, the former are drawn on separate axes to the higher SMT bins. It should be noted that though values are obtained for the 0 and 1 hit bins, these are never used by either the $x - y$ vertexer or any of the other tools which require DCA errors to be calculated. By fitting the

function described in equation 4.5 to each of the distributions values for c_0 and c_1 are found. These values are shown in table 4.2.

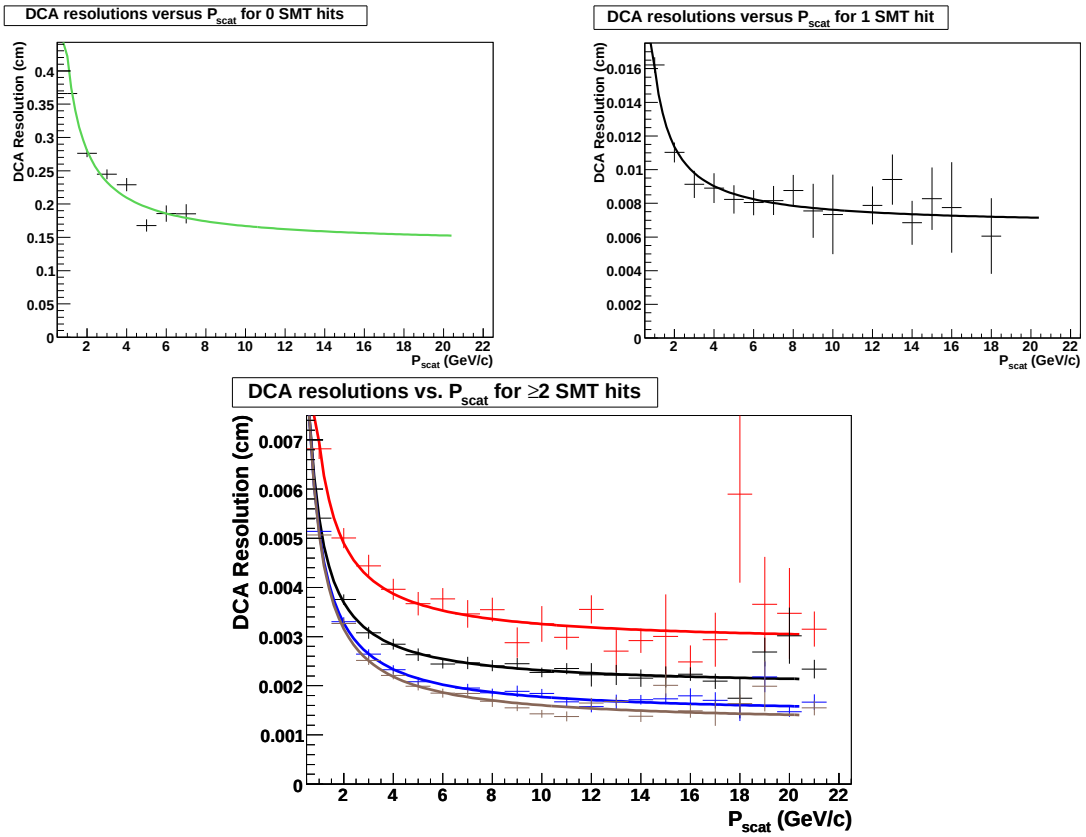

Figure 4.4: DCA resolution versus p_{scat} graphs for each of the six SMT hit bins. Each of the distributions are fit according to the function shown in equation 4.5. The first distribution is for 0 SMT hits, the second for 1 SMT hit. The plot showing many distributions contains, from top to bottom, 2 (red), 3 (black), 4 (blue) and $\geq$5 (brown) SMT hits. The locations where the distributions lack entries for a particular range of p_{scat} values represent where the Gaussian fit to that distribution has failed.

4.5 Testing the new errors

Now that the errors have been obtained they need to be verified. This is done by first checking the DCA significance as a function of p_{scat} and number of SMT hits, where DCA significance is defined as:

$$\text{DCA Significance} = \frac{\text{DCA}}{\sigma_{DCA}} \tag{4.6}$$

Number of SMT hits	c_0	c_1
0	0.136 ± 0.008	0.448 ± 0.02
1	0.0082 ± 0.0009	0.019 ± 0.001
2	0.0042 ± 0.0001	0.0089 ± 0.0002
3	0.00352 ± 0.00004	0.0081 ± 0.0001
4	0.00295 ± 0.00003	0.0069 ± 0.0001
≥ 5	0.00284 ± 0.00001	0.0069 ± 0.00002

Table 4.2: The values of c_0 and c_1 derived from the fits performed to the DCA resolution versus p_{scat} distributions shown in figure 4.4.

If the errors have been calculated properly then the DCA significance versus p_{scat} distributions should be flat around a significance resolution of 1. This test can be run on both the same QCD Monte Carlo as before, and on data to produce the significance distributions. The data chosen were 60,000 events from run 213821, which had an initial luminosity of 1.08x10^{32} $cm^{-2}s^{-1}$. The sample data consists of events taken under normal data taking conditions. This means that the data sample could contain a small amount of long lived particles from heavy flavor production. The long lived particles will introduce a slight bias to the high positive side of the DCA significance distribution. However, the relatively small quantity of long lived particles compared to other shorter lived ones, and the fact that only the centre region of the distribution around 0 is used to test the DCA errors (as explained in section 4.5.1) means that the effect of the long lived particles on the results is very minimal.

The raw data collected are reconstructed using the Run IIb tracking software and the new errors and the same procedure as used for the Monte Carlo. The tracks are then passed to the $x-y$ vertexer which then calculates an appropriate primary vertex for the event. Once found the tracks then have their parameters recalculated with respect to the returned vertex, as opposed to (0,0) as returned by the tracking algorithms. This process allows for the total true DCA to be found and also the total true DCA error. Both the data and Monte Carlo events are subject to the track and event selection criteria described in section 4.4.2.

Equation 4.3 shows that the total track DCA error is dependent upon both the newly measured track errors, parameterized in terms of p_{scat} and number of SMT

hits, and also upon the beam width. This means that to consider the total DCA error, values for the beam width must be included. For the data sample this is simple and involves inputting the values measured online for the beam width, location and tilt and recalculating the total error within the vertexer. However, for the QCD Monte Carlo this is slightly harder. Since the beam spot is always at (0,0) for every event this requires simulating both the beam width and the position of the beam spot. By convention the beam width is always taken to be 30 μm, as it is in real data. The beam position is simulated by a Gaussian distribution with a 30 μm width around (0,0) for both the x and y positions. The result is a simulation of beam position which will correctly modify the beam spot when used in the formulae shown in equation 4.4, where the beam tilt terms are assumed to zero.

4.5.1 Fitting the DCA significance

Once the DCA significances of all tracks which pass the selection requirements have been input into the appropriate p_{scat} and SMT bin, the distributions need to be fit to in order to extract a resolution for that bin. In this case a double Gaussian fit is used, similar to that used previously, and the weighted mean width of the two Gaussians is taken to be the DCA significance resolution for that particular p_{scat} and SMT bin.

A sample DCA significance distribution and fit can be seen in figure 4.5. The distribution seen here is for the p_{scat} range 2.5 to 3.5 GeV/c and 2 SMT hits and is made using the Monte Carlo sample.

4.5.2 DCA significance resolution distribution

To obtain the overall DCA significance resolution versus p_{scat} the widths of the Gaussian fits in each of the bins are taken and plotted against the entire binned p_{scat} range. Similarly to the the derivation of the DCA resolution functions, this is done separately for each of the six possible SMT hit bins. Also, the individual fits

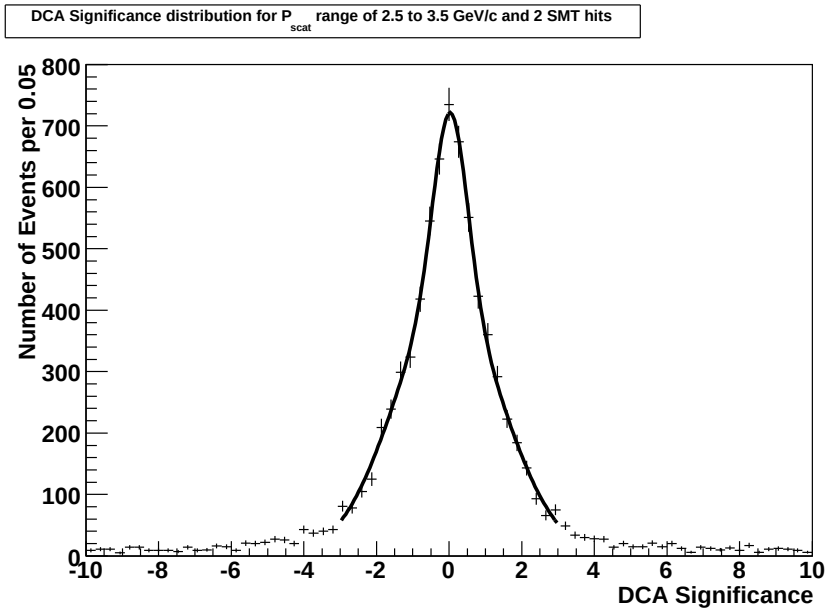

Figure 4.5: Double Gaussian fit to DCA significance distribution for a p_{scat} range of 2.5 to 3.5 GeV/c and 2 SMT hits. The weighted width for this fit is 1.04 $\pm$0.04, which shows that the derived error parameterization works for this particular p_{scat} and SMT bin.

must pass the same selection cuts as described in section 4.4.4 to remove those bins where the fit fails due to a lack of statistics.

Figure 4.6 shows the distributions for all SMT bins for the QCD Monte Carlo, whilst figure 4.7 shows the distributions for all bins for the previously described data set. These graphs show that the DCA significance for both the Monte Carlo and data are close representations to the desired uniform distributions with values for each bin lying close to 1. As before, the online tools require a minimum of 2 SMT hits in order for a track to pass selection cuts and for that track to be passed onto the vertexing algorithm. This means that the deviation from 1 observed in the 0 and 1 SMT hit bins will not have an effect on the vertex results as these tracks will not be used.

4.6 $x-y$ vertexing results

The final check of the measured DCA values is to investigate what happens to the $x-y$ vertex once the new parameterized errors are input into the tracking software.

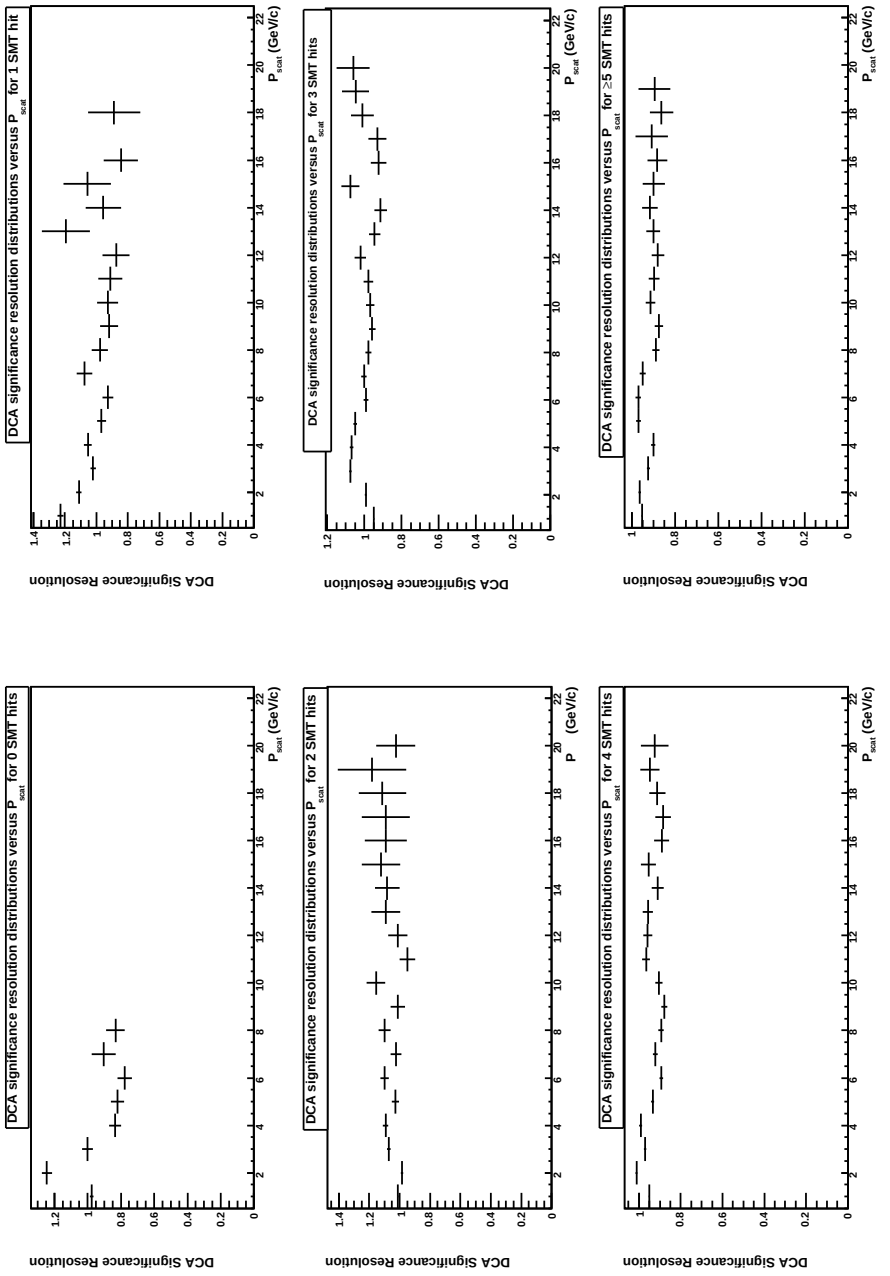

Figure 4.6: DCA significance resolution versus p_{scat} plots for the QCD Monte Carlo and the derived DCA error parameterization. In order from top left to bottom right on the rotated figures are 0, 1, 2, 3, 4 and ≥ 5 SMT hits. Values close to 1 represent cases where the error parameterization has worked. The 0 and 1 SMT hit plots have values that lie far from 1, however this is acceptable since tracks must have at least 2 SMT hits in order to be considered to make a vertex. Missing entries on each plot are indicative of a failed Gaussian fit to that DCA significance distribution, usually due to a lack of statistics.

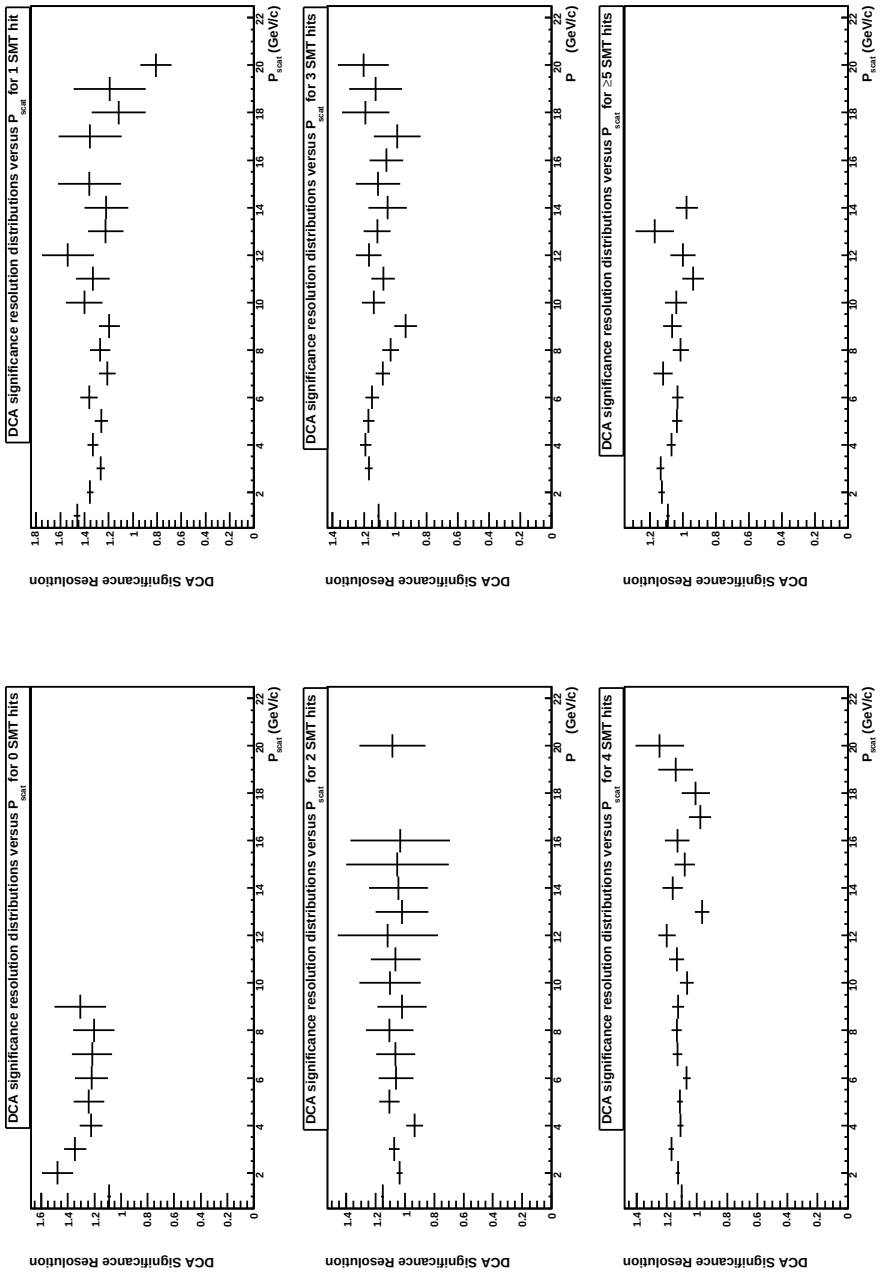

Figure 4.7: DCA significance resolution versus p_{scat} plots for the data sample and the derived DCA error parameterization. In order from top left to bottom right on the rotated figures are 0, 1, 2, 3, 4 and ≥ 5 SMT hits. Values close to 1 represent cases where the error parameterization has worked. The 0 and 1 SMT hit plots have values that lie far from 1, however this is acceptable since tracks must have at least 2 SMT hits in order to be considered to make a vertex. Missing entries on each plot are indicative of a failed Gaussian fit to that DCA significance distribution, usually due to a lack of statistics.

Since the vertexer is needed to recalculate the track parameters with respect to the found vertex, as opposed to the origin as assumed by the tracking software, it is simple to then use the vertexing results in order to obtain another handle on the performance of the new errors.

Whilst the DCA significance plots in figures 4.6 and 4.7 are important to see whether or not the new errors work, looking at the vertexing results allows for estimations to be made as to results obtained by using the trigger online. Of particular interest here are the vertex resolutions in both the x and y directions and the number of the tracks assigned to a given vertex.

Figure 4.8 shows the number of tracks associated to a given vertex for both the data sample and the QCD Monte Carlo sample. Since at least two tracks are required to make a vertex, any events which fail to produce a vertex will be assigned as having zero associated tracks. Those events with more tracks associated to a vertex will generally correspond to a better quality vertex. In the data sample it can be estimated that about 55% of the events have zero associated tracks and hence have failed to find a vertex; this is comparable to the results obtained from the certification of the Run IIa tracking software. All events that fail to find a vertex will simply return the beam spot as measured by the `vertex_examine` program in data and return the origin in Monte Carlo.

The x and y vertex distributions for data can be seen in figure 4.9, and the resolutions in Monte Carlo can be seen in figure 4.10. By fitting the distributions with a Gaussian function a measurement of the vertex resolution can be made. This works out to be 28.6 $\pm$ 0.1 μm for the x vertex and 26.0 $\pm$ 0.1 μm for the y vertex in data, and 20.9 $\pm$ 0.1 μm for the x and also 20.9 $\pm$ 0.1 μm for the y in Monte Carlo. It should be noted in these plots that those events which fail to find a vertex, and hence have zero associated tracks to the vertex, have been excluded. Including those tracks would produce an excess in the bin nearest to the beam spot location. The Monte Carlo results obtained here can be compared to those shown in figure 4.1, and it can be seen that the new errors are working as desired due an improved vertex resolution.

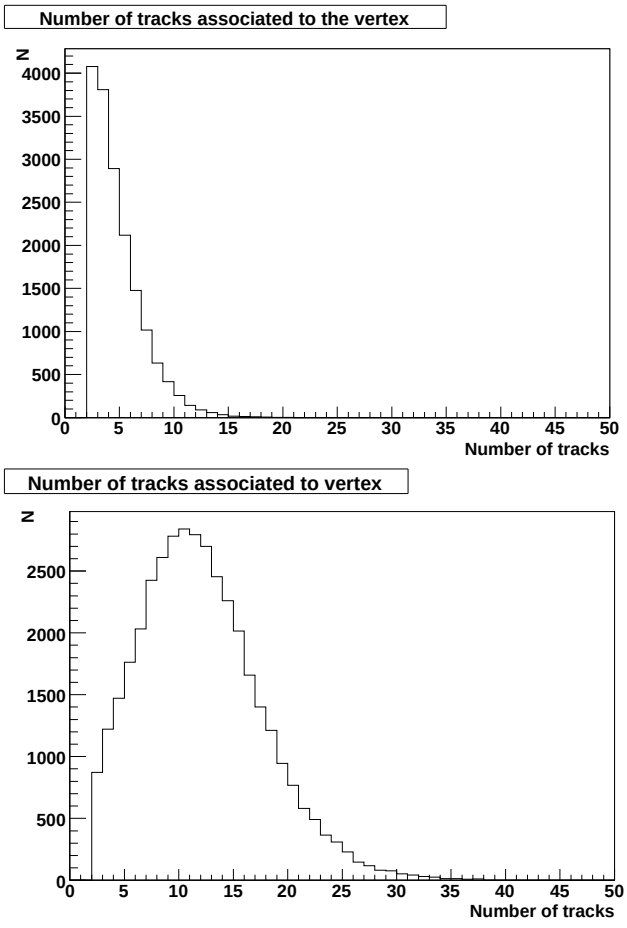

Figure 4.8: The number of tracks associated to the found Level 3 vertex using the new DCA error parameterization on both the chosen data sample (top) and QCD Monte Carlo (bottom). The mean number of associated tracks in the data sample is 4.32 ± 0.02 and 11.55 ± 0.03 in the Monte Carlo.

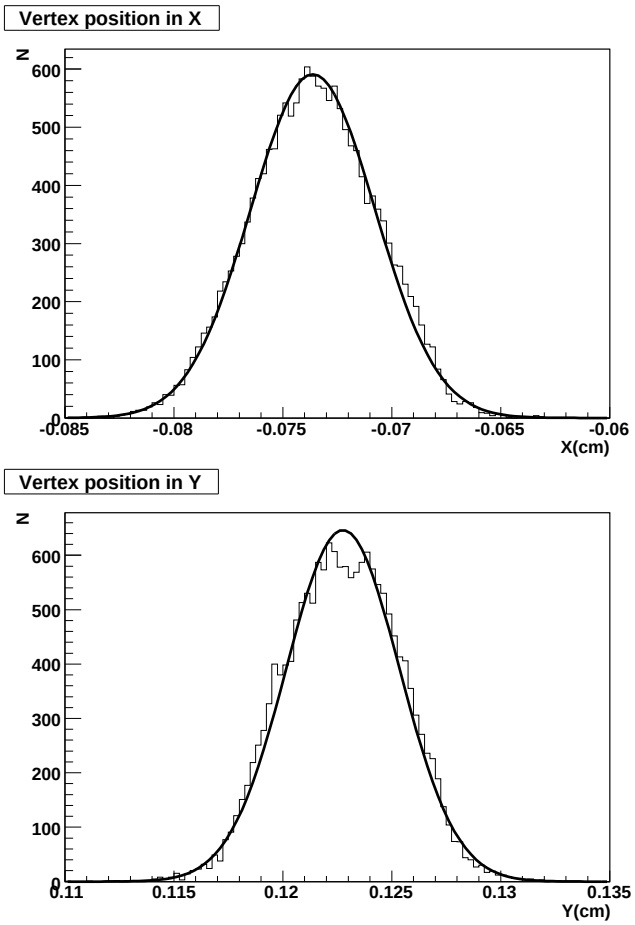

Figure 4.9: x (top) and y (bottom) vertex resolutions obtained in the data sample using the new DCA errors. The x vertex resolution is found to be 28.6 ± 0.1 μm, whilst the y resolution is found to be 26.0 ± 0.1 μm.

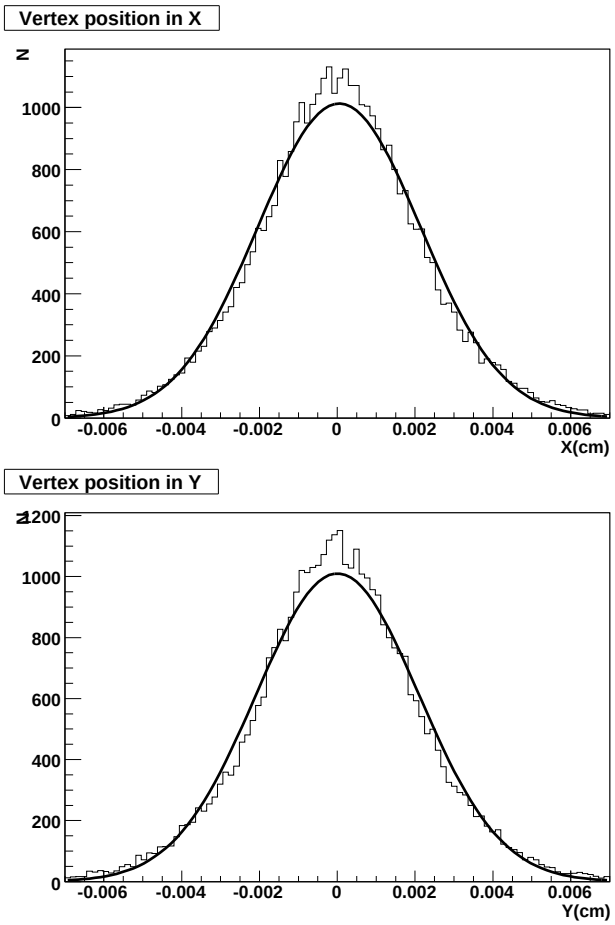

Figure 4.10: x (top) and y (bottom) vertex resolutions obtained in the QCD Monte Carlo using the new DCA errors. The x vertex resolution is found to be 20.9 ± 0.1 μm, whilst the y resolution is found to be 20.9 ± 0.1 μm.

4.7 Conclusions

This chapter has introduced the new Run IIb tracking software, `L3TCFTTrack`, which is designed to deal with the increasing luminosity, and hence processing demands of Run IIb, and the need to tune appropriate errors for this new tracker and the process used and results obtained.

In addition, this chapter described the methods used to certify and verify the obtained errors by investigating both the DCA and the DCA significance as a function of both p_{scat} and the number of SMT hits, the former to derive the DCA error parameterization (figure 4.4) and the latter to verify the obtained results, as well as looking at the results obtained from the $x - y$ vertexer. DCA significance distributions lying uniformly close to 1 show that good errors have been obtained (figures 4.6 and 4.7), whilst the number of associated tracks and measured vertex resolutions have been shown to have improved in the Monte Carlo once the new errors are implemented (11.55 ± 0.03 tracks versus 10.9 ± 0.03 tracks with the new and old errors respectively, and improvements of 0.5 to 0.8 μm in the vertex resolutions between the old and new errors). Whilst the vertex results are similar to those seen in Run IIa, the reduced processing time and better efficiency obtained using the Run IIb tracking algorithms makes this the more desirable software.

The errors described here are for using a hardware set up that corresponds to that used in Run IIa, that is excluding the new silicon hardware added in Run IIb, Layer 0. The reason that the initial Level 3 release used online in Run IIb excluded Layer 0 was to ensure that the new tracking algorithms were working as expected online when run in concert with all the other triggering upgrades. However, it would not be long until a new Level 3 release was placed online that included code to deal with Layer 0 readout and clustering and a new set of associated DCA errors to go with the upgraded SMT unpacking software. The SMT unpacker upgrades and the new DCA errors are described in the following chapter.

Chapter 5

The Layer 0 detector and Level 3

5.1 Preface

This chapter concerns the integration of the new Layer 0 sub-detector into the existing Level 3 SMT unpacker, `L3TSMTUnpack` [55], and its integration into the Run IIb tracking software, `L3TCFTTrack` [68]. Details of both the existing SMT unpacking packages, unpacking and clustering, are covered, as well as the modifications made to include Layer 0 into those routines. Since there was a change to the silicon input to the tracking software, a new DCA error parameterization was also required, details of which are also covered in this chapter.

The Layer 0 changes were then tested by an investigation into the produced Layer 0 clusters themselves and into the tracks produced using the modified SMT unpacker. The DCA errors were parameterized in terms of the number of SMT hits and p_{scat} according to the method described in the previous chapter. The new errors were then compared to the previous ones, produced without Layer 0, through comparison of the DCA resolutions in the individual bins and through comparison of the $x - y$ vertexing results, once the DCA significance versus p_{scat} distributions had been verified.

5.2 Layer 0 and Level 3

The DØ Run IIb upgrade brought many changes to both the software and hardware used by the experiment. One of the major hardware upgrades was the introduction of a new layer of silicon to the existing SMT detector. This extra layer was designed to help improve existing momentum and impact parameter (DCA) track resolutions and also to supplement the radiation damaged innermost layer of the existing SMT detector.

As previously mentioned, the upgrade was not limited to the silicon hardware. Numerous triggering upgrades were also undertaken, most noticeably at Level 1 and Level 3. The previous chapter covered one of the main upgrades undertaken to improve the Level 3 trigger, the new Run IIb tracking software, `L3TCFTTrack`. One of the main design goals of the new software was to allow for easy integration of Layer 0 into the SMT tracking algorithms. However, for the Run IIb SMT tracking algorithms to know about and use the new Layer 0 information, changes were made to the read out and clustering algorithms in the SMT unpacker, `L3TSMTUnpack`.

5.3 Modification of the Level 3 SMT unpacker

The SMT unpacker, `L3TSMTUnpack`, is responsible for the silicon read out and clustering within Level 3. These two components are run consecutively for each chip that is read out, with clustering, in effect, being performed 'on the fly'. Both of these required modifications made to make them compatible with Layer 0 readout and to ensure that the data from the new sub-detector are formed into clusters that can be read and used by the Run IIb tracking algorithms, whilst preserving full backwards compatibility with the existing Run IIa detector. This was done through the use of switches to turn the Layer 0 modifications on or off as desired. The changes made to each of the algorithms are discussed in detail below.

5.3.1 SMT chip readout

The Layer 0 sub-detector utilizes SVX-4 chips in order to facilitate readout of the silicon strips. These are an upgraded version of the SVX-2 chips used in the rest of the silicon detector and can allow for more advanced triggering decisions to be made compared to the older chips through the use of more advanced event buffering techniques. However, for simplicity in readout, and to enable use of the existing front end crates, these newer chips are run in SVX-2 mode. Each of the SVX chips handles 128 channels of silicon strip information and through newer manufacturing techniques are more radiation tolerant than the existing SVX-2 chips.

Similarly to the existing silicon read out, the SVX chips are placed into an High Density Interconnect (HDI) module from which the actual readout is taken. Unlike the rest of the system, in Layer 0 only 2 SVX chips are placed in each HDI. The single sided nature of the Layer 0 strips reduces the number of channels that need to be read out on each strip and thus reduces the number of SVX chips needed to interface with said channels. The data from the HDIs are passed through adaptor and interface boards before being passed to the sequencer boards. The sequencer then passes the data by fibre optic link to the VRB (VME Readout Buffer) boards in the front end crates. Layer 0 has 4 HDIs linked to each VRB board. Each front end crate also contains a board to pass data to Level 3 and a board to control the operation of the crate. Layer 0 was designed to use the VRB boards previously used by the two outer H-disks in Run IIa, and so the design of the Layer 0 sequencer cards allows for these to interface correctly with the older VRB hardware. This results in no interface changes to the front end crates being required in either the online or offline software.

When the data packet is passed to the next stage in the read out chain, a new header is added to the existing data to help in the next stage of read out. These headers are unique to each HDI and VRB and detail the path followed so far by the data stored within. The VRB contains the information for all of the component HDIs connected to it, and its header is simple and contains information about where it is located in the front end crates, the size of the data within (in number of bytes)

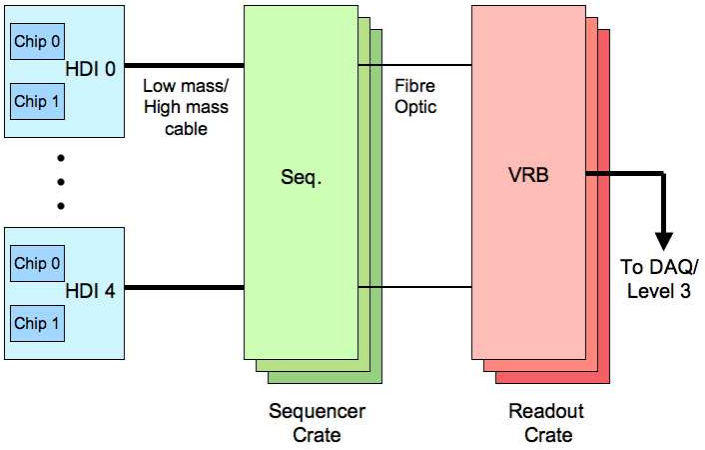

Figure 5.1: Illustration of the SMT readout system for the Layer 0 detector. The 4 Layer 0 HDIs only have 2 SVX chips connected to each. The sequencer and VRB crates are pre-existing from Run IIa and were used to readout the outer H-disks.

each of the HDIs, as well as a total byte count for that VRB. The HDI header is added when the sequencer reads out the relevant HDI and contains information about which sequencer read out the HDI and the status and ID of the read out HDI. The data format from the HDI for the Layer 0 sub-detector is:

```
HDI header

     Chip 0 header

         Channel 0 data

         Channel 1 data

         ...

     Chip 1 header

         Channel 0 data

         Channel 1 data

         ...

HDI end of record
```

As previously stated, there can be up to 128 channels per chip, but the chip is capable of varying the number of channels that are actually read out if necessary. The data format can be extended to as many chips as needed for the other layers and disks. The SVX chip header contains information about the chip ID, whilst the SVX channel data contains the channel ID and ADC count from the silicon strips on the ladders.

Level 3 readout of the SMT consists of a coding interface to the data stored in the front end crate download (stored in the raw data chunk, `RawDataChunk`) that utilizes SMT libraries common to both the Level 3 and d0reco versions of the SMT unpacker. These libraries are used to translate the HDI headers into strip information, including detector type (barrel or Layer 0), barrel number, ladder number and side. They are also used to apply calibrated pedestal settings to the individual channels in the d0reco unpacker, however, due to time constraints a simpler parameterization is applied to each HDI at Level 3. This parameterization allows for pedestals for each channel to be estimated for each HDI.

Layer 0 modifications

The Layer 0 modifications involved the removal of the readout code for the outer H-disks, and the modification of the barrel read out code to include the new sub-detector. Level 3 tracking does not use information coming from the F-disks or the H-disks, so the needed changes to the H-disk code do not have any effect on Level 3 tracking performance. Since the new silicon layer is treated by the libraries as a separate detector to the rest of the barrel system, the Level 3 read out code initially treats Layer 0 as a separate sub-detector, before then integrating it into the overall barrel detector information. Amalgamating the Layer 0 detector in with the other 8 SMT barrels allows for the clustering algorithms to effectively be transparent to the change from Layer 0 to layers 1 to 8. The only differences observed by the clustering algorithm are an increased number of barrels - 8 barrels in Layer 0 compared to 6 in the other layers - and full 2π coverage around the beam pipe. However, modifications to the clustering algorithms and the silicon geometry used allow for this to proceed smoothly, and these changes are detailed in section 5.3.2 below.

5.3.2 The SMT clustering algorithm

Once a given chip has been read out by the systems described above, the processed data are passed onto the clustering algorithm in order to produce SMT clusters which the tracker can use to improve the quality of the track hypotheses it finds from the CFT clusters. The clustering algorithm works by grouping adjacent hit strips into 'two dimensional' clusters, and using the axial and stereo layers (the 90° ladders in particular) to directly obtain positions in $r-\phi$ and z respectively. Though the capability to combine the 2° ladders with the two dimensional clusters exists to produce three dimensional clusters, it is not currently used online.

The SMT detector describes strip locations in its local coordinate system, thus in order to obtain locations within the overall DØ detector that can be used by the tracker, a conversion system is required before the final clusters can be formed, and this is described below.

The SMT geometry and coordinate system

Since Level 3 only uses the barrel information, only the coordinate transformations for the barrel ladders will be described here. As previously mentioned, each ladder has its own local coordinate system [72]. The local z axis is orientated towards the SVX chips, the local y axis is directed from the p side of the detector to the n side, whilst the local x axis is orientated to form a right handed coordinate system. This is illustrated in figure 5.2. The origin of the local coordinates is positioned at the centre of a given ladder. A one dimensional position, known as the cluster centroid, is measured along a line perpendicular to the orientation of the hit strip, or strips for the double sided ladders, keeping the origin at the centre of the ladder still.

For double sided ladders with 90° stereo ladders this equates to:

$$x_L = u_1 \qquad z_L = -u_2 \tag{5.1}$$

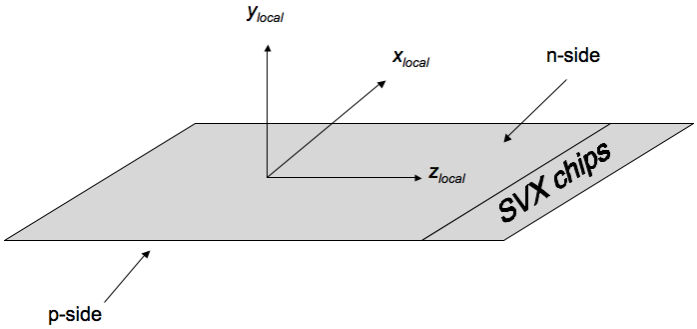

Figure 5.2: The local coordinate system used for the silicon ladders. The z_{local} points towards the SVX chips at one end, the y_{local} points from the p-side to the n-side and the x_{local} is orientated to form a right handed coordinate system.

where u_1 and u_2 are the cluster centroids of the axial and stereo sides respectively, and x_L and z_L are the relevant positions in the local coordinate system.

Once the cluster centroids have been calculated it is necessary to convert the local coordinates into the global coordinate system common to all sub-detectors in DØ. Due to timing constraints at Level 3, an approximation to the full offline geometry is made by making the assumption that the ladders in the barrels can be treated as though they are flat planes. This allows for the following linear transformation to be made:

$$\begin{pmatrix} x_G \\ y_G \\ z_G \end{pmatrix} = \mathbf{r}_0 + x_L\mathbf{r}_1 + y_L\mathbf{r}_2 \tag{5.2}$$

where $\mathbf{r}_0$ is the vector from the global origin to the centre of the ladder, $\mathbf{r}_1$ is the global coordinate vector corresponding to the location (1,0,0) in the local system and $\mathbf{r}_2$ is the global coordinate vector corresponding to the location (0,0,1) in the local system, x_G, y_G and z_G are the positions in the global coordinate system [73].

Two dimensional clustering

Though many improvements were made to the clustering algorithms at the end of Run IIa, (see section 3.6 for details), the core clustering principle remains the same. The algorithm works by taking each new strip, with an energy deposit higher than a threshold value, and then checking to see whether or not the energy deposit lies adjacent to an existing cluster on the same detector element. If so then the strip belongs to the current cluster. If not, or if it is the first unpacked strip for a given event, then it is treated as the start of a new cluster.

The position of a given cluster is decided by taking the weighted average of the pulse heights for all the strips to be included in said cluster:

$$\overline{n} = \frac{\sum n_i w_i}{\sum w_i} \tag{5.3}$$

where n_i is the strip number of the ith strip and w_i is the energy in the strip. From this a centroid position, u, can be calculated:

$$u = u_1 + (\overline{n} - 1)p \tag{5.4}$$

where u_1 is the centroid of the first strip and p is the pitch of strips as given by the SMT geometry files. Equation 5.1 can then be used to convert the centroids into local ladder coordinates, and then this can be transformed into global coordinates by using equation 5.2. The final clusters are then stored and can be passed onto the tracker for use there.

Layer 0 modifications

Since Layer 0 contains only single sided ladders, only axial information is obtained from read out of this detector, that is only $r - \phi$ information. As such equation 5.1 condenses down to:

$$x_L = u \tag{5.5}$$

where u is the cluster centroid for the relevant strip, and can then be transformed into global coordinates as shown above. As previously stated, each ladder within the existing barrels has its own local coordinate system, and this is no exception in Layer 0.

Since the read out routines convert Layer 0 from a separate sub-detector into another barrel layer, the barrel clustering algorithms are the ones that have been adjusted to account for the added inner layer, whilst the H-disk clustering algorithms were modified to account for the removed outer disks. This involved ensuring that the clustering algorithm creates clusters correctly in all 8 barrels, and each of the 6 ladders on each barrel, and that relevant adjacent strips are added to existing clusters too. However, the differing numbers of barrels and ladders makes no difference to the clustering as the clusters do not spread across different layers of the detector.

As stated above, the improvements made to the clustering routines in p17, as detailed in 3.6, are also used in conjunction with Layer 0. This means that said improvements, like cluster merging and splitting, are routinely used to help improve the quality of the Layer 0 clusters coming from the Level 3 unpacker.

5.3.3 SMT unpacker results

The result of the changes made to the SMT unpacker are observed in two ways, looking at the clusters themselves and looking at the tracks made using those clusters. Investigations into the clusters will show whether or not the unpacker changes are working as intended, and are detailed here.

At the start of Run IIb Level 3 was running without Layer 0 unpacking. This was to ensure that the tracker was performing as designed under known conditions. However, the data recorded to tape still includes Layer 0 information, and so this provides ideal data that can be used to verify the Layer 0 changes to the unpacker.

In particular, over 400,000 events from run 230114, which had an initial luminosity of 1.55x10^{32} cm^{-2}s^{-1}, were chosen to be the test data sample. The number of Layer 0 clusters found by the Level 3 SMT unpacker for this sample is shown in figure 5.3.

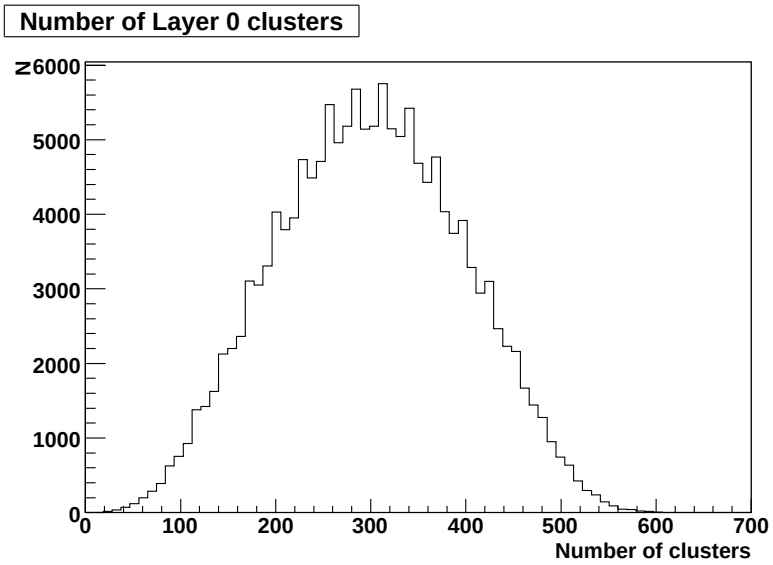

Figure 5.3: The number of clusters found by the Level 3 SMT unpacker in Layer 0. The mean number of clusters per event is 298.9 ± 0.2.

The Layer 0 detector itself provides full 360° coverage around the beam pipe, so one way to check that the unpacker is working as intended is to check whether or not found clusters lie around the full detector circumference. This is represented by the global ϕ distribution of the Layer 0 clusters, and is shown in figure 5.4 for the data sample described above. As can be seen here, the distribution runs from 0 to 2π with few breaks in between. As a comparison to the rest of the SMT, figure 5.5 shows the clusters found for all 9 layers of the barrels.

Timing is a major concern at Level 3, and so the Layer 0 changes made to the SMT unpacker should not increase the total unpacking time. In practice though there is a slight increase in processing time simply due to the increased number of layers to unpack and clusters to form with the addition of Layer 0. However, this increase is very slight and the time taken by the tool is still only a small fraction of the total processing time. This can be seen in figure 5.6 which compares the SMT unpacker timings with and without Layer 0. As is seen here, the increase in time equates to just under 1 ms per event on average.

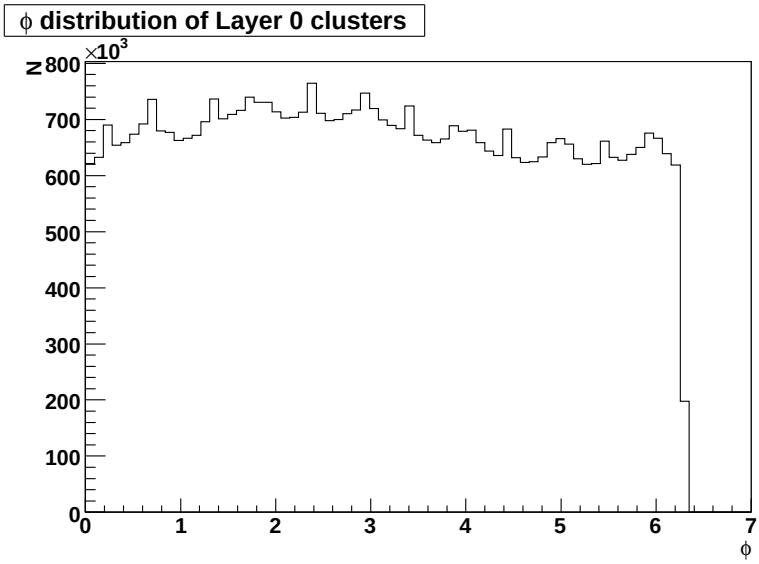

Figure 5.4: The ϕ distribution of Layer 0 clusters.

5.3.4 Layer 0 and the Run IIb tracking algorithms

Another way to investigate the performance of the new Layer 0 modifications is to observe the results of the Run IIb tracking software, `L3CFTTrack`, when used in conjunction with Layer 0. For all the studies shown here 3500 events taken using a combination of all available triggers from a normal data taking run, run 230114 (initial luminosity of 1.55x10^{32} cm^{-2}s^{-1}) were chosen as a data sample. Figure 5.7 shows the number of axial SMT hits assigned to the tracks. This figure reveals a higher mean number of hits per track when Layer 0 is active than when it is disabled (2.26 ± 0.01 with Layer 0 versus 1.85 ± 0.01 without). This shows that the tracking software is making good use of the extra layer of potential hits.

The certification process described in section 3.5.1 is used to compare the Level 3 tracks to those found by d0reco, and thus produce tracking efficiencies and purities with which to gauge tracking performance with and without Layer 0 readout, as well as checking that the processing time does not increase too significantly with the addition of the extra silicon layer. These results can be seen in table 5.1.

As can be seen in table 5.1, the tracking efficiency and purity do not change with the addition of Layer 0. This is to be expected as the silicon clusters are only added

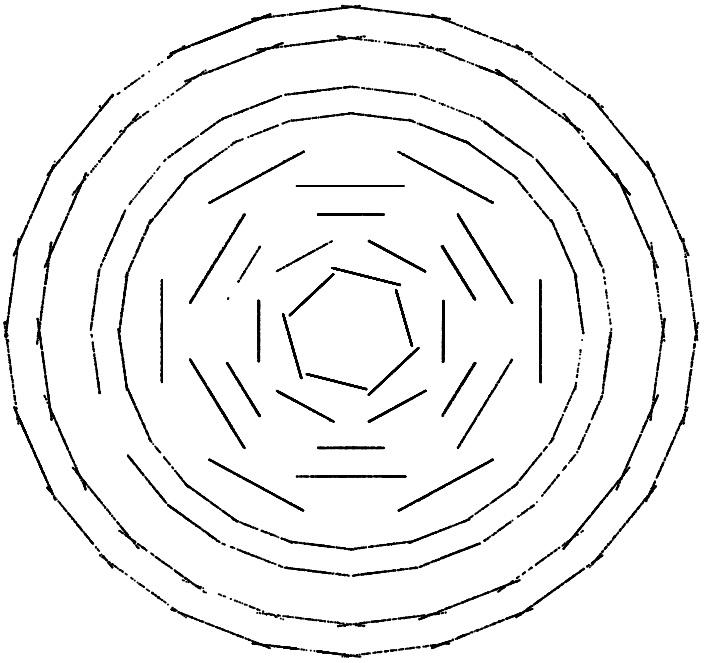

Figure 5.5: Cluster read out for the 9 layers of the SMT. The clusters shown are spread out over 50 events, not all clusters will be found in one particular event. Regions where gaps are observed are either due to fewer ladders in that layer, as shown in the inner layers, or to problems in the SVX chip readout, as shown in the outer layers. Layer 0 is the innermost silicon layer shown here.

	Without Layer 0	With Layer 0
Efficiency	0.651 ± 0.001	0.651 ± 0.001
Purity	0.263 ± 0.001	0.264 ± 0.001
Mean Tracking Time (ms)	327.1 ± 5.2	329.9 ± 5.3

Table 5.1: Comparison of tracking performance with and without read out of Layer 0. These results were made using 3500 events of average luminosity data.

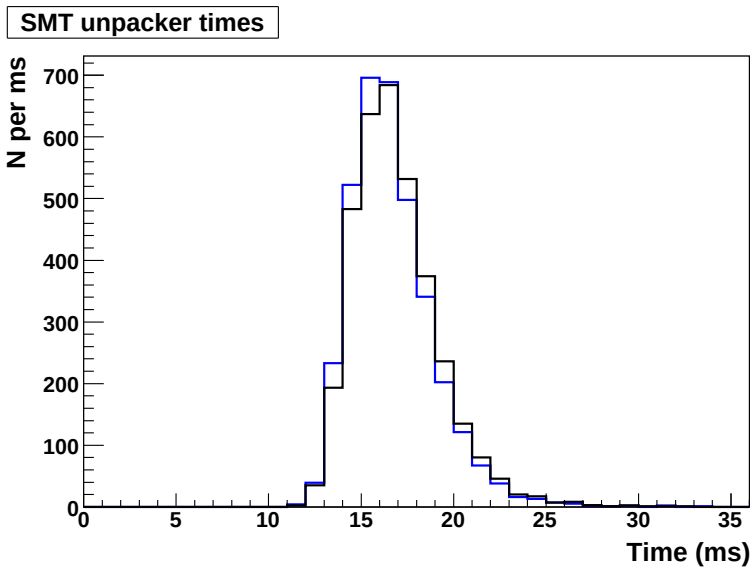

Figure 5.6: Level 3 SMT unpacker times for 3500 events of average luminosity data using Layer 0 (blue) and not using Layer 0 (black). There is a slight increase in the unpack processing time with the inclusion of Layer 0, with the mean unpacking time changing from 14.78 ± 0.03 ms without Layer 0 to 16.51 ± 0.04 ms with Layer 0.

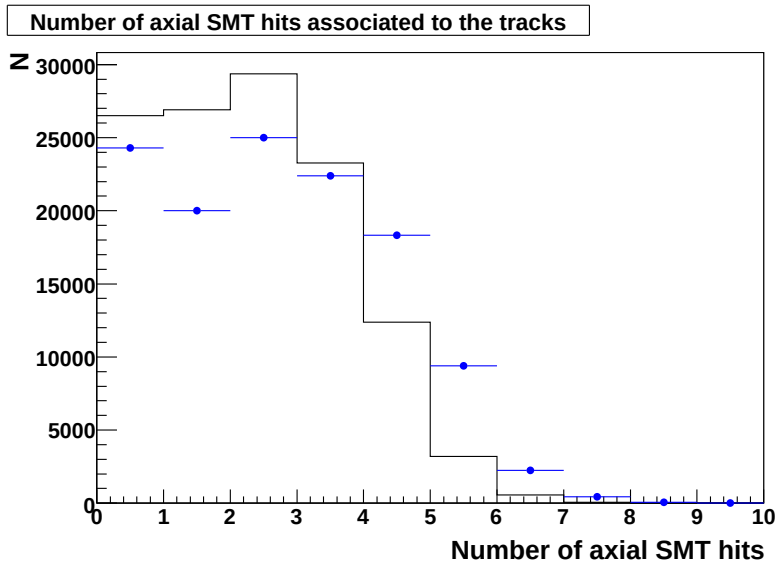

Figure 5.7: Comparison of the number of axial SMT hits from Level 3 tracks matched to d0reco tracks between when Layer 0 is included (blue) and when it is excluded (black). The mean number of hits per track increases from 1.85 ± 0.01 to 2.26 ± 0.01 with the inclusion of Layer 0. The dip in the number of tracks with 1 SMT hit when Layer 0 unpacking is included is due to the propensity of the Run IIb Level 3 tracking software to add a Layer 0 hit to tracks with only one SMT hit in the rest of the detector.

on to a track that was originally found within the CFT, and hence should not have any effect on tracking performance. However, it is important to check this as it helps verify the integration of the new silicon into the existing tracking algorithms. The mean tracking time is found to be the same within errors with and without Layer 0 read out. It should be noted, however, that the efficiency for track finding for tracks with ≥ 2 SMT hits increases when Layer 0 readout is included. A sample event display for the Level 3 tracking algorithms combined with the Layer 0 SMT modifications for one particular event from run 230114 is shown in figure 5.8.

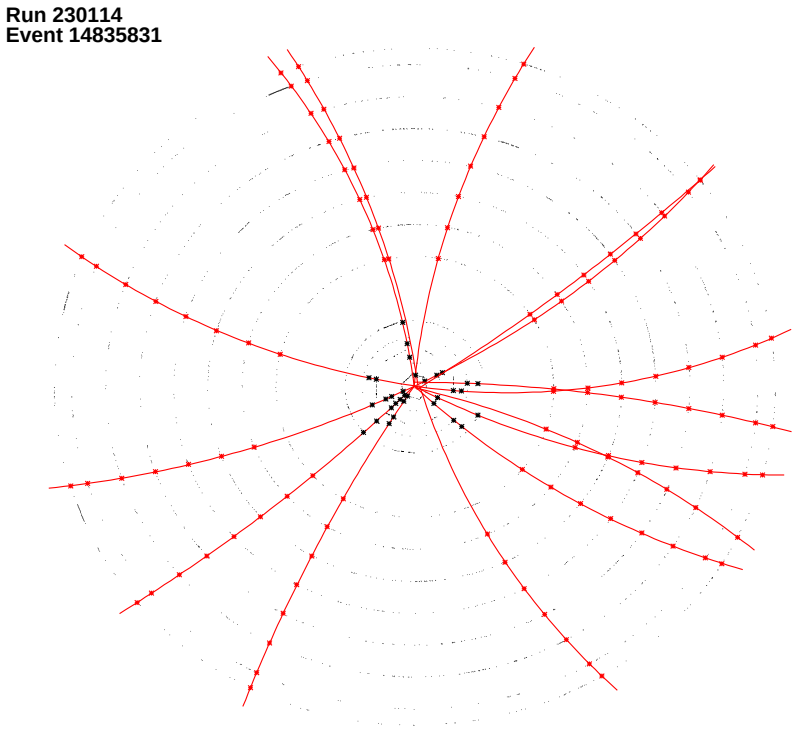

Figure 5.8: Sample event from run 230114 showing the Level 3 tracks, hits and found CFT and SMT clusters. Layer 0 is the innermost layer, and the clusters found there are being used in many tracks.

One of the main reasons for the addition of the extra silicon layer was to help improve the track DCA resolution. By adding a layer of silicon closer to the collision point, one can dramatically improve the errors on the measurement of tracks, and low momentum tracks in particular. Figure 5.9 shows a comparison of the overall DCA resolution for good matched tracks (that is those which have been matched to offline

tracks) being returned by the Level 3 tracking software with and without Layer 0. Single Gaussian fits to the resolution distributions reveal the overall resolutions, and from this it is seen that the overall DCA resolution improves by about 50%. The improvement to the DCA resolution is investigated in more detail in section 5.4 below.

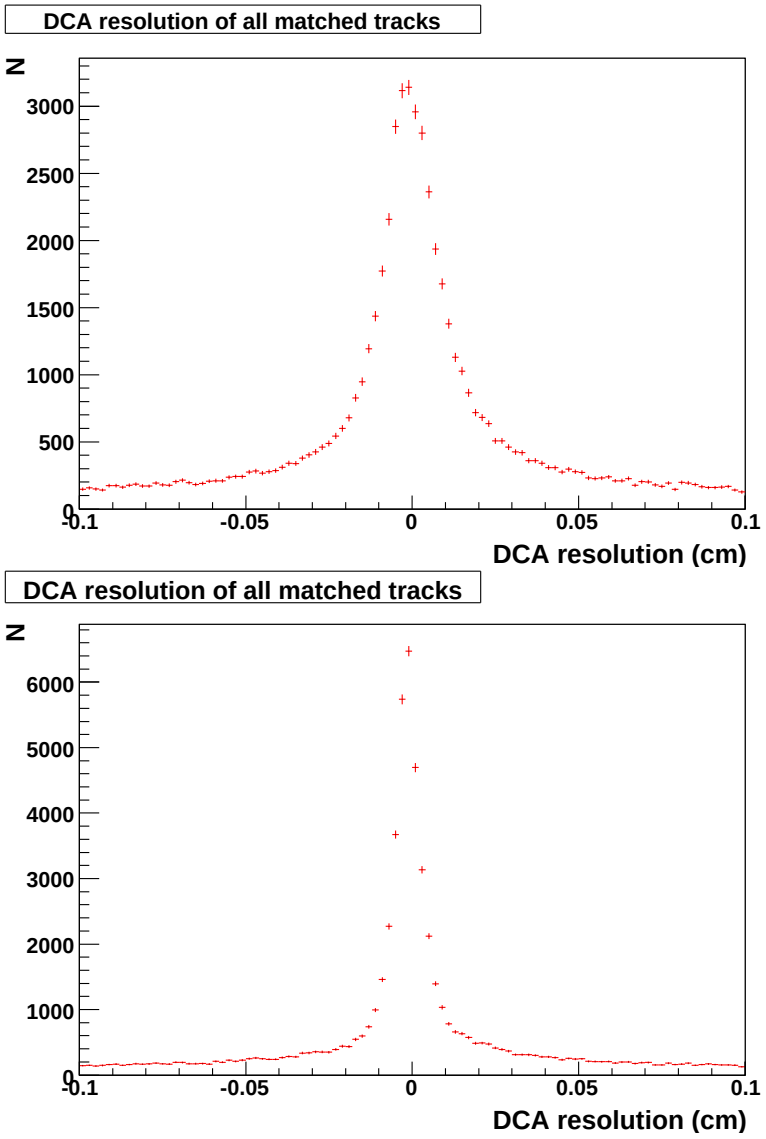

Figure 5.9: Overall DCA distributions for all Level 3 tracks which successfully match to d0reco tracks without (top) and with Layer 0 (bottom). The measured DCA resolution, using a Gaussian fit on both, without Layer 0 is 114 ± 7 μm and with Layer 0 it is 70 ± 4 μm.

5.4 Track DCA errors and Layer 0

The addition of Layer 0 to the Level 3 SMT unpacker enables the use of an extra possible silicon hit. As such, it is necessary to redo the DCA error parameterization process detailed in the preceding chapter. The same parameterization method is used, and this is then followed by a similar certification process involving investigations into DCA significance versus p_{scat} distributions and looking at the $x - y$ vertexing results to ascertain the benefit Layer 0 provides to primary vertex location.

5.4.1 Monte Carlo and data samples

The QCD Monte Carlo used previously, as detailed in 4.4.1, did not include Layer 0 in its production sequence, namely at the detector simulation and digitization stages. Thus, a new QCD Monte Carlo sample was created using the same Pythia output as before, with the beamspot fixed to (0,0), but then running the Pythia output through new versions of the detector simulation and digitization software which include Layer 0. The results are comparable samples, based on identical Pythia events, that can be used to both derive a new DCA error parameterization including Layer 0 and to then test and compare the new errors to the older errors (which exclude Layer 0).

For the $x - y$ vertex testing and the DCA significance resolution versus p_{scat} distributions a data sample is also required. The chosen data sample must be able to be used with and without Layer 0 so a comparison can be obtained. Thus 400,000 events from run 230114 (initial luminosity $1.55\text{x}10^{32}$ $\text{cm}^{-2}\text{s}^{-1}$) were chosen to fulfill these requirements and to produce certification plots.

5.4.2 The new parameterization

To derive new DCA errors, the individual track DCAs are binned in terms of both p_{scat} and the number of SMT hits. As before, a range of 0.5 to 20.5 GeV/c is used for p_{scat} and a range of 0 to ≥ 5 hits is used for the number of SMT hits. The bins

are all individually fit with the same function as before, a double Gaussian, from which the weighted mean is extracted and taken as the DCA resolution for that particular bin. Figure 5.10 shows a comparison of a single p_{scat} and SMT bin with and without Layer 0 included. In this particular bin, 2.5 to 3.5 GeV/c and 3 SMT hits, an improvement in the DCA resolution from 24.9 $\pm$ 2.0 μm without Layer 0 to 23.2 $\pm$ 3.5 μm with Layer 0 is obtained.

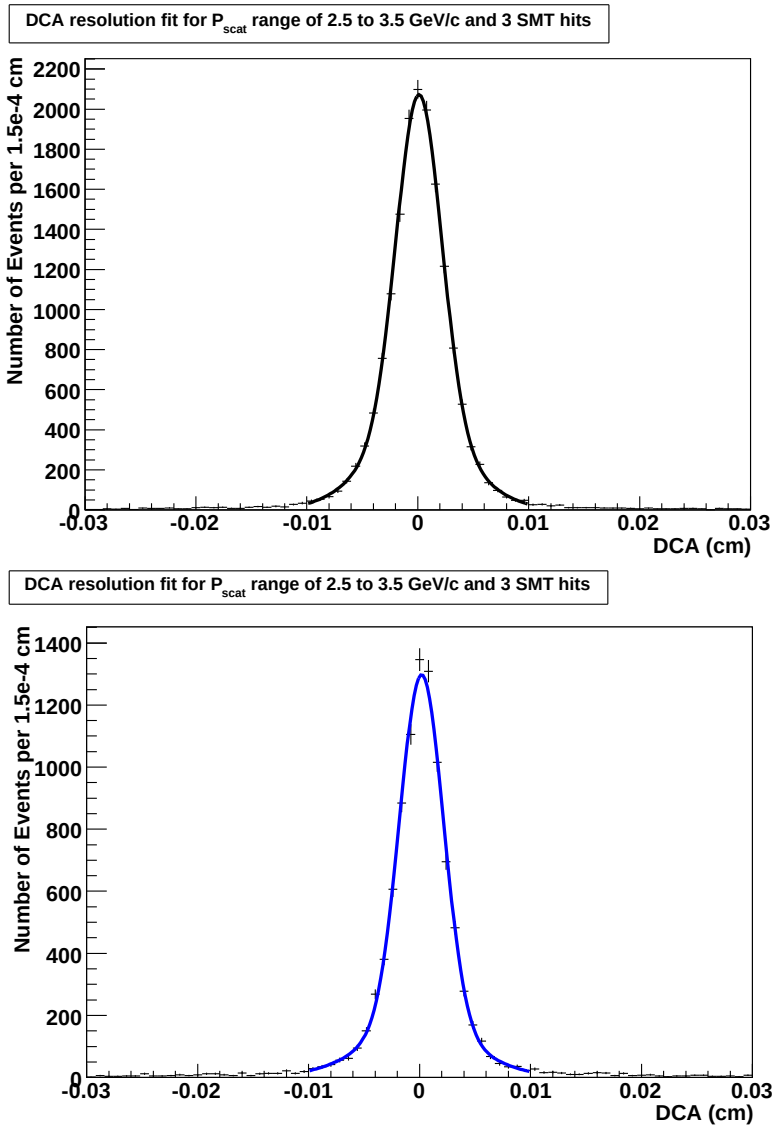

Figure 5.10: Sample DCA resolution fit for a p_{scat} range of 2.5 to 3.5 GeV/c and 3 SMT hits without (top, black) and with (bottom, blue) Layer 0. The measured DCA resolution with Layer 0 here is 23.2 $\pm$ 3.5 μm and without Layer 0 it is 24.9 $\pm$ 2.0 μm.

Once all the p_{scat} and SMT bins have been filled and fitted, the resultant DCA

resolutions are taken and plotted against p_{scat} for each of the six SMT bins. The final distributions are then fit according to the function shown in equation 4.5 and the parameters c_0 and c_1 extracted from the fit. The DCA resolution versus p_{scat} distributions and fits when including Layer 0 are shown in figure 5.11, whilst the resultant fit parameters are shown in table 5.2.

The distributions shown in figure 5.11 and values shown in table 5.2 are directly comparable to those shown in figure 4.4 and table 4.2, which were derived without the use of the Layer 0 sub-detector. Due to a lack of statistics in the 0 SMT hit bin, the previous distribution and values for c_0 and c_1 are used in the new error parameterization. Though this is not ideal, the lack of SMT hits means that the errors should be near identical even with the inclusion of Layer 0. In addition to this, tracks with less than 2 SMT hits are not used for the vertexing tools, and hence for the latter b-tagging and lifetime tools, so the lack of ideal errors will not impact on these tools.

Number of SMT hits	c_0	c_1
0	0.136 ± 0.008	0.448 ± 0.02
1	0.0082 ± 0.0007	0.071 ± 0.001
2	0.0022 ± 0.0001	0.0054 ± 0.0003
3	0.00177 ± 0.00007	0.0038 ± 0.0002
4	0.00134 ± 0.00004	0.0035 ± 0.0001
≥ 5	0.00112 ± 0.00003	0.0034 ± 0.00008

Table 5.2: The values of c_0 and c_1 derived from the fits performed to the DCA resolution versus p_{scat} distributions shown in figure 5.11. The results shown here include SMT clusters coming from Layer 0.

5.4.3 DCA significance versus p_{scat}

Once the new fit values derived from the DCA error parameterization process are entered into the Run IIb tracking software, the new errors can be tested and verified as before. The testing first takes the form of investigations into the DCA significance distributions as a function of p_{scat} and the number of SMT hits for the new errors for both the QCD Monte Carlo and the data samples.

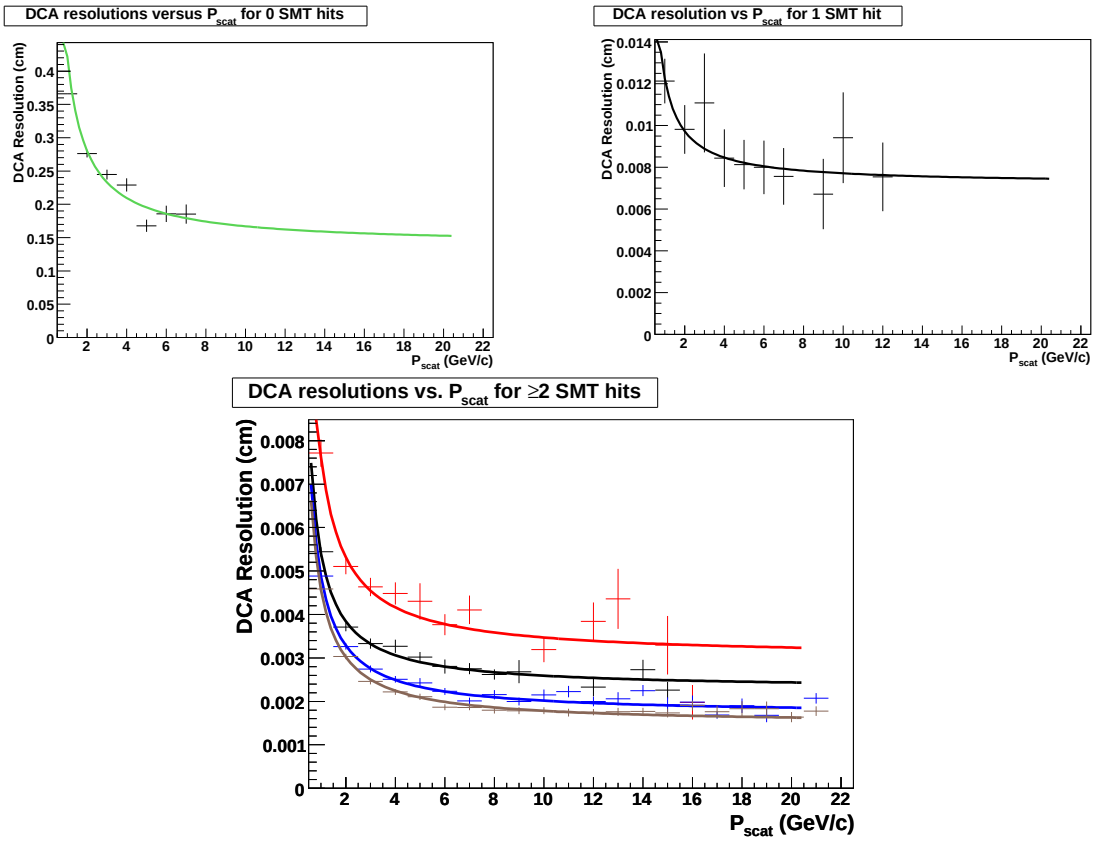

Figure 5.11: DCA resolution versus p_{scat} graphs for each of the six SMT hit bins including Layer 0 information. Each of the distributions are fit according to the function shown in equation 4.5. The first distribution is for 0 SMT hits, the second for 1 SMT hit. The plot showing many distributions contains, from top to bottom, 2 (red), 3 (black), 4 (blue) and ≥5 (brown) SMT hits. The locations where the distributions lack entries for a particular range of p_{scat} values represent where the Gaussian fit to that distribution has failed.

By binning the track DCA significance, once the DCA has been recalculated with respect to either the real or smeared beamspot (for data and Monte Carlo respectively) as before, by both p_{scat} and the number of SMT hits, the individual bins can then be fit by a double Gaussian function in order to extract a weighted mean DCA significance resolution for each bin. The DCA significance resolution should ideally be a flat distribution which lies close to a value of 1. This represents a good parameterization of the DCA errors.

Plotting the individual DCA significance resolutions for every p_{scat} and SMT bin allows for the overall DCA significance resolution distribution to be observed. The distributions for the 6 SMT bins for the QCD Monte Carlo can be seen in figure 5.12, whilst the distributions for the data sample can be seen in figure 5.13. The distributions for the majority of the SMT bins lies uniformly around 1, the exceptions being the distributions with 0 SMT hits associated to the tracks. These tracks in particular have only CFT hits associated to them, and so are not affected by the presence of an extra silicon layer (other than helping to reduce the total number of CFT only tracks found). As previously stated, only tracks with ≥ 2 SMT hits are considered for $x-y$ vertexing, and hence are considered for input to the b-tagging or lifetime tools.

5.4.4 $x-y$ vertexing results

The other test of the new errors, and of the integration of Layer 0 into the SMT unpacker, is to investigate the $x-y$ vertexing results with and without Layer 0. Through examination of the x and y vertex resolutions and the number of tracks associated to the $x-y$ vertex in both Monte Carlo and data the effect of the addition of Layer 0 into the tracking software can be gauged.

A comparison of the x and y vertex resolutions in the QCD Monte Carlo is shown in figure 5.14, whilst the same for data is shown in figure 5.15. The x vertex resolutions in the Monte Carlo reveal an improvement of 1.3 μm when Layer 0 is used, whilst the y vertex resolutions show an improvement of 1.5 μm when Layer 0 is included. For the data sample an improvement of 4.3 μm is observed in the x vertex resolution

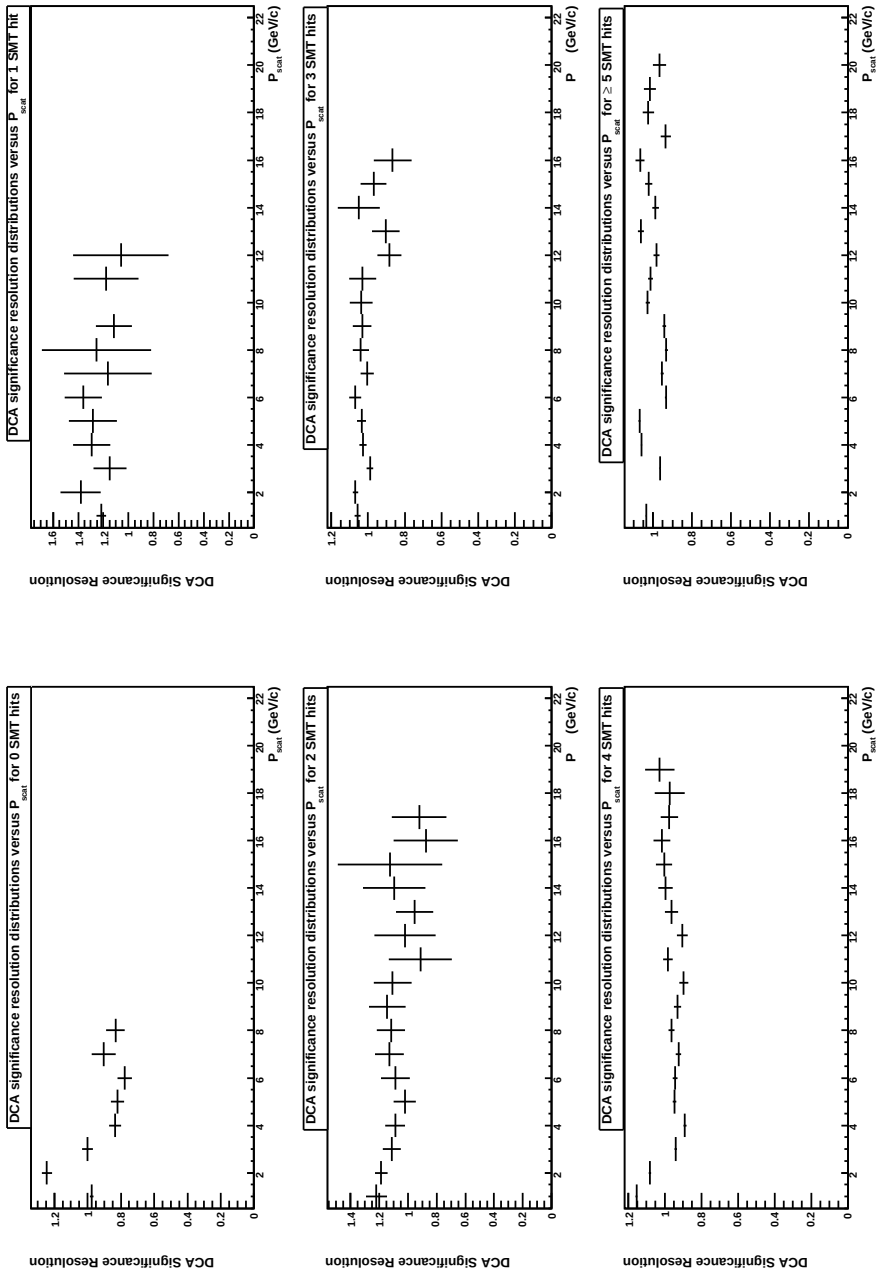

Figure 5.12: DCA significance resolution versus p_{scat} plots for the QCD Monte Carlo and the derived DCA error parameterization when Layer 0 is included. In order from top left to bottom right on the rotated figures are 0, 1, 2, 3, 4 and ≥ 5 SMT hits. Values close to 1 represent cases where the error parameterization has worked. The 0 and 1 SMT hit plots have values that lie far from 1, however this is acceptable as tracks must have at least 2 SMT hits in order to be considered to make a vertex. Missing entries on each plot are indicative of a failed Gaussian fit to that DCA significance distribution, usually due to a lack of statistics.

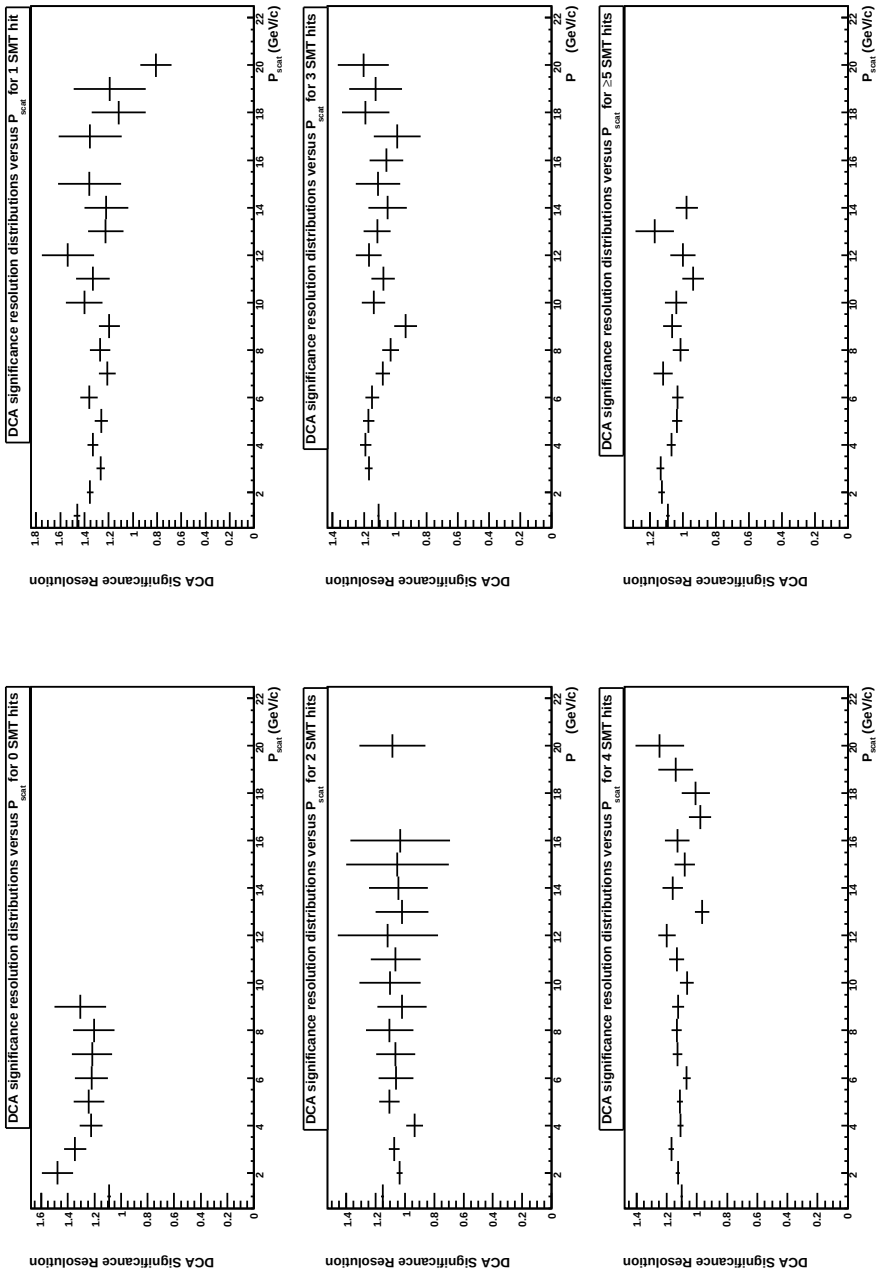

Figure 5.13: DCA significance resolution versus p_{scat} plots for the data sample and the derived DCA error parameterization when Layer 0 is included. In order from top left to bottom right on the rotated figures are 0, 1, 2, 3, 4 and $\geq$ 5 SMT hits. Values close to 1 represent cases where the error parameterization has worked. The 0 and 1 SMT hit plots have values that lie far from 1, however this is acceptable as tracks must have at least 2 SMT hits in order to be considered to make a vertex. Missing entries on each plot are indicative of a failed Gaussian fit to that DCA significance distribution, usually due to a lack of statistics.

and an improvement of 4.6 μm is seen in the y vertex resolution when Layer 0 is used.

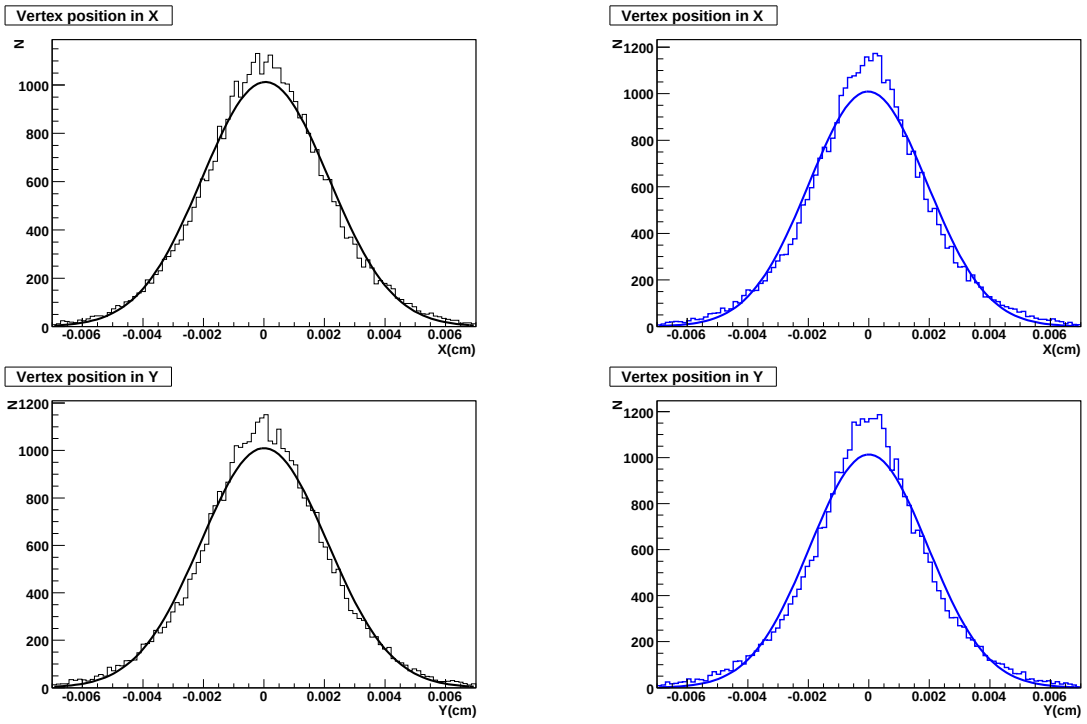

Figure 5.14: x (top) and y (bottom) vertex resolution comparison with (blue) and without (black) Layer 0 information included, for the QCD Monte Carlo sample. The x resolution without Layer 0 is 20.9 $\pm$ 0.1 μm and with Layer 0 is 19.6 $\pm$ 0.1 μm, whilst the y resolution without Layer 0 is 20.9 $\pm$ 0.1 and is 19.4 $\pm$ 0.1 with Layer 0 included.

The comparison between the number of tracks associated to the vertex with and without Layer 0 for the QCD Monte Carlo can be seen in figure 5.16, whilst the same comparison for data can be seen in figure 5.17. For the data the mean number of tracks associated to the vertex changes from 5.85 $\pm$ 0.01 without Layer 0 to 7.37 $\pm$ 0.01 with Layer 0, whilst a change from 8.48 $\pm$ 0.02 tracks without Layer 0 to 10.91 $\pm$ 0.03 tracks with Layer 0 is observed in Monte Carlo. These changes, combined with the improvement to the vertex resolutions, show that Layer 0 is helping to improve the quality of the returned vertices.

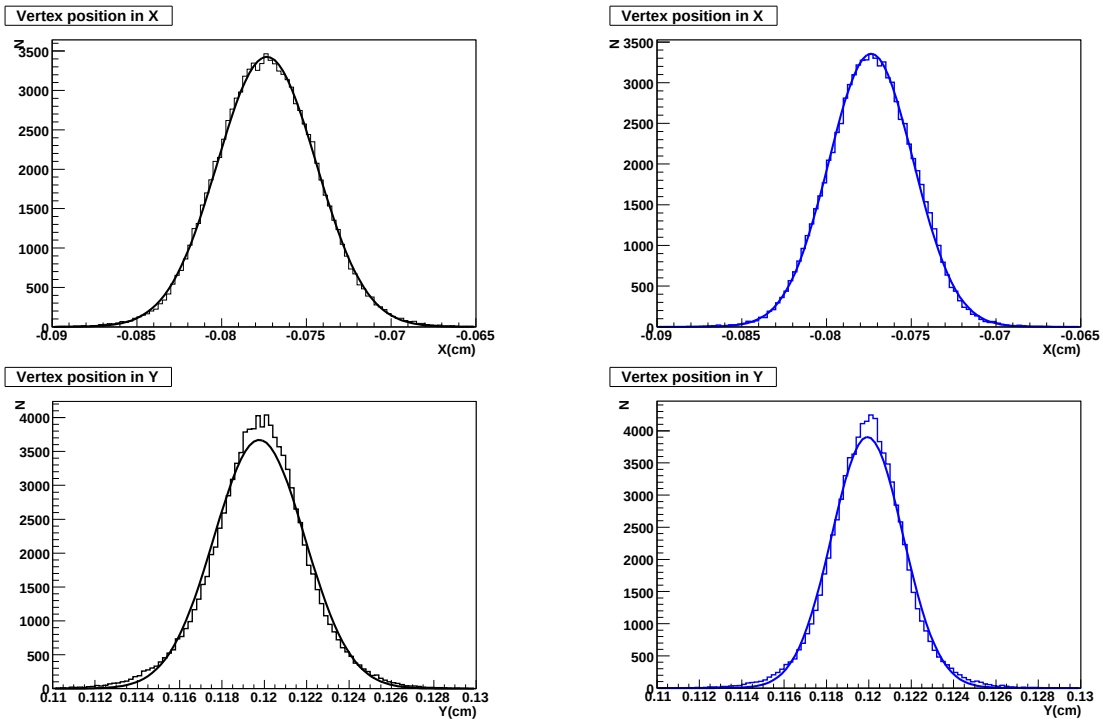

Figure 5.15: x (top) and y (bottom) vertex resolution comparison with (blue) and without (black) Layer 0 information included, for the data sample. The x resolution without Layer 0 is 29.2 $\pm$ 0.1 μm and with Layer 0 is 24.9 $\pm$ 0.1 μm, whilst the y resolution without Layer 0 is 21.5 $\pm$ 0.1 and is 16.9 $\pm$ 0.1 with Layer 0 included.

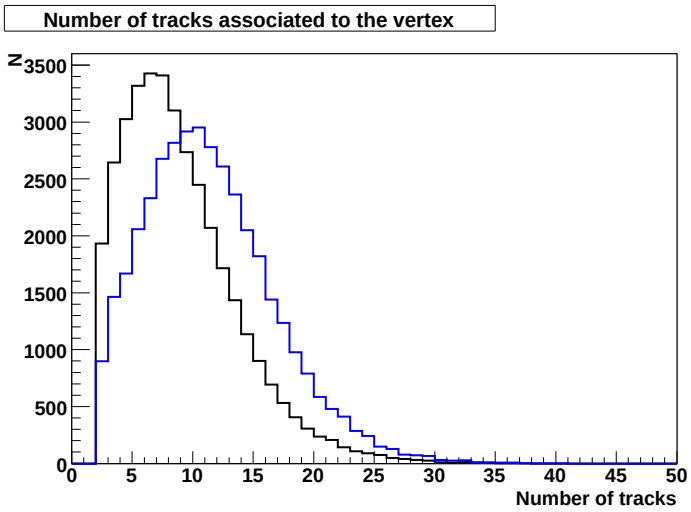

Figure 5.16: Comparison of the number of tracks associated to the $x-y$ vertex with (blue) and without (black) Layer 0 in the QCD Monte Carlo. The mean number of associated tracks with Layer 0 is 10.91 $\pm$ 0.03 and without Layer 0 it is 8.48 $\pm$ 0.02.

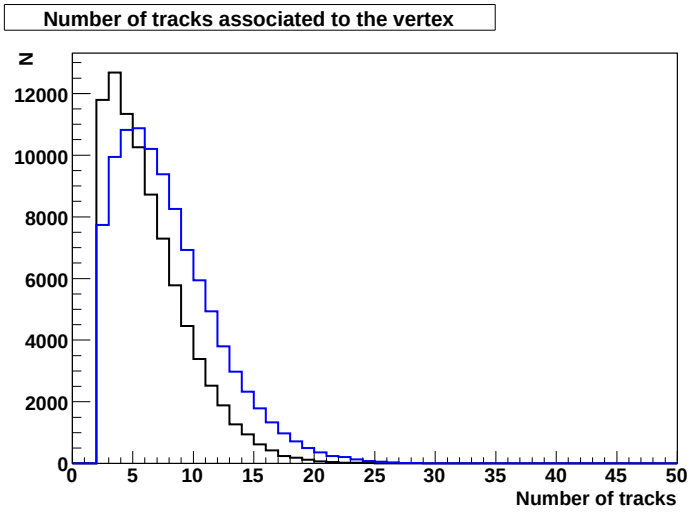

Figure 5.17: Comparison of the number of tracks associated to the $x-y$ vertex with (blue) and without (black) Layer 0 in the data sample. The mean number of associated tracks with Layer 0 is 7.37 ± 0.01 and without Layer 0 it is 5.85 ± 0.01.

5.5 Conclusions

This chapter details the inclusion of the new silicon sub-detector, Layer 0, into the Level 3 trigger, and in particular its inclusion in the SMT unpacker `L3TSMTUnpack`. It has also been shown that the detector is reading out correctly at Level 3 and is also integrated correctly within the Run IIb Level 3 tracking software, `L3TCFTTrack`.

The modifications made to the Level 3 SMT unpacker to include Layer 0 involved changes at both the data unpacking and the clustering stages. The results of these changes are a healthy number of Layer 0 clusters being produced and the expected full 2π coverage in ϕ (figures 5.3 and 5.4). These clusters are being used to help improve the tracks coming from the tracking algorithms as shown in figure 5.7 and particularly in figure 5.9 which shows an overall DCA resolution improvement for all tracks of around 50%. New silicon hardware and read out software means that new DCA track errors were required, the results of which are shown in figure 5.11 and table 5.2.

Combined with newly paremeterized DCA errors, the extra silicon layer, and the improved DCA resolution it provides, helps with vertex finding by adding clusters

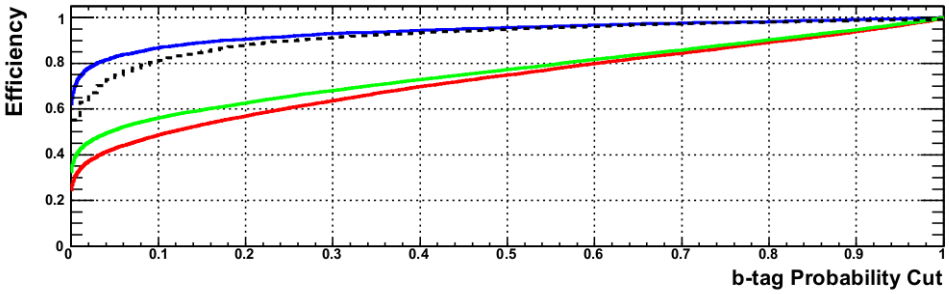

Figure 5.18: The Level 3 b-tagging efficiency (the number of correctly found b jets divided by the number b jet possibilities) versus b-tag probability cut (that is the probability that a jet contains a b quark) for a previously identified sample of b jets with Layer 0 included (blue) and without Layer 0 included (black, dashed line). The green line represents a background sample of high luminosity data (2.5 x 10^{32} cm^{-2}s^{-1}), whilst the red line represents a background sample of lower luminosity data (0.9 x 10^{32} cm^{-2}s^{-1}) [74].

that lie closer to the beam pipe, and thus, closer to the interaction point where the primary vertex lies. Both the vertex resolutions (figure 5.15) and the mean number of associated tracks to the vertex (figure 5.17) show an improvement when Layer 0 is included, the resolutions improving by 4.3 μm in x and 4.6 μm in y and the mean number of tracks increasing by 1.52, in the data sample. Improvements are observed in the QCD Monte Carlo sample too (see figures 5.14 and 5.16 for vertex resolutions and the associated number of tracks respectively).

The DCA errors derived here for the Layer 0 enabled Run IIb Level 3 tracking software are then subsequently used in both the lifetime and b-tagging tools, the results from which are directly used to make triggering decisions at Level 3. The b-tagging tool, for example, shows a noticeable improvement in tagging efficiency when Layer 0 is enabled at Level 3, as shown in figure 5.18 where it can be observed that the tagging efficiency for lower values of b-tag probability (that is the probability that the jet contains a b quark) is greatly improved when Layer 0 is included in the Level 3 track reconstruction. For example, at a b-tag probability cut of 0.1 (representing a tight cut), the b-tagging efficiency increases by nearly 10% for a previously identified sample of b jets, and thus more b jets would pass the trigger and get recorded [74]. This improvement translates into a direct improvement in the b-tagging trigger efficiencies.

The Layer 0 modifications, and the associated DCA errors, are currently running online and have been since early April 2007 and to date have been used to collect over 3 fb^{-1} of data*. Whilst new pedestal parameterizations have been made and previously dead HDIs brought back into the read out, the Layer 0 code changes made to the Level 3 SMT unpacker are independent of these and currently there are no plans to further update or modify the core SMT unpacking code.

*Considering only the data taken since Layer 0 readout was included in the online Level 3 framework.

Chapter 6

Di-J/ψ mass spectra at DØ

6.1 Preface

This chapter describes the studies made of the di-J/ψ mass spectrum after previous studies into the di-J/ψ channel revealed an anomalous peak. The di-J/ψ channel is an important probe of the color octet model, as well as providing a potential search channel for both the η_b and Higgs particles in beyond the SM models. Studies of J/ψs were used to derive an ideal set of cuts, whilst blind to the final di-J/ψ mass. These were found to be too harsh when applied to the di-J/ψ system, and so an alternative set of cuts was obtained by looking at the signal to background and total yield values of the di-J/ψ system, whilst still remaining blind to the final di-J/ψ mass spectra. As a further cross-check the cuts used to obtain the di-J/ψ spectra in the original analysis which saw a possible excess were then repeated.

6.2 DØ reconstruction software and the BANA analysis suite

The analyses shown here used data reconstructed by the official DØ reconstruction software, d0reco. The p17 version of d0reco for Run IIa data and the p20 version of d0reco for Run IIb data. These data are then used by the BANA analysis suite

[75], which provides tools for vertexing of tracks and muons. Details on the DØ reconstruction software can be found in section 3.3.

BANA works by converting tracks, found by the reconstruction software, into pseudo-particle classes. These can be vertexed together to make combination particles, deriving both vertex position, momentum and relevant masses of the combination. BANA also allows for the association of muons to tracks, thus creating track-matched muons, and provides an interface to all of the standard muon information that is created by the reconstruction software.

6.3 Di-J/ψ analysis

Resonances in $c\bar{c}-c\bar{c}$ mass spectra can reveal many details of b-physics (for example $\eta_b \rightarrow J/\psi J/\psi$), and can also hint towards potential beyond the Standard Model physics signatures, and studies of cross-sections can reveal details of production mechanisms and further test the theory of QCD. For example, SUSY Higgs decays can be searched for by looking for an increased production in a Standard Model process (for example an excess of muons coming from a Higgs decay), or by searching for an excess in a kinematic distribution that is not predicted by Standard Model processes. One example of this is the decay of a light NMSSM Higgs to four muons [32]. Further details of di-J/ψ production mechanisms can be found in section 1.5.

A previous DØ analysis [76] looking into the di-J/ψ decay channel (where the two J/ψs each decay to two muons) observed an unpredicted excess at around 13.7 GeV/c^2 with a signal significance $>5\sigma$. This can be seen in figure 6.1. This analysis used 1 fb^{-1} of Run IIa data, a mixture of d0reco versions, p14 and p17 and asymmetric J/ψ mass windows. The analysis that follows is a follow up to this previous analysis to try and verify the findings.

The analysis for this channel is described below. The initial procedure used for the analysis involved studies of the muons and J/ψ states to develop suitable cuts for the di-J/ψ state, whilst remaining blind to its mass. However, once the di-J/ψ box was opened it was discovered that these cuts were too tight given the data sample used.

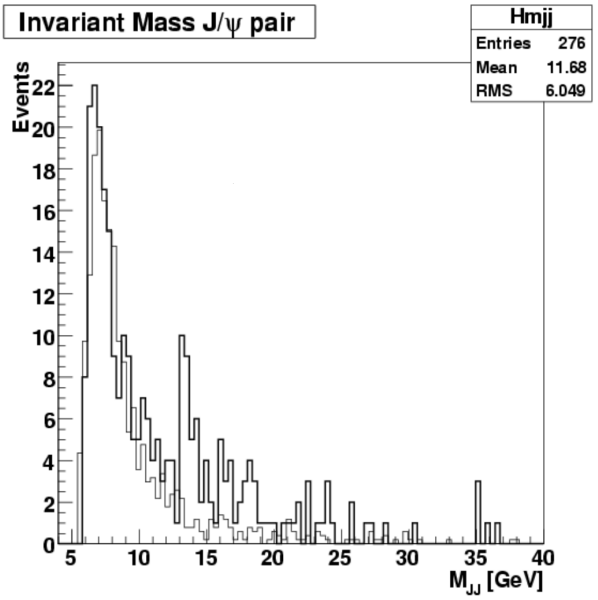

Figure 6.1: Di-J/ψ mass distribution from the original analysis. A possible excess was observed at $\sim$13.7 GeV/c^2. The background estimation shown here is from an analysis of the J/ψ sidebands [76].

This then led to a study conducted using the di-J/ψ system. Here the first, and best quality, J/ψ was fixed and then cuts derived from studies of the second J/ψ. The results were then compared to the original analysis and conclusions derived.

6.3.1 Data selection and reconstruction

For the following analysis 2.8 fb^{-1} of DØ Run II data were used, comprising of both Run IIa and Run IIb data - both of which were treated separately initially and then the results combined together. The data has been skimmed to produce a smaller subset that contains at least one dimuon state. In addition, special Monte Carlo for this decay channel was produced using Pythia 6.323 [71] and EvtGen [77], with a di-J/ψ mass of 13.7 GeV/c^2. The di-J/ψ was then forced to decay to two J/ψs, which then each decayed to two muons. The Monte Carlo was generated using the following selection requirements during the generation stage:

- At least two muons, from the same dimuon, with $p_T > 1.5$ GeV/c
- At least two muons, from the same dimuon, with $|\eta| < 2.2$

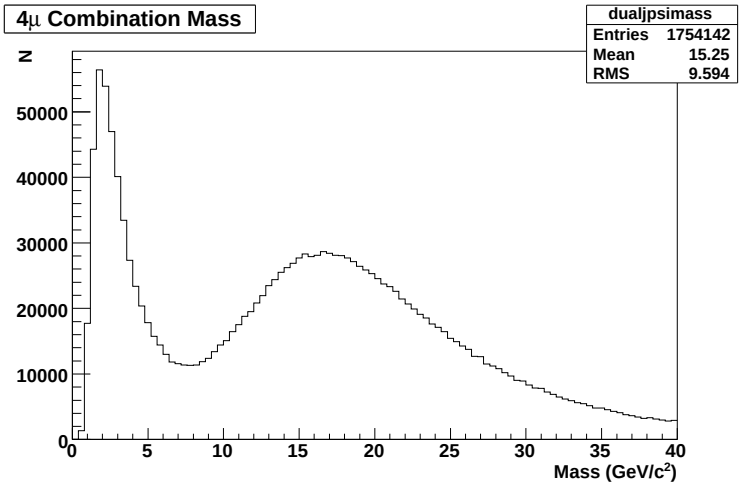

Figure 6.2: Di-J/ψ candidates in the data sample before any cuts are imposed.

These two criteria ensure that the majority of the muons in a simulated event will be reconstructable. The generator output is then passed through the official DØ detector simulation, digitization and reconstruction software, and then finally through BANA to reconstruct the simulated event. The Monte Carlo is for Run IIa only and as such was reconstructed using the p17 version of the d0reco software.

To reconstruct the di-J/ψ candidate itself, first two separate dimuons must be made. These dimuons must come from the same primary vertex in the event, to allow for a good 4μ vertex to be made. Once the dimuon vertices have been found, the four component muons, two from each dimuon, are then combined together to form a 4μ state. J/ψ mass window cuts on the dimuons are used to then select only those 4μ candidates which correspond to a di-J/ψ state. Vertex constraints are imposed on both dimuon vertices and the 4μ vertex to help ensure that good quality vertices are obtained. In addition these vertex constraints allow for J/ψ mass constraints to be used at a later date, that is to fix the mass of the dimuon state at the J/ψ mass and then calculate momentum correction factors for the muons which can then be applied to the di-J/ψ state. The di-J/ψ mass plot in data before any cuts are imposed can be seen in figure 6.2.

6.3.2 Errors

The statistical errors used in this analysis are all assumed to based on Poisson distributions. For this distribution the mean, λ, is equal to the variance of the distribution. So hence, the standard deviation of the distribution will be:

$$\sigma = \sqrt{\lambda}$$

This means that in a binned histogram, the error on each bin will be equal to $\sqrt{N}$, where N is the number of entries in that bin. In the limited scope of this analysis, statistical errors only will be considered. Further investigation into the low-p_T multi-muon channel would warrant a full analysis of the systematic errors too.

6.3.3 Basic muon and J/ψ kinematics

The dimuon is one of the most well known, yet most important signals in the field of b-physics. Plumbing the depth of its many resonances has led to several of the biggest discoveries in the field, including the discovery of the c and b quarks through the observation of the J/ψ [78, 79] and Υ [80] resonances respectively. The Tevatron produces lots of dimuon particles every day, and their distinctive signature of two muon segments makes them an excellent trigger.

To produce a dimuon sample, we first need to ensure that we have good quality muons matched to tracks. This involves looking at both the track quality and the quality of the segments in the muon system itself. The variables in question are the track p_T, the number of CFT hits ($nCFT$), the number of SMT hits ($nSMT$) and the location of the muon segments, described by a quantity known as $nseg$ and explained in more detail later on. To avoid cutting too much potential signal, the aim is to make these cuts as loose as possible, removing only those muons that are of dubious quality. There is a minimal momentum requirement for the muons to pass through the tracking and calorimeter volumes to reach the muon detectors, and as such we can place a lower limit on the track p_T of the muons of:

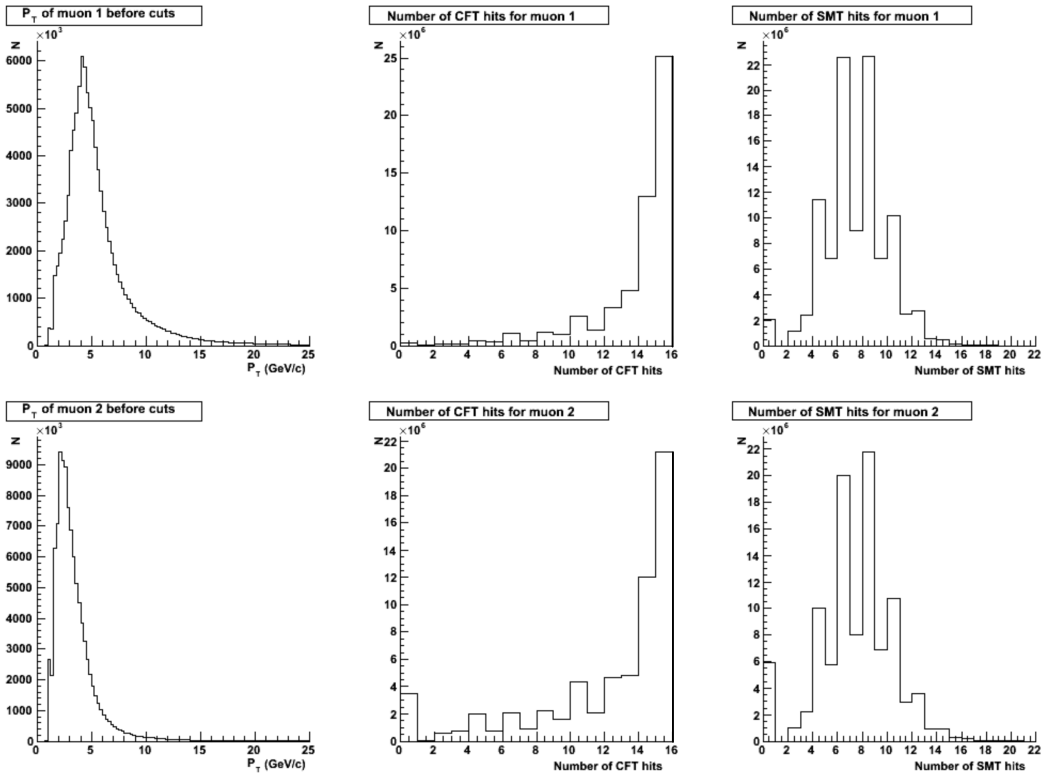

Figure 6.3: Basic track properties (p_T, $nCFT$ and $nSMT$) for muon constituents of a dimuon, which pass a p_T cut of 1 GeV/c. Muon 1 (upper row) is the higher p_T muon of the two.

- Track $p_T > 1$ GeV/c for each muon

This value of 1GeV/c relates to the momentum required for a muon to pass through the least dense area of the calorimeter (that is between the calorimeter cryostats) and into the first layer of the muon system. Figure 6.3 shows the distributions for the track p_T, $nCFT$ and $nSMT$ for muons which combine into a dimuon, after placing the p_T cut.

As can be seen in figure 6.3, the distribution for $nCFT$ shows that the majority of the muons have at least 14 CFT hits. Similarly, the majority of muons also have more than one hit in the silicon. More silicon hits leads to better momentum resolution, and hence a better vertex for the combined dimuon. In addition to this, for a central muon ($|\eta| < 1.0$) to hit the central muon system, passing through the calorimeter, requires a muon p_T of 1.5 GeV/c. Hence the following cuts can be made:

- At least 1 CFT hit on each muon
- At least 1 SMT hit on each muon
- $p_T > 1.5$ GeV/c if there is a hit in the muon system

The quality, and location, of the segment in the muon system is defined by the *nseg* value of the muon. The *nseg* scale is described in table 6.1 below.

nseg Value	Meaning
3	Well matched muon to track with PDT hits in A and B or C layers
2	Track-matched muon with a PDT hit in either B or C layers
1	Track-matched muon with a PDT hit in the A layer
0	Track-matched calorimeter muon defined as a minimal ionizing particle in the calorimeter

Table 6.1: Table showing the relevant values of track-matched muon *nseg* used in this analysis [81].

Figure 6.4 shows the muon *nseg* distributions with the already decided track quality cuts applied. Muons with an *nseg* value of 0 are calorimeter only muons matched to a track, and as such are of dubious quality unless paired with a much higher quality muon, and as such the requirement here that all muons used have at least one segment in the muon system is imposed, that is:

- Muon $nseg > 0$

By imposing the requirement that the dimuon contain opposite sign muons, that is a combination charge of zero, a simple dimuon mass can be produced, using the PDG value for the muon mass [7]. The mass produced comes from the resultant momentum vector for the combination of the two muons. Vertex constraints are further applied to improve the resultant momentum vector and mass of the dimuon. The dimuon mass spectrum can be seen in figure 6.5. The J/ψ resonance is clearly visible at about 3.1 GeV/c^2.

Fitting a Gaussian for signal, and a simple linear polynomial for background estimation, an estimate of how many J/ψs are in the data can be made. A close up of the

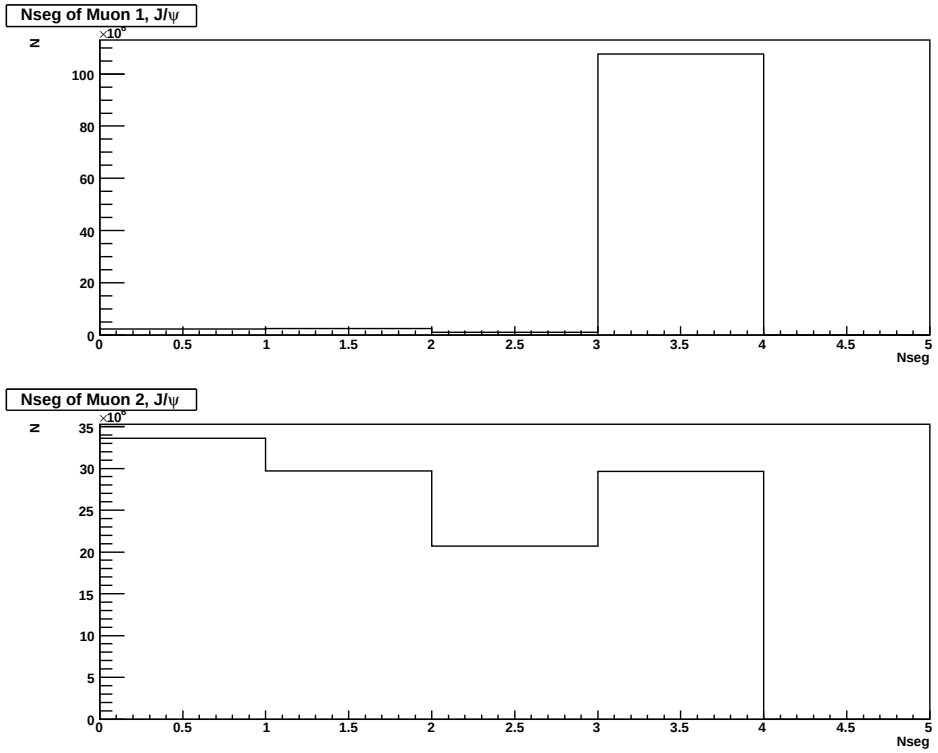

Figure 6.4: $Nseg$ values for muons making up a dimuon after applying simple track quality cuts. The highest p_T muon is at the top.

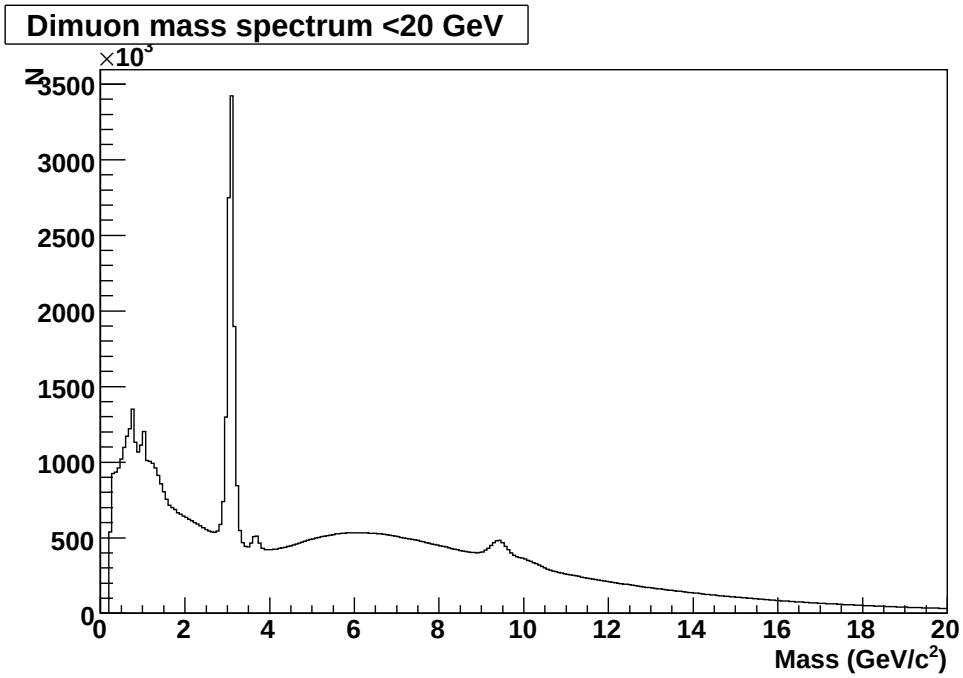

Figure 6.5: The dimuon mass spectrum between 0 and 20 GeV/c^2 using only the basic muon cuts described in section 6.3.3.

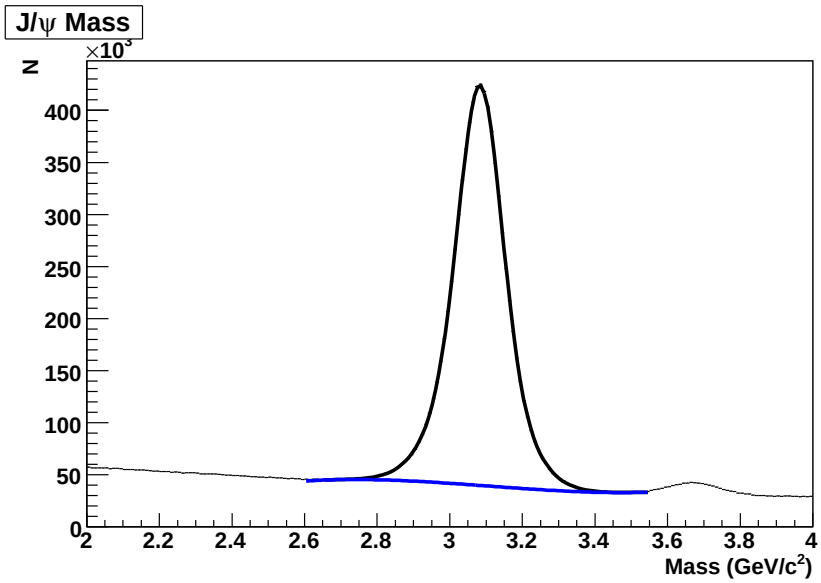

Figure 6.6: Close up of the J/ψ mass region. Fits for signal (in black) and background (in blue) allow for an estimate of the number of J/ψs under the peak.

J/ψ peak can be seen in figure 6.6. From this plot the number of J/ψs is estimated to be around 7.6 million. The mass window used to obtain that number is 2.9 to 3.3 GeV/c^2, and this is also the mass window used throughout this analysis. Using this mass window and the basic cuts described above results in about 1600 di-J/ψ candidates for use in this analysis.

During this process it was discovered that certain regions of the detector, in η-ϕ space, produced a much higher event rate than the rest of the detector. This can be seen in figure 6.7. These muon 'spikes' are caused by the former presence of the old Main Ring accelerator passing through the calorimeter cryostats. It is located off-center to the Tevatron beampipe, hence the displacement in η-ϕ. During the Run II upgrade the Main Ring beampipe was removed and the gap in the calorimeter filled with concrete. This concrete leads to a less dense material for particles to pass through to hit the muon system, and hence a higher fraction of both low momentum muons, and other particles that were not absorbed by a full calorimeter volume, is obtained. To account for this any muons that lie within this 'spike' region are excluded. In particular, any muon located in the following region is excluded:

- $0.8 < |\eta| < 1.2$

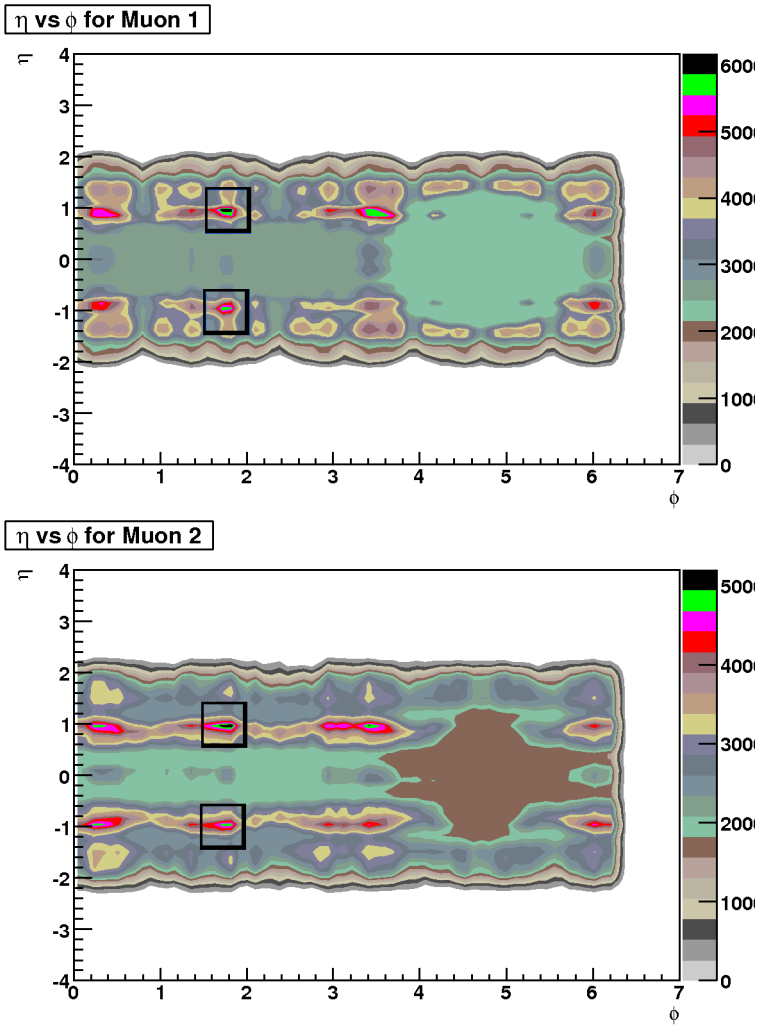

Figure 6.7: η versus ϕ for each of the muons, the highest p_T muon at the top. The 'spike' regions due to the former presence of the Main Ring passing through the calorimeter are clearly visible here. The 'spike' regions are excluded as a possible source of contamination, and the regions of exclusion are indicated by the black boxes on each diagram. The 'hole' at high values of ϕ is due to reduced muon coverage on the bottom of the detector.

- $1.6 < \phi < 2.0$

Studies of this region with J/ψs revealed that the vast majority of muons passing through this region were low p_T muons ($1.0 < p_T < 1.5$) and that the signal to background ratio for J/ψ production in the excluded region was significantly less than in other regions of the detector. Combined these have the effect of reducing the impact of the signal reduction due to the exclusion of the 'spike' region from what might be expected to about 4% of the total.

This 'spike' muon effect has been observed previously in other muon only analyses, in particular in the $ZZ \rightarrow 4\mu$ channel [82, 83]. However, due to the low momentum of the muons in consideration here the effect is more pronounced than in the ZZ channel. The 'hole' in the high ϕ region is due to a smaller number of muon detector layers at the bottom of the DØ detector, so as to make way for structural supports.

6.3.4 Deriving cuts from J/ψ data

Now that a basic data sample of J/ψs has been obtained, cuts can be derived using this data which can then be used in the di-J/ψ mode. The variables that will be looked at in particular are:

- Di-J/ψ vertex χ^2
- Muon opening angle, α
- Impact parameter cuts
- Muon scintillator timing cuts
- Distance between hits in the innermost muon layer

These variables will be covered one by one in turn. For each of the variables in question, histograms of the J/ψ and di-J/ψ masses for those events which fail the cuts are supplied. Histograms with either few or no entries in them indicate where the given cut removes few or none of the events being tested within the mass region of interest.

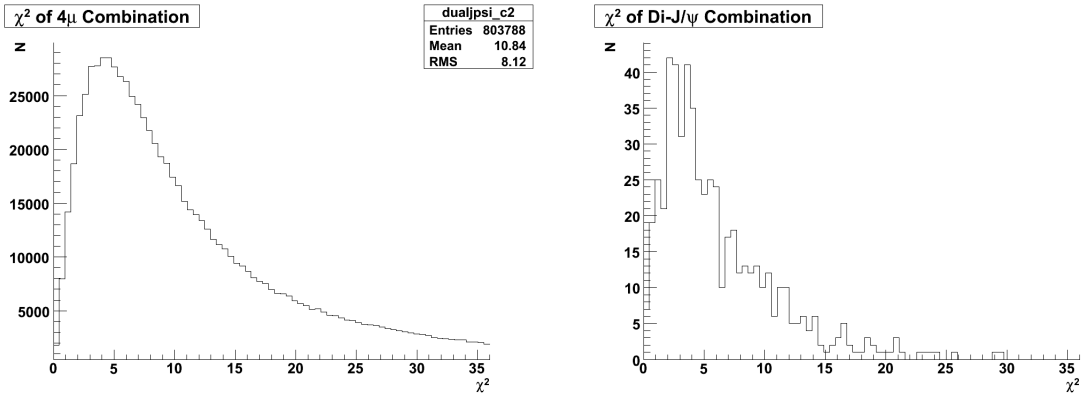

Figure 6.8: Plot showing the χ^2 distribution for a 4μ vertex in both data (left) and Monte Carlo (right).

Di-J/ψ vertex χ^2

The vertex for the di-J/ψ particle is made from the combination of the four component muons, after they have previously been successfully combined into dimuons. The quality of the vertex is measured by its χ^2 value.

In general, a smaller χ^2 corresponds to a better quality vertex. Figure 6.8 shows the 4μ vertex χ^2 in both the data and in the Monte Carlo simulation using the simple cuts described in section 6.3.3, and figure 6.9 shows a comparison between Monte Carlo and data for the dimuon vertex for the same cuts. The agreement between the Monte Carlo and data allows for the cuts to be based on Monte Carlo and thus the Monte Carlo 4μ vertex can be used to derive a possible cut for the vertex in data.

From this the following χ^2 cut is made:

- $\chi^2 < 25$

This cut allows for a lot of the poor quality 4μ combination vertices to be removed, whilst still retaining a large fraction of the total yield. A plot of the dimuon and di-J/ψ masses for those candidates which did not pass the χ^2 cut can be seen in figure 6.10. In the di-J/ψ plot a J/ψ mass window of 2.9 to 3.3 GeV/c^2 is used.

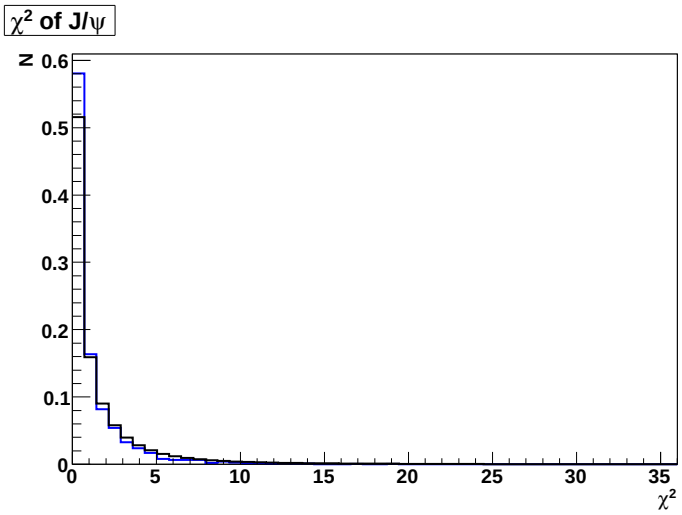

Figure 6.9: Normalised plot showing the relative χ^2 values for a dimuon vertex in both Monte Carlo (blue) and data (black).

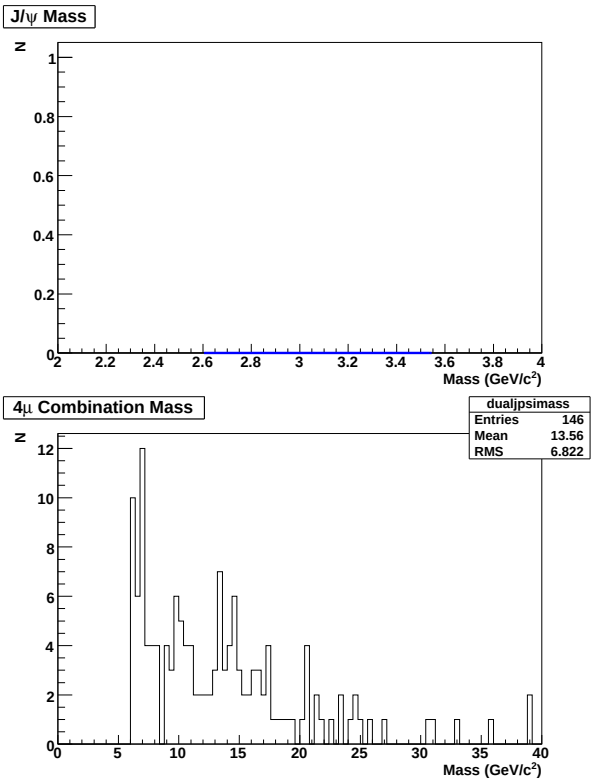

Figure 6.10: Plot showing the dimuon (first plot) and 4μ (second plot) mass spectrum for those candidates which fail the vertex χ^2 cut of < 25. There are 0 J/ψs and 190 ± 10 di-J/ψs which fail the χ^2 cut. The empty plot indicates that no events fail the cut within the given mass window.

Muon opening angle, α

There lies a possibility that two reconstructed muons in a di-J/ψ candidate are just two different tracks matched to the same muon segment - or vice versa. To help ensure that the final data sample of di-J/ψ events contains four distinct muons, a cut on the opening angle between each possible dimuon track combination can be placed. This angle, α, is calculated from the difference in η-ϕ between the two muons. The use of the opening angle in this analysis is analogous to the opening angle cuts used in similar searches involving J/ψ decay products [84].

For the dimuon case, this is simple and one possible angle is obtained. However, for the 4μ state all combinations of tracks must be considered, hence six muon angles from all four muons are obtained. All of these angles must then pass the α cut, or in this case a $\cos(\alpha)$ cut for simplicity. Figure 6.11 shows the distribution of $\cos(\alpha)$ values for all six possible combinations of muons, whilst figure 6.12 shows a close up of the $\cos(\alpha)$ distributions around +1.0.

The Monte Carlo simulations of the di-J/ψ decay suggests that the muons will be well separated. In terms of $\cos(\alpha)$ this means values < 1.0. Analysis of the Monte Carlo result leads to the conclusion that the following α cut would be suitable:

- $\alpha > 10\,^{\circ}$, (equivalent to $\cos(\alpha) < 0.9848$)

Figure 6.13 shows the J/ψ and di-J/ψ mass plots for those candidates which fail this cut. Again, a J/ψ mass window of 2.9 to 3.3 GeV/c^2 is used.

Impact parameter cut

Long-lived particles can decay to J/ψs and so could possibly contribute to both data samples, J/ψ and di-J/ψ. J/ψs from these particular mesons would hence be produced far from the primary vertex, and hence the muons too will be produced far from the same vertex. By placing cuts on the impact parameter, the distance of the track from the primary vertex, the long lived meson decays can be removed.

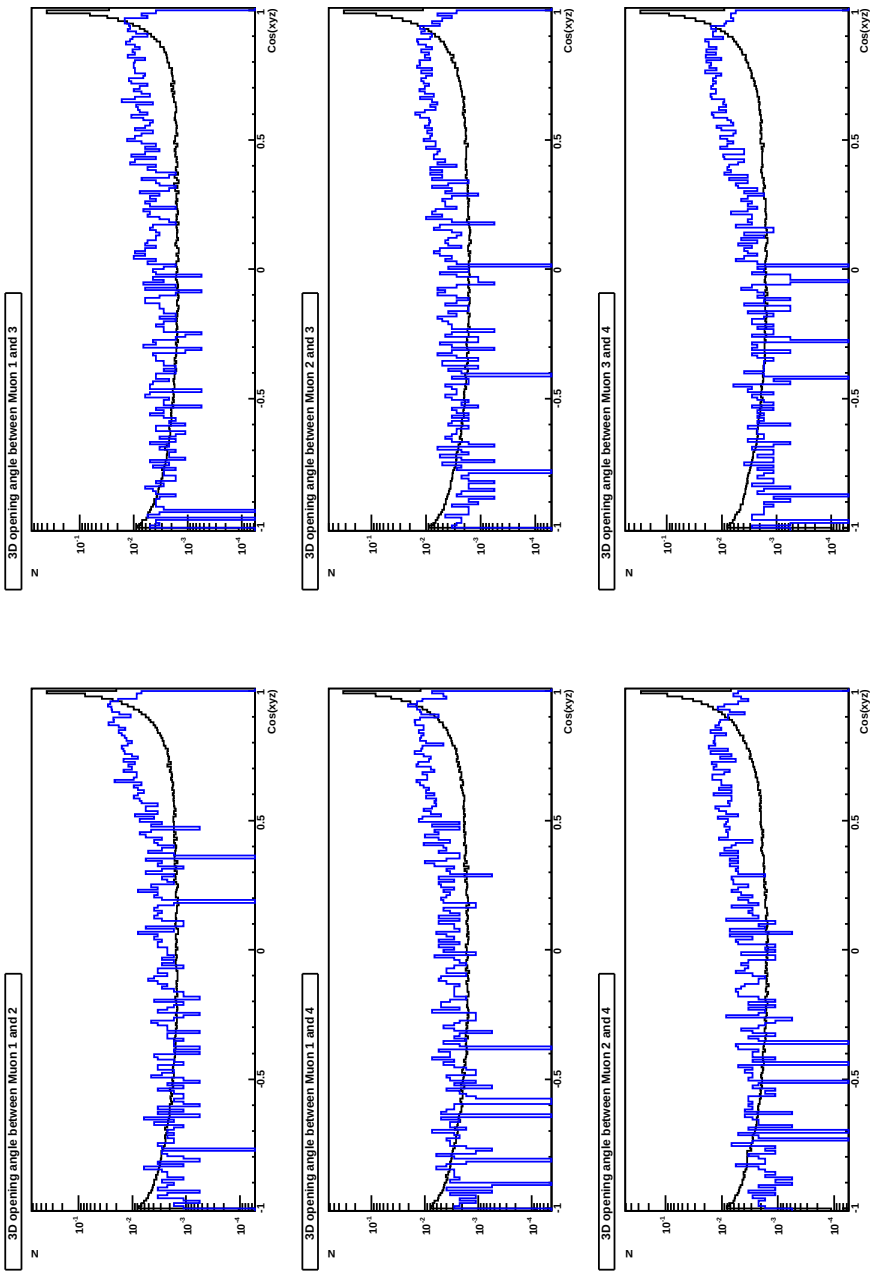

Figure 6.11: cos(α) distributions for all six combinations of four muons, for both data (black) and Monte Carlo (blue). Both distributions are on a log scale, and have been normalized to 1.

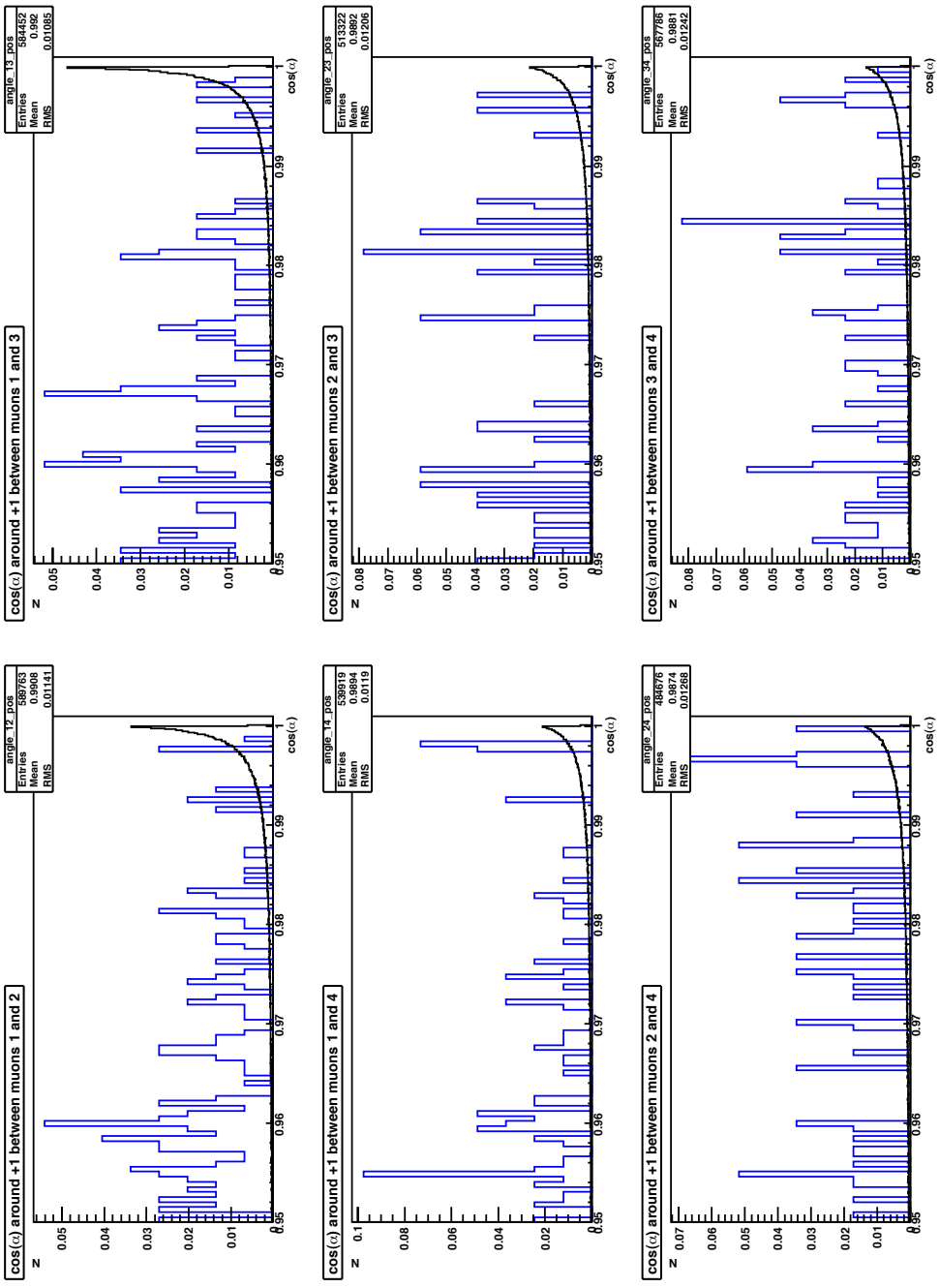

Figure 6.12: A close up of the $\cos(\alpha)$ distributions around +1.0 for all six combinations of four muons, for both data (black) and Monte Carlo (blue). Plots have been normalized to 1.

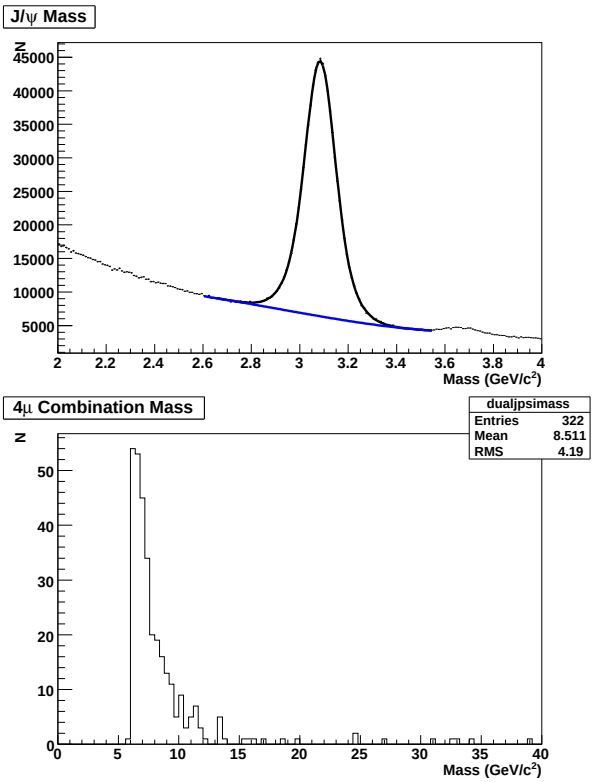

Figure 6.13: Dimuon and di-J/ψ mass profiles for those candidates which fail the $\alpha > 10\,^{\circ}$. There are 648000 $\pm$ 1000 J/ψs and 430 $\pm$ 20 di-J/ψs which fail the opening angle cut.

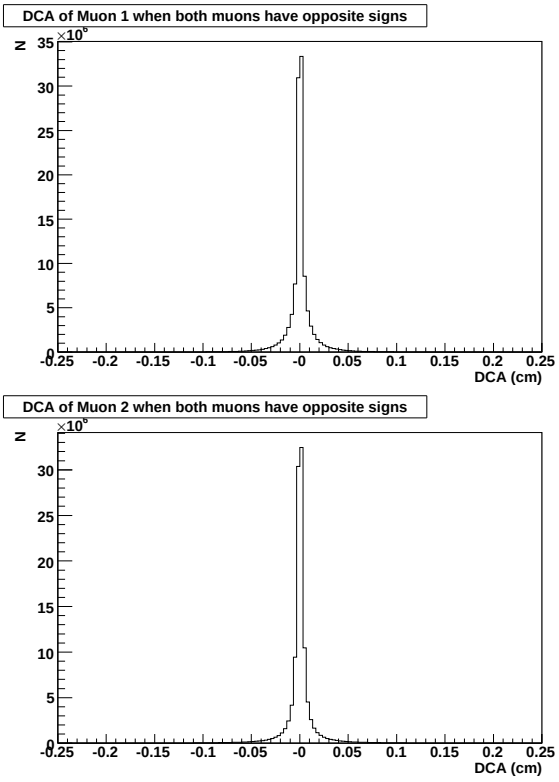

Figure 6.14: Impact parameter distributions for dimuon component muons in Monte Carlo. The highest p_T muon is on top.

The original analysis used a loose cut on the lifetime significance to accomplish this distinction between prompt J/ψ production and J/ψs from long-lived particles. In addition, this cut will help to reduce contributions from cosmic rays as these would be seen as not coming from the primary vertex either.

Figure 6.14 shows the J/ψ component muon impact parameter distribution. Here the impact parameter is defined as the distance of closest approach (DCA). The majority of muon DCAs lie close to 0 cm, that is close to the primary vertex. So this leads to the following cut on the data:

- |Muon DCA| < 0.1 cm

The di-J/ψ mass plot for those candidates that fail this cut can be seen in figure 6.15. This plot uses, as ever, a J/ψ mass window of 2.9 to 3.3 GeV/c^2. This figure also shows the dimuon mass distribution for those events which fail the mass cut.

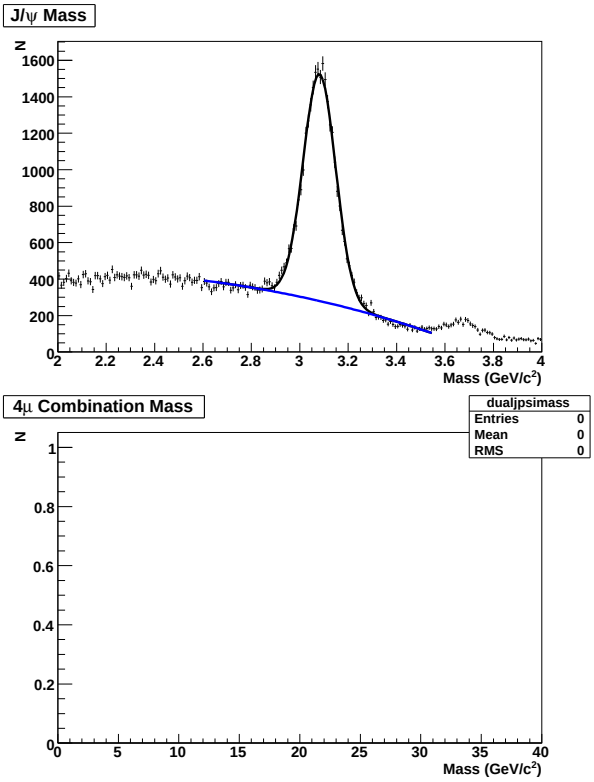

Figure 6.15: Dimuon and di-J/ψ mass distribution for those candidates whose muons fail the impact parameter < 0.1 cm cut. There are 21000 ± 200 J/ψs and 0 di-J/ψs which fail the impact parameter cut. The empty plot indicates that no events fail the cut within the given mass window.

Scintillator timing cuts

A dimuon candidate could just be a cosmic muon passing through the detector and causing muon hits on opposite sides of the detector. In addition, the cosmic muon could also strike the tracking system and hence create tracks that point to the muon hits. The result of this is then seen as two back-to-back muons that can then be combined to form a dimuon. In addition to the DCA cut, the number of possible contributions from cosmic muons can be reduced using timing information coming from the three layers of muon scintillators. Muons coming from normal beam collisions should have muon scintillator times close to zero (zero being when the beam-beam interaction is assumed to occur), and the difference in the scintillation times (Δt) should also be very close to zero. Cosmic muons can hit at any time and since they are travelling straight through the detector, rather than radially out from the centre, there will be a large Δt between scintillator hits.

The standard cuts for scintillation times used to remove cosmic muons [81]:

- |A-layer time| < 10 ns
- |B-layer time| < 10 ns
- |C-layer time| < 10 ns
- $\Delta t_A < 12$ ns

Unfortunately not all muons have scintillator timing information in all three layers of the muon system, so cuts will only be applied when the scintillation layer in question has timing information available. Similarly, both muons require timing information for layer A for the Δt cut to be considered. The dimuon and di-J/ψ mass plots for those candidates with muons which fail these timing cuts can be seen in figure 6.16.

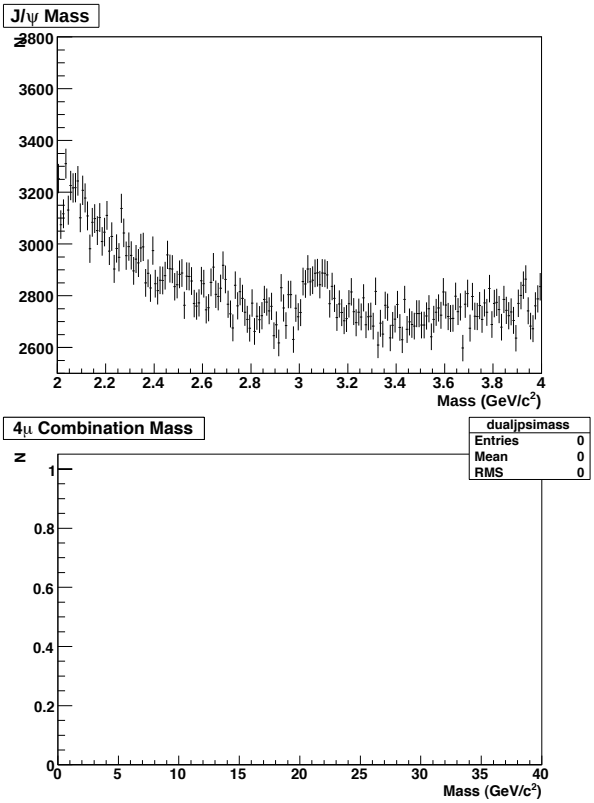

Figure 6.16: Dimuon and di-J/ψ mass plots for those candidates which fail the muon scintillator timing cuts. There are 5880 ± 400 J/ψs and 1 ± 1 di-J/ψs which fail the scintillator timing cuts. The empty plot indicates that no events fail the cut within the given mass window.

Muon hit distance cut, ΔR_A

The final cut that will be considered is the distance between hits in the muon system. In particular the distance between muon hits in the first layer of the muon detector, layer A, will be considered. By looking at this particular information, an attempt to remove the particular case when one muon will hit in between two muon PDTs, and hence depositing charge in both PDTs, can be made. This then allows for the possibility that this will be reconstructed as two different, distinct muons. Hence, a fake J/ψ signal from these two supposed muons can be obtained. Layer A is cut on, rather than the other two layers, as layer A is situated before the Toroidal magnet, hence before the muons tracks have been bent by the Toroid.

Consideration of the distance between the PDTs in the first muon layer led to the decision to use the following cut:

- $\Delta R_A > 10$ cm

Using a J/ψ mass window of 2.9 to 3.3 GeV/c^2, the di-J/ψ mass plot in figure 6.17 can be made from those candidates that fail the ΔR_A cut.

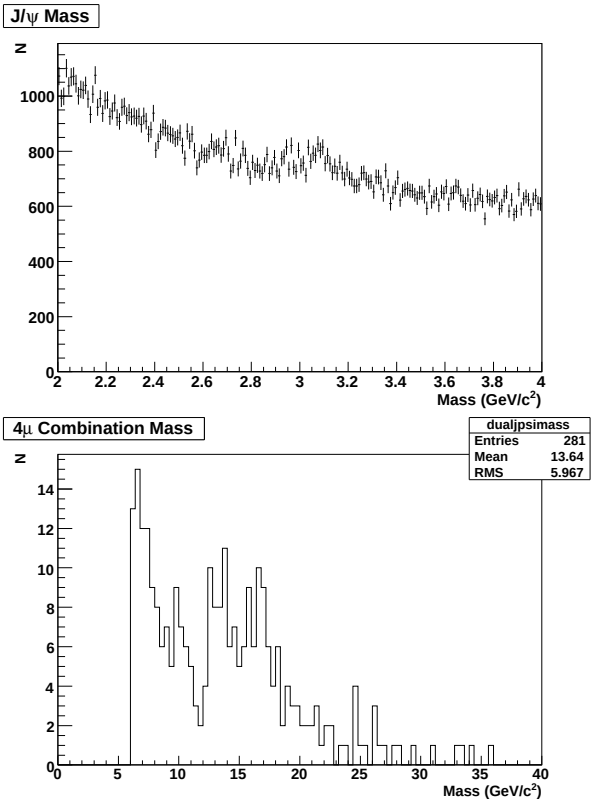

Figure 6.17: Dimuon and di-J/ψ mass plots for those candidates which fail the $\Delta R_A > 10$ cm cut. There are 2000 ± 200 J/ψs and 360 ± 20 di-J/ψs which fail the ΔR_A cut.

6.3.5 Background estimation

Before the box can be opened on the di-J/ψ mass plot for those candidates which pass the above cuts, the possible backgrounds need to be examined. In particular, same sign muon backgrounds, sideband backgrounds and mixed event backgrounds will be looked at. These backgrounds can reveal problems with the cuts or reconstruction of the 4μ vertex, as well as allow hints of a signal excess or deficit to be quantified properly.

Same sign muon background

To simulate the effect of miscalculating the charge of one of the two muons in the sample, we can consider what would happen when two same sign muons are combined into a dimuon vertex. In particular, the case where both dimuons contain same sign muons will be considered, hence both dimuons will have charges of either +2 or -2, but there are no requirements on charge for the combinaton 4μ vertex.

Figure 6.18 shows the 4μ combination mass when all the previously discussed cuts are used in combination with the charged dimuon requirement. Due to the nature of the estimation method, looking at the same sign background is likely to provide the most accurate portrayal of the real 4μ mass profile. However, as can be seen from the plot, this method of estimating the background suffers from limited statistics.

Sideband background

An efficient way of estimating what the background for the 4μ mass could look like is to investigate what happens when mass regions either side of the J/ψ mass window are used. For this mass regions lying 0.9 GeV/c^2 either side of the signal mass window upper and lower bounds shall be used. This means that the relevant mass regions are 2.0 to 2.9 GeV/c^2 and 3.3 to 4.2 GeV/c^2. The different regions used are illustrated in figure 6.19.

By combining one dimuon, with its mass lying in a sideband region, with another dimuon, which lies in the J/ψ mass window, a new 4μ mass profile can be obtained.

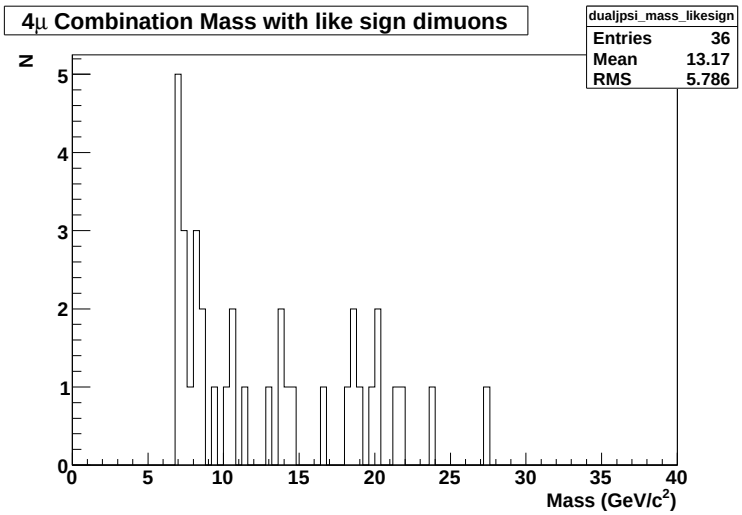

Figure 6.18: 4μ mass distribution using the same sign muon background model.

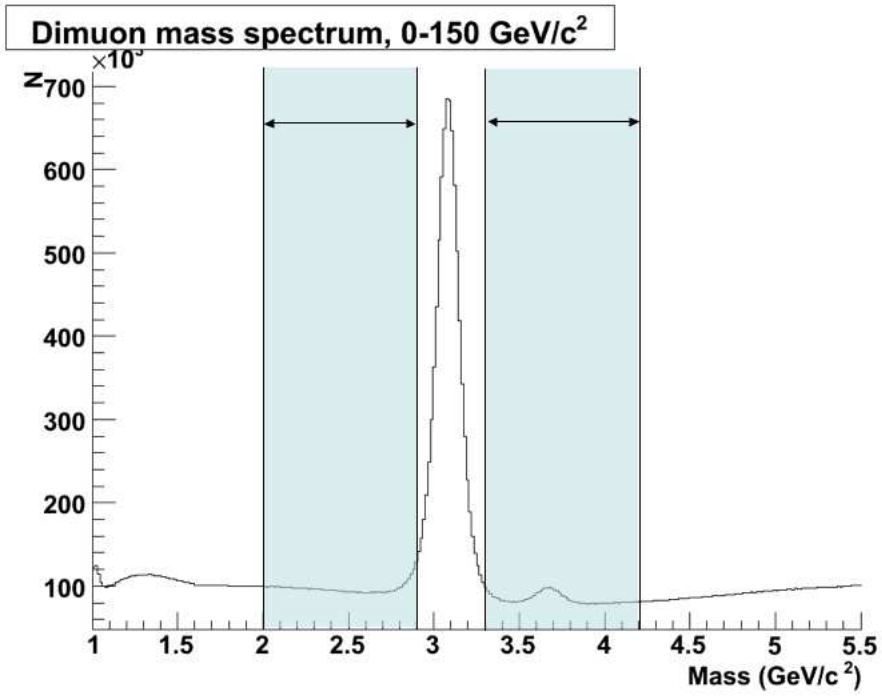

Figure 6.19: Illustration showing the regions in the dimuon mass spectrum used when calculating the J/ψ sideband background plot. The regions marked in blue represent the sideband regions that are being used here. The region in between the blue areas represents the J/ψ mass window.

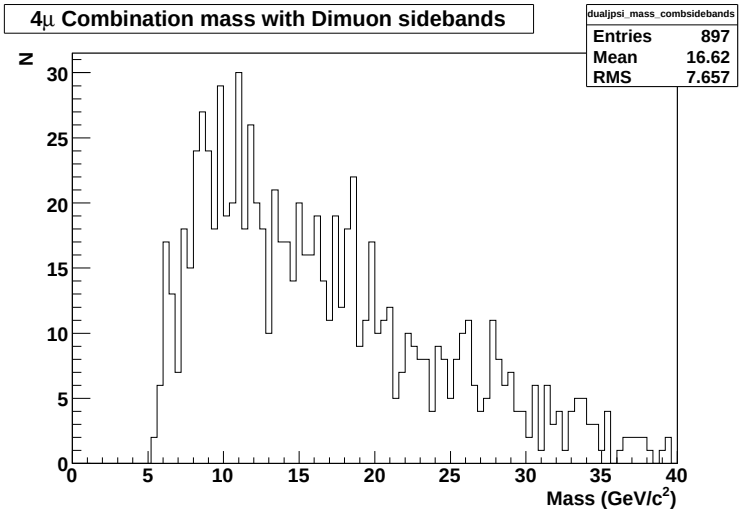

Figure 6.20: 4μ mass distribution using the J/ψ sideband background model. The sideband regions used are shown in figure 6.19.

This particular mass profile can be seen in figure 6.20. Here the plot extends to a lower mass than the di-J/ψ plot will have due to the fact that the dimuon mass' lower limit is 2.0 GeV/c^2 as opposed to 2.9 GeV/c^2 for the di-J/ψ plot. This estimation method benefits from much higher statstics, particularly in the low mass region where there are many possible sideband candidates with which to combine with a J/ψ. However, due to the nature of the dimuon mass spectrum, this process can lead to the inclusion of other dimuon resonances into the calculated 4μ mass.

Mixed event background

The final potential background sample that will be considered here is the mixed event background. This background is made up of combining a J/ψ from one di-J/ψ candidate with a companion J/ψ from another possible candidate. To help prevent potential problems with trigger bias, the higher p_T J/ψ from the first di-J/ψ candidate in an event will only be combined with the lower p_T J/ψ from the second di-J/ψ candidate, and vice versa. Once the J/ψs have been found in the different events, their constituent muons can then be combined together to form a new 4μ state. Since one particular event can be potentially combined with all others, a very large background sample is obtained, once all appropriate cuts have been made. A diagram to help explain this can be seen in figure 6.21.

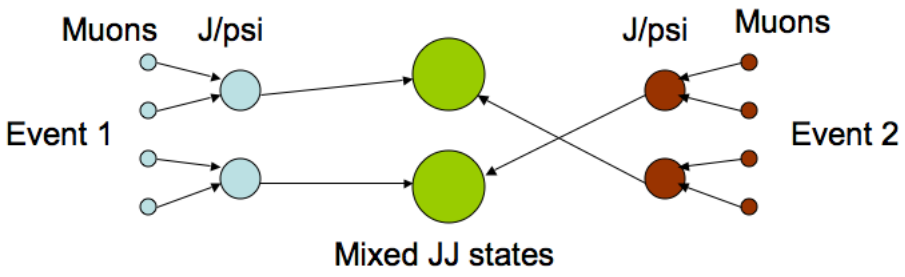

Figure 6.21: Diagram showing how the mixing of two different di-J/ψ candidates happens. After finding two different successful di-J/ψ candidates the J/ψs from each are then combined with each - J/ψ_1 from di-J/ψ_1 and J/ψ_2 from di-J/ψ_2, and vice versa - to produce two new background di-J/ψs.

Since the two dimuons are from different events they will very likely have different primary vertices, and as such the vertex constraint, where the dimuon vertices are constrained to come from the same primary vertex, will not work here; however the individual dimuons are vertex constrained separately. As such a full mass constraint will not work properly here either, as this ideally requires a vertex constraint too to provide a basis for momentum corrections. However, this does allow for a much simpler calculation of invariant mass using only the 4-vectors of the component muons.

This method can be used since the two individual J/ψs have already been located and identified. In addition to this, previous studies have shown that the vast majority of dimuons form a good vertex, as measured by the vertex χ^2. Both of these caveats must be true for the 4-vector method to be valid. Figure 6.22 shows the mass distribution obtained through this mixing of events.

As can be seen in figure 6.22 we obtain a background distribution with high statistics, to be expected given that one event is being mixed with every other event. This provides a mass distribution that is similar to that seen for the other background distributions in figures 6.18 and 6.20, although the distribution appears to tend towards peaking at a higher mass range compared to the other models.

The peaking of the distribution occurs at a higher mass compared to the 4μ distribution prior to any cuts being imposed, as shown in figure 6.2, (the mixed event

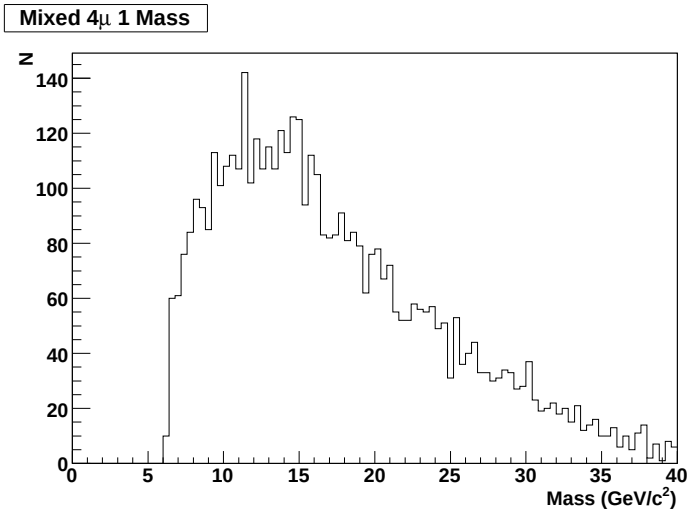

Figure 6.22: 4μ mass distribution using the mixed events background model. The background is created by mixing J/ψs from different events to create a new di-J/ψ candidate.

background peaks at around 14 GeV/c^2 whilst the 4μ background peaks at around 10 GeV/c^2). This indicates that this particular background model is unsuitable for use.

Background Normalization

In order to compare signal di-J/ψ candidates to those found in the background samples, the two samples need to be normalized. The chosen normalization method was to normalize both distributions to the same number of di-J/ψ candidates with a mass below 10 GeV/c^2. This particular value was chosen so as to avoid any potential bias being added to any possible excess occurring above the 10 GeV/c^2 threshold.

6.3.6 Results

From the three background models that have been looked at, the sideband background model seems to be the most appropriate. This is mostly due to the high statistics this model provides, whilst the background shape is the best fit to the expected distribution in data for the di-J/ψ mode.

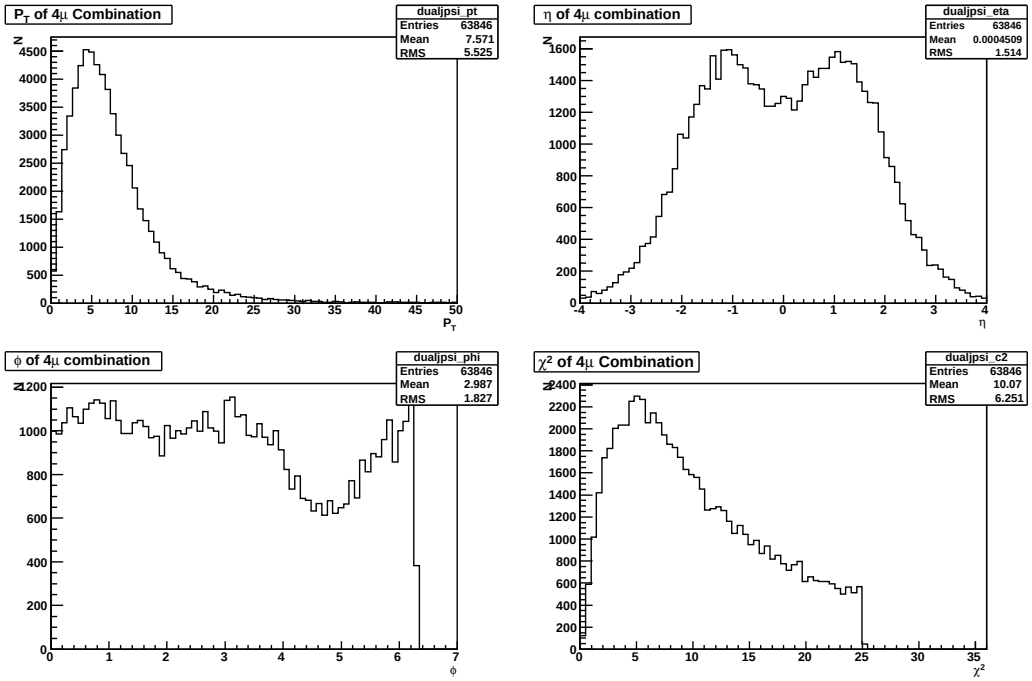

Figure 6.23: Kinematic plots for the di-J/ψ candidates produced using the old cut set. From the top left, these plots are di-J/ψ p_T, di-J/ψ η, di-J/ψ ϕ and di-J/ψ χ^2. The peaks in η around $\eta = \pm 1$ are due to the reduced coverage of the calorimeter in this region allowing a greater number of muons to pass through to the muon system (and in particular lower momentum muons). The dip in ϕ between 3.5 and 5.5 is due to the reduced PDT coverage at the bottom of the detector to make way for structural supports. Both of these effects are observed in each of the individual muon kinematic plots too, and after combination of the four muons to create the 4μ state the effects are still present.

One last check that needs to be completed before the di-J/ψ mass can be investigated is to check that the other kinematic variables for the di-J/ψ are sensible. The variables to be checked are the di-J/ψ p_T, η and ϕ and vertex χ^2. These can be seen below in figure 6.23, there are no unexpected surprises.

Now that the cuts are fixed and the background model decided upon, the final selected J/ψ candidates can be checked for consistency. In particular the mass of both dimuons will be looked at, where dimuon 1 is the dimuon containing the highest p_T muon and dimuon 2 is the other. In addition to the individual dimuon masses the effect on dimuon 2 of placing a J/ψ mass window cut on dimuon 1 can also be investigated. This can all be seen in figure 6.24. The mass window used here is the normal one - 2.9 to 3.3 GeV/c^2.

Applying the J/ψ mass window to both dimuons now means that the 4μ vertex will

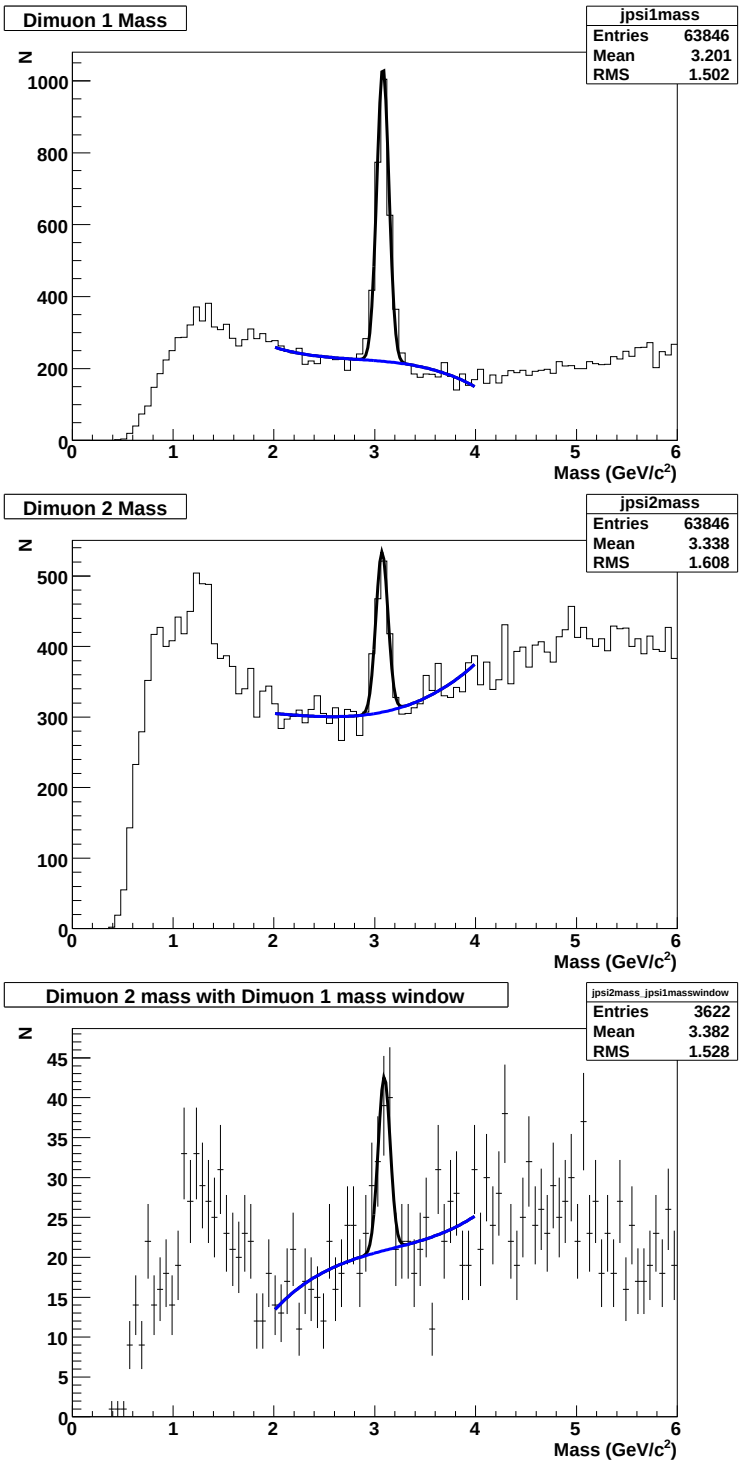

Figure 6.24: Dimuon mass plots for successful di-J/ψ events. Here are shown dimuon 1 (top), dimuon 2 (middle) and dimuon 2 after placing a J/ψ mass window cut on dimuon 1 (bottom). After J/ψ mass cuts are imposed 246 $\pm$ 16 di-J/ψ candidates remain.

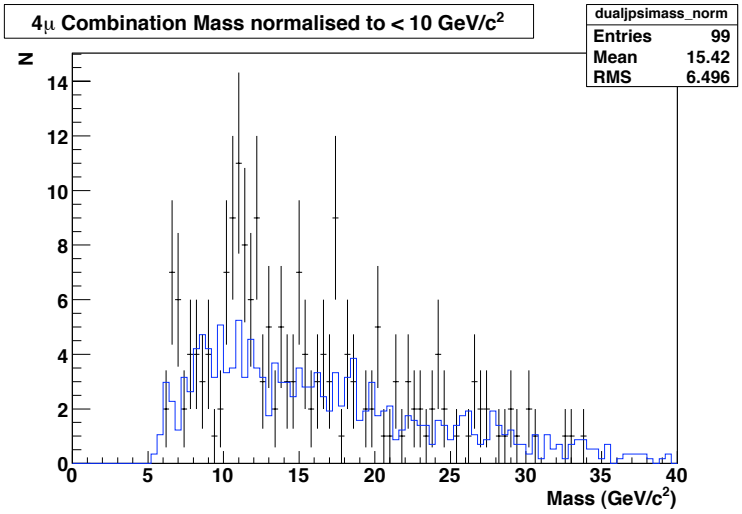

Figure 6.25: Normalized di-J/ψ mass plot for both signal (black) and sideband background (blue). Plots are normalized to the same number of candidates below 10 GeV/c^2.

become a di-J/ψ one. Combining the constituent four muons together allows for an invariant di-J/ψ mass to be found. This mass distribution can be observed in figure 6.25. Here it can be seen that there are limited statistics and that the low end of the mass spectrum has been shaped as there are very few events below 10 GeV/c^2. A much higher proportion of di-J/ψ events would be expected to be seen below 10 GeV/c^2, similar to the low end of the di-J/ψ mass spectrum seen in figure 6.1, due to the dominance of lower momentum (and thus lower energy) muons in the di-J/ψ sample.

The mass plot can be further improved through the use of a J/ψ mass constraint on each of the candidate dimuons. This constraint allows for corrections to the momentum measurements of the muons to be calculated by forcing the J/ψ mass to be that of the PDG value, 3.09692 $\pm$ 0.00001 GeV/c [7], and then finding the momentum scale factor necessary to obtain that value. This will result in four scale factors being derived, one per muon, which can then be applied to the final di-J/ψ mass and hence try to obtain a better value for the mass. This correction tries to account for slight errors in the silicon geometry, mis-measurement of p_T and Δp_T, and other similar small effects. The mass constrained plot can be seen in figure 6.26.

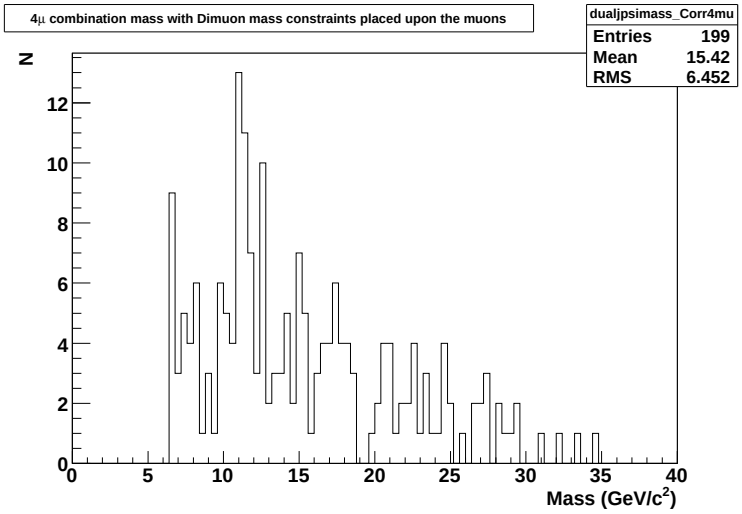

Figure 6.26: Mass constrained di-J/ψ mass for successful candidates. No background comparison present here as mass constraints fail on these background models.

6.3.7 Analysis of results

The lack of statistics is partly due to the combination of all the different cuts, as previously observed none of the cuts individually removes a high number of bad candidates. However, one of the main culprits for the low statistics was found to be the $nSMT$ cut. This cut is there to ensure that we have some silicon hits on the tracks, and hence obtain a vertex that can be well measured by the silicon detector. Unfortunately, requiring at least one silicon hit for every muon is too harsh a cut, so this will need to be relaxed and rethought.

The low statistics problem is not solely due to the $nSMT$ cut either, this cut was merely found to be the most harsh cut. Another basic cut that was found to have a large adverse effect on the total yield was the $nseg > 0$ cut. This cut was introduced to help filter out calorimeter only muons of dubious quality. However, to reintroduce these calorimeter only muons will also require careful consideration. The ideal situation here would be to pair the $nseg = 0$ muons with a good quality $nseg = 3$ muon, so as to obtain a good dimuon.

The mass shaping can be attributed to the α cut removing the low end of the mass spectrum. The mass associated to a vertex, made up of numerous tracks, is

dependent upon the angle between the tracks - the higher the mass the larger the angle generally. Hence a cut, even a small one of 10°, would have an effect on the low end of the mass spectrum. This is another cut that will need to be rethought.

6.3.8 Rethinking the di-J/ψ cuts

As previously discussed, the previous selection of cuts need to be refined. What follows are details of the investigations undertaken to improve the cuts.

The new strategy

To develop a more refined set of cuts a new way of deciding how tight a cut needs to be is required. The J/ψ was chosen initially as it is a very well known state and as such would be ideal as a basis on which to derive a set of cuts for an unknown di-J/ψ state. However, the previous results show that this strategy can lead to unforeseen problems with total yield and mass shaping, so the cut selection needs to be approached a different way.

So as to ensure that there is always a good total yield of di-J/ψ candidates, whilst still removing as many sources of poor quality tracks and muons as possible, it was decided to use the estimated number of J/ψs found in dimuon 2, after a 'good' higher p_T J/ψ_1 has already been found, as a measure of the possible yield of di-J/ψs, again blind to the di-J/ψ mass. In addition doing this allows for the signal to background ratio of the second J/ψ (after fixing J/ψ_1) to be used to ascertain the effectiveness of the cut decision on 4μ data.

Track isolation cuts

The opening angle, α, cut was designed to ensure that the final sample of di-J/ψ candidates did not contain any muons that had been matched to more than one track. This was accomplished by ensuring that there were no other matched muon tracks within a 10° cone of a particular muon. As seen in figure 6.25, this also had the unfortunate effect of shaping the low mass end of the di-J/ψ mass spectrum.

Another possible variable that would perform similarly to the opening angle is track isolation. However, since this will only allow di-J/ψ candidates whose component muon tracks are isolated from any other track (muon or otherwise), this should not shape the overall mass spectrum, but rather provide a more uniform reduction in background across the mass spectrum, which is the more desirable of two possibilities.

For this cut, an isolation cone in $dR(\eta, \phi)$ space of 0.5 is considered. The dR cone is calculated by the using the relation shown in equation 6.1 below.

$$dR = \sqrt{(\eta_1 - \eta_2)^2 + (\phi_1 - \phi_2)^2} \tag{6.1}$$

By summing over all track momenta within the $dR = 0.5$ cone, the fraction of momenta due to the muon can thus be calculated:

$$\text{Isolation} = \frac{\mathbf{p}_\mu}{\sum_{\substack{\text{Tracks in} \\ dR = 0.5 \text{ cone}}} \mathbf{p}} \tag{6.2}$$

The distribution of muon track isolation in the 4μ sample, with only the p_T and $nCFT$ muon cuts imposed, can be seen in figure 6.27. Looking at the isolation distrubtion in figure 6.27, the following isoloation cut was decided upon:

- Muon Isolation > 0.5

A comparison of the effect α and muon isolation have on dimuon 2 (with J/ψ_1 fixed) can be seen in figure 6.28. As can be seen here, whilst the isolation cut seemingly performs slightly worse than the α cut in the total di-J/ψ yield, as measured by the number of J/ψ_2s after J/ψ_1 has been found, the lack of low-end mass shaping makes the isolation cut more appropriate in this case.

The di-J/ψ mass distribution for those events which fail this muon isolation cut can be seen in figure 6.29. As can be observed in this figure, the distribution of the

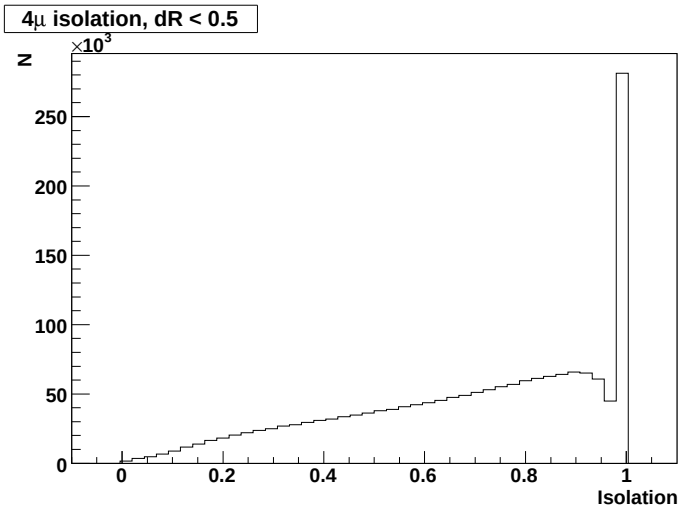

Figure 6.27: 4μ isolation distribution (using definition in equation 6.2), after applying simple muon selection cuts.

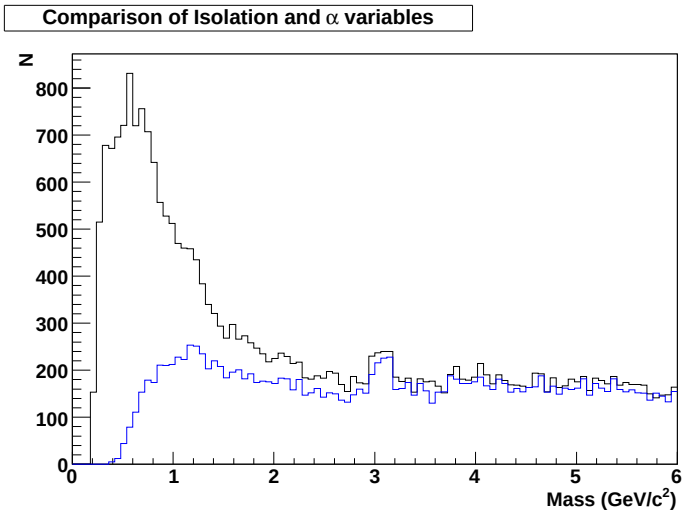

Figure 6.28: Comparison distributions between the α cut (blue) and the Isolation cut (black). The distributions used are the dimuon 2 mass after dimuon 1 has had a J/ψ mass window cut applied. The isolation cut produces 270 ± 58 J/ψs above background, and the α cut 306 ± 55 above background; additionally the isolation cut does not shape the low mass spectrum as the α cut does.

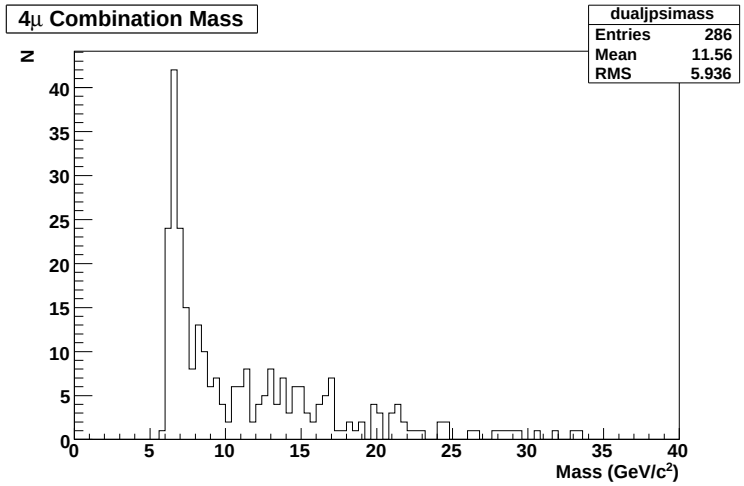

Figure 6.29: Di-J/ψ mass distribution for those candidates which fail the isolation > 0.5 cut. 390 ± 20 di-J/ψ candidates fail the isolation cut overall.

failed candidates is much more uniform than for the previously used α cut. This factor makes the isolation more suitable for distinguishing muons than the opening angle cut previously used.

Modified $nSMT$ cut

The current $nSMT$ cut is in a large-part responsible for the low di-J/ψ yield as well as helping to remove fake tracks, and as such a more refined cut is needed instead. The $nSMT$ requirement that every muon have at least one SMT hit was to help ensure that the final sample of di-J/ψ candidates has good quality vertices. After careful consideration it was decided to reduce this cut to require only one muon in each dimuon pair to pass the $nSMT$ requirement. That is explicitly:

- At least one muon in each dimuon must have $nSMT > 1$

This loosened cut can be made as the high muon quality requirements, that is $nseg$ cuts, will help to ensure that the vertices contain good muons, thus the $nSMT$ requirement can be relaxed. Comparison of the old and new $nSMT$ requirements can be seen in figure 6.30. Here the mass spectrum of dimuon 2, with a fixed J/ψ_1, is plotted in each case. The new $nSMT$ cut is seen here to produce a greater yield

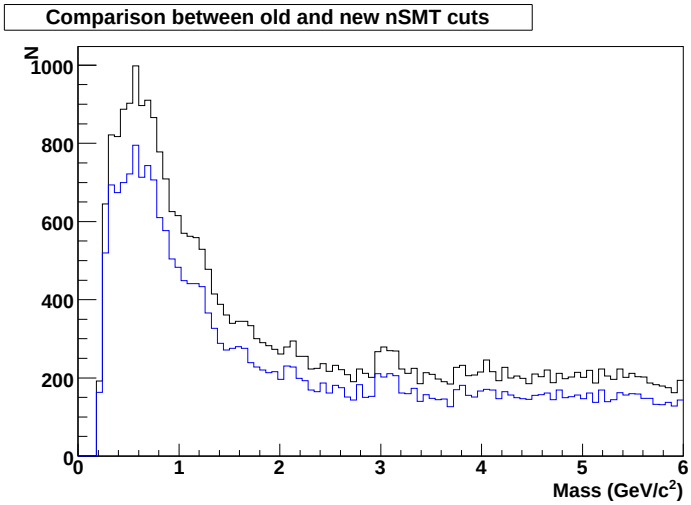

Figure 6.30: Comparison distributions between the old $nSMT$ cut (blue) and the new cut (black). The distributions used are the dimuon 2 mass after dimuon 1 has had a J/ψ mass window cut applied. The old cut produces 223 ± 55 J/ψs above background, and the new cut 285 ± 58 above background.

of di-J/ψs than the old cut. A plot of the failed di-J/ψ candidates when considering this new $nSMT$ requirement can be seen in figure 6.31.

Modified muon $nseg$ requirements

The other cut that was found to be most responsible for the low di-J/ψ yield observed was the muon $nseg$ requirement. The requirement was that all muons must have at least one hit somewhere in the muon system, that is:

- Muon $nseg > 0$

That is, no calorimeter muons. As previously mentioned, this was found to be too restrictive and so a way to include these calorimeter-only muons is needed. Since these $nseg = 0$ muons are of potentially dubious quality, they should ideally be paired with a muon of good quality, that is $nseg = 3$. In addition, some extra identification criteria, using the calorimeter, are required to ensure that the energy deposits left there most likely come from a low momentum muon and are described in detail in [85].

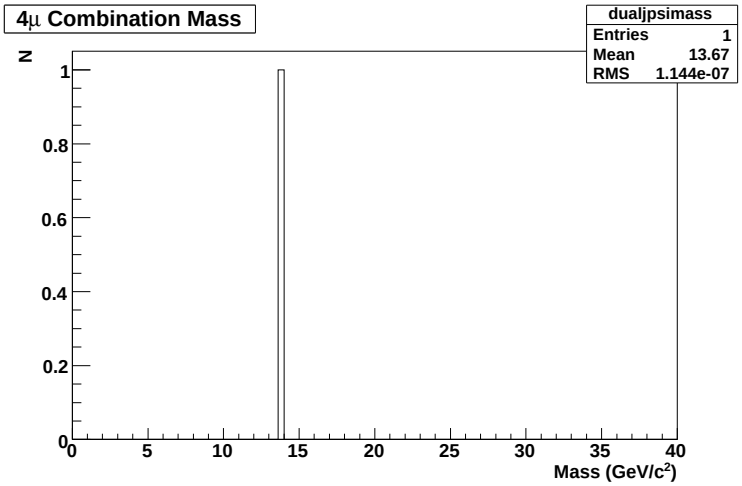

Figure 6.31: Di-J/ψ mass distribution for those candidates which fail the new $nSMT$ cut, ≥ 1 muon per dimuon must have $nSMT > 0$. 1 ± 1 di-J/ψ candidates fail the new $nSMT$ cut overall.

The yield provided by these refined cuts can further be increased by accounting for the 'hole' in the bottom of the muon system. The bottom of the DØ detector contains only two layers of muon detectors, instead of the usual three. This means that the muon acceptance is lower in this region, and hence the efficiency of the previous cut is impaired. To remedy this, the $nseg$ requirement on the dimuon is lowered from one $nseg = 3$ muon to one $nseg = 2$ muon in the central region of the detector, that is $|\eta| < 1.0$. Elsewhere the requirement is still $nseg = 3$.

The comparison of the old and new $nseg$ requirements can be seen in figure 6.32. In this figure the yields of di-J/ψ are estimated from the dimuon 2 with a fixed J/ψ_1. A plot of those di-J/ψ candidates which fail these new $nseg$ requirements can be seen in figure 6.33.

6.3.9 Background models

Now that the cuts are finalized, the three possible background models previously described can be examined, deriving them in the same way.

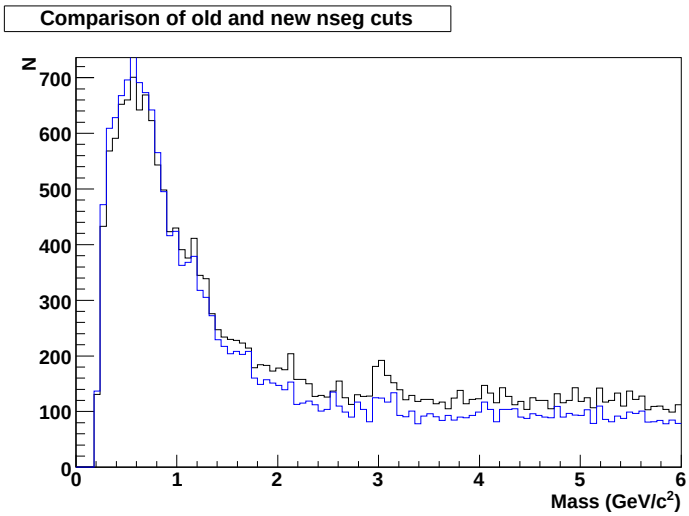

Figure 6.32: Comparison distributions between the old (blue) and new (black) *nseg* cuts. The distributions used are the dimuon 2 mass after dimuon 1 has had a J/ψ mass window cut applied. The old *nseg* cut produces 111 ± 43 J/ψs above background, whilst the new cut produces 226 ± 49 above background.

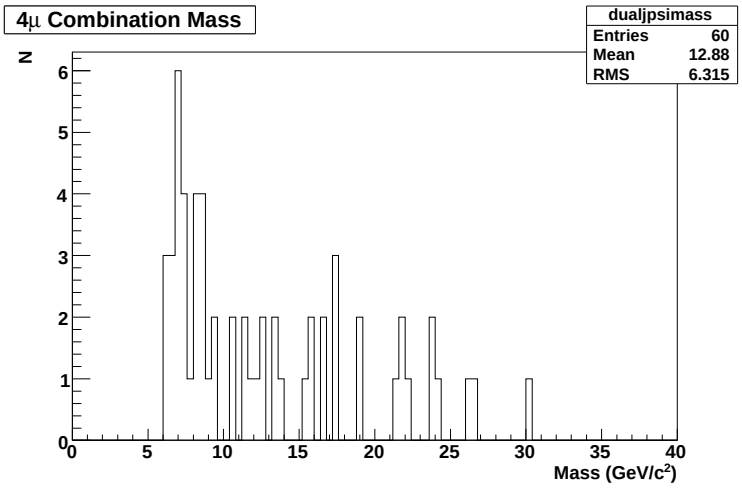

Figure 6.33: Di-J/ψ mass distribution for those candidates which fail the new region dependent *nseg* cuts. 75 ± 9 di-J/ψ candidates fail the new *nseg* cuts overall.

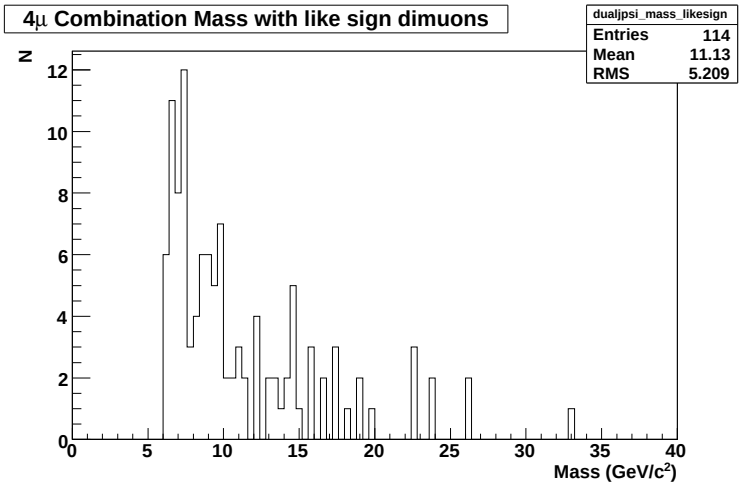

Figure 6.34: Like sign dimuon background for the new set of cuts.

Same sign background

The 4μ mass distribution, whilst requiring same sign muons in each dimuon, can be seen in figure 6.34. Once again the same sign background suffers from a lack of statistics, although this is somewhat offset by the new cuts. The mass distribution looks similar to that seen using the previous cuts, figure 6.18. The low statistics of this particular background model, however, make it unsuitable for use in this particular case.

Sideband background

Using the same sideband definitions as previously, a plot similar to that shown in figure 6.20 can be created for the new cuts. This is shown in figure 6.35. As before, the 4μ yield in this sample is much more favourable than using the same sign background. Also, as previously, the sample tends to prefer the low mass end of the spectrum, again due to the larger number of low mass dimuons over higher mass dimuons in the sample.

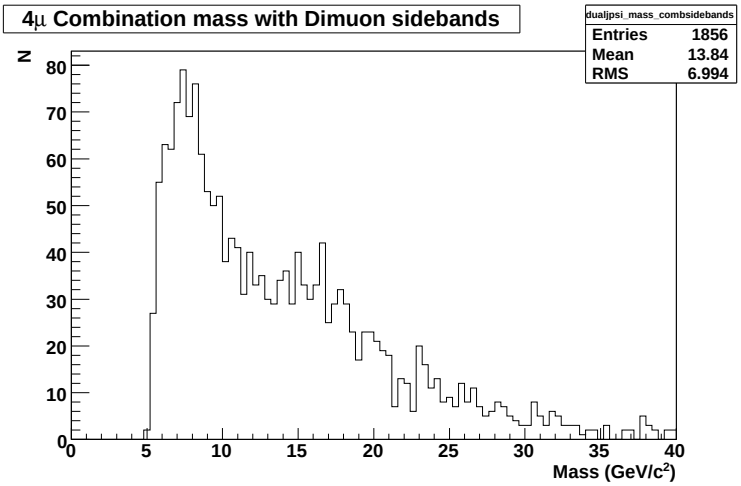

Figure 6.35: J/ψ sideband background for the new cuts. The distribution is comparable to that shown in figure 6.20, but with a bigger background yield.

Mixed event background

Simarly, the mixed event background for the new cuts can be also be calculated using the previously described method. This result can be seen in figure 6.36. The background mass distribution is similar to figure 6.22, but the newer set of cuts also provides greater statistics - to be expected given the looser cuts, and trends in the other background models.

6.3.10 Results

Once again, the sideband background is chosen as the background model. This is due to its good background description and the high statistics it provides. The sideband background will also use the same background normalisation as before. This allows for a good comparison of the di-J/ψ candidates which pass the cuts and the background model.

The same checks for the di-J/ψ kinematics and J/ψ distributions can now be redone for the new cuts. The di-J/ψ kinematics, p_T, η, ϕ and vertex χ^2, are shown in figure 6.37. All four of the basic kinematic plots are as to be expected.

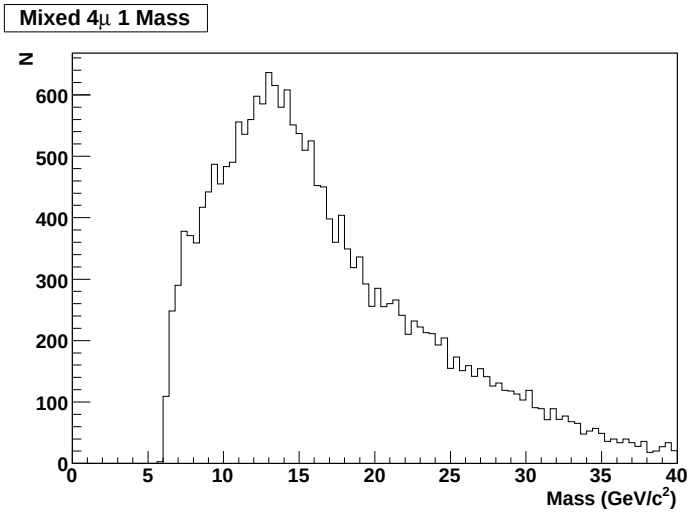

Figure 6.36: Mixed event background for the new cut set. This distribution can be compared to the mixed event background for the previous cuts shown in figure 6.22.

The J/ψ mass distributions can be seen in figure 6.38. The three plots are the two dimuon masses, with all cuts imposed, and the mass spectrum of dimuon 2 with J/ψ_1 mass window restrictions imposed. As usual, the mass window is located around the PDG measured J/ψ mass, 2.9 to 3.3 GeV/c^2.

By applying the same J/ψ mass window restrictions to both dimuons, a di-J/ψ candidate is obtained. By then combining the four muons together, a di-J/ψ vertex can be found, and hence a di-J/ψ mass calculated. This mass distribution can be observed in figure 6.39. Compared to the previous cuts, shown in figure 6.25, it can be seen that the new cuts provide greater statistics and also compensate for the shaping of the low-end mass spectrum previously observed.

As before, J/ψ mass constraints can also be applied to those dimuons which lie within the predefined J/ψ mass window. This process can allow for better mass resolution on the di-J/ψ vertex as the momentum corrections applied to the individual muons, arising from forcing the dimuons to have the measured J/ψ mass, help reduce the momentum uncertainty. The result of this can be seen in figure 6.40, and can be compared to the previous cuts shown in figure 6.26.

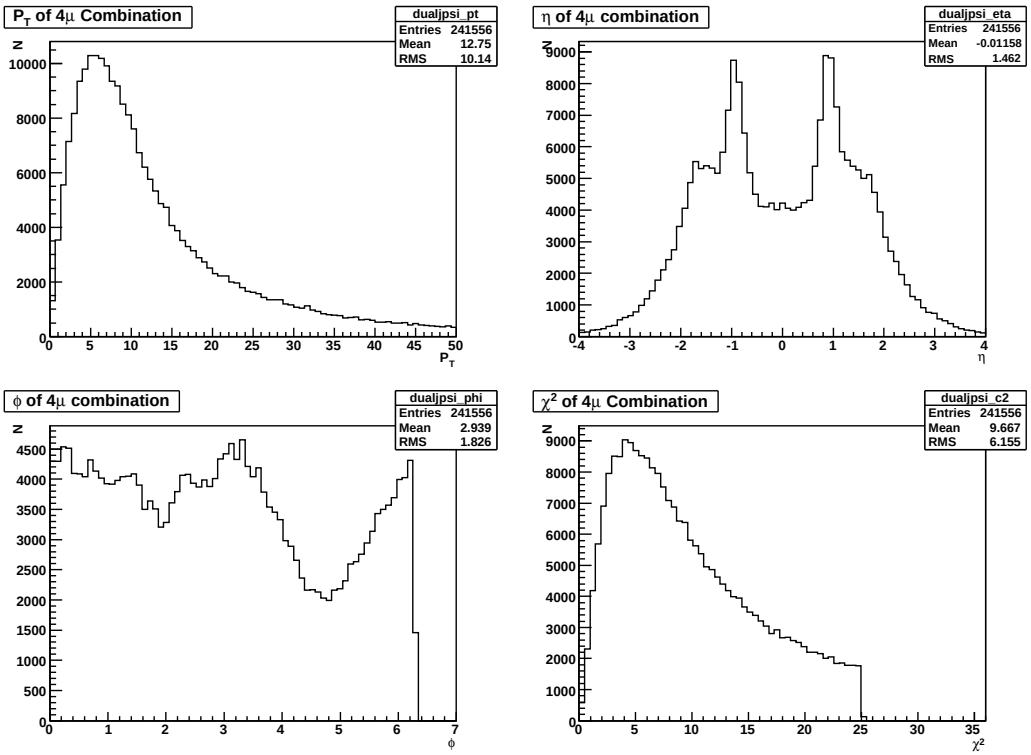

Figure 6.37: Kinematical plots for the di-J/ψ candidates produced using the new cuts. From the top left, these plots are di-J/ψ p_T, di-J/ψ η, di-J/ψ ϕ and di-J/ψ χ^2. The peaks in η around $\eta = \pm 1$ are due to the reduced coverage of the calorimeter in this region allowing a greater number of muons to pass through to the muon system (and in particular lower momentum muons). The dip in ϕ between 3.5 and 5.5 is due to the reduced PDT coverage at the bottom of the detector to make way for structural supports. Both of these effects are observed in each of the individual muon kinematic plots too, and after combination of the four muons to create the 4μ state the effects are still present.

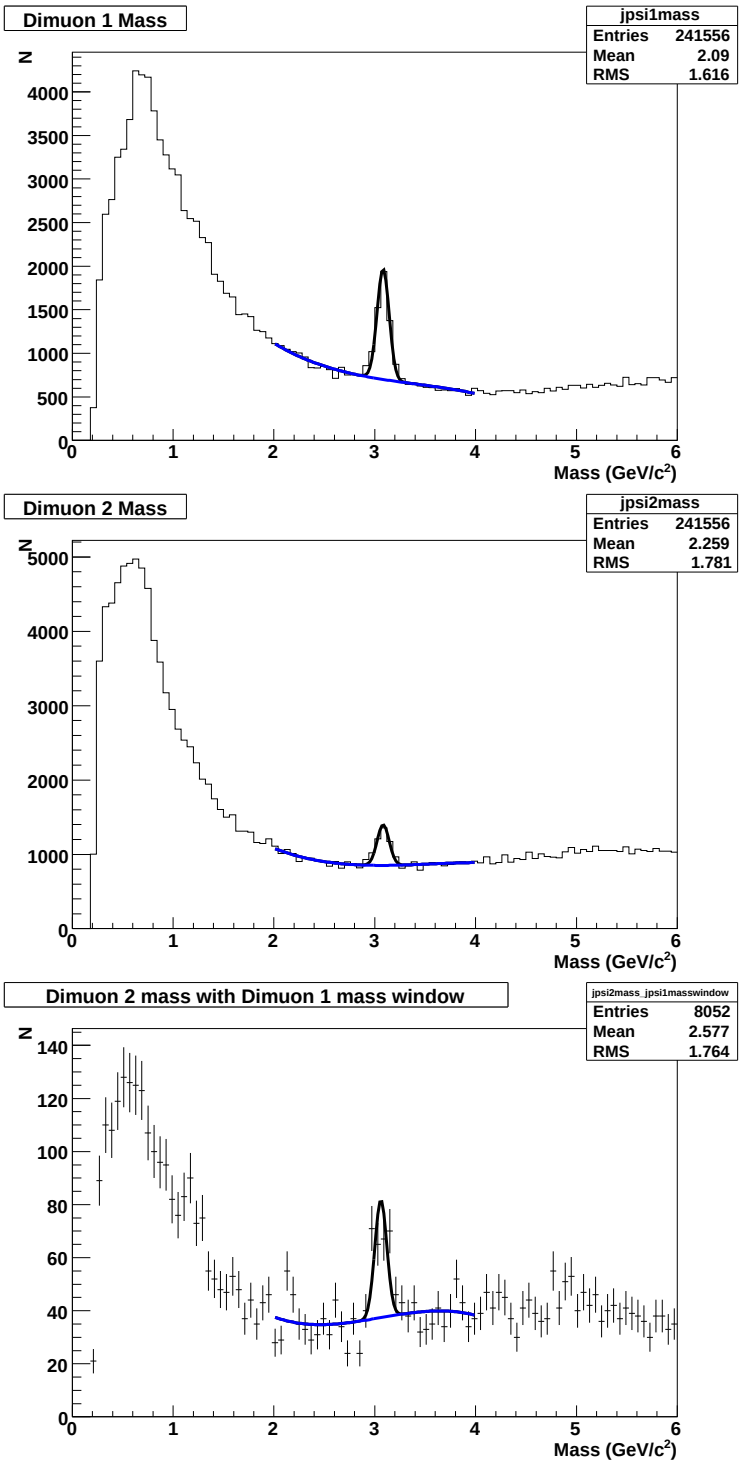

Figure 6.38: Dimuon mass plots for successful di-J/ψ events using the new set of cuts. Here are shown dimuon 1 (top), dimuon 2 (middle) and dimuon 2 after placing a J/ψ mass window cut on dimuon 1 (bottom). After J/ψ mass cuts are imposed 464 ± 22 di-J/ψ candidates remain.

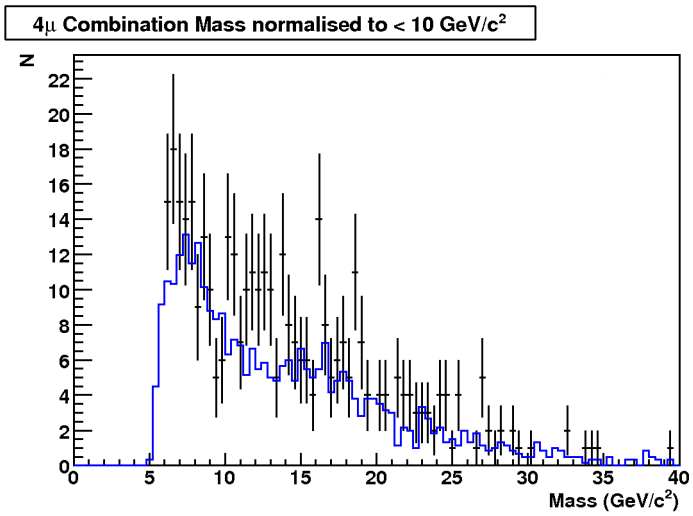

Figure 6.39: Normalized di-J/ψ mass plot for both signal (black) and sideband background (blue). Plots are normalized to the same number of candidates below 10 GeV/c^2. These plots were produced using the new cuts.

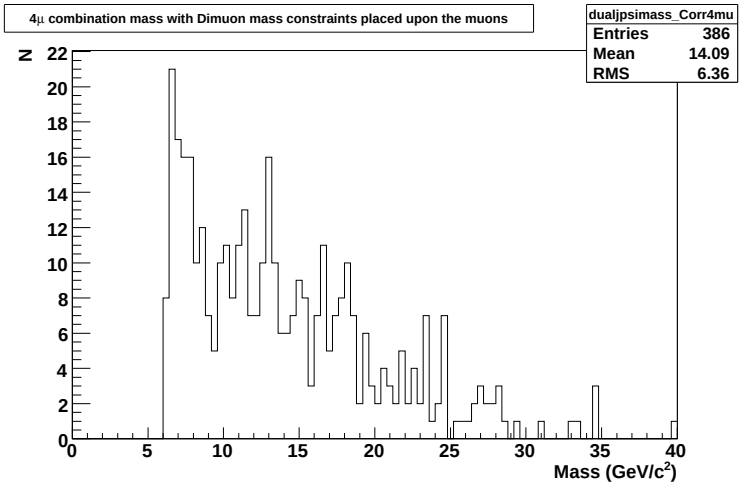

Figure 6.40: Mass constrained di-J/ψ mass for successful candidates using the new set of cuts. No background comparison present here as mass constraints fail on the sideband background model.

6.3.11 Analysis of results

The new choice of cuts appears to have much improved the total di-J/ψ yield, and the removal of the α cut has seemingly also reduced the shaping of the mass spectrum below 10 GeV/c^2. The final number of di-J/ψ candidates is simply calculated from the number of di-J/ψ candidates which pass the cuts. In addition to this, signal to background estimates of J/ψ_2 production given a previously found J/ψ_1, as estimated from the dimuon 2 with J/ψ_1 mass window imposed plot, can provide an estimate of the signal to background for the di-J/ψ candidates, that is the number of di-J/ψs that are from two J/ψs rather than a J/ψ and background dimuon, or even two background dimuons. Fits to the J/ψ resonance in the dimuon mass spectrum allow for the number of signal and background events to be estimated.

This information is shown in table 6.2. In this table the two cut selections are compared for the total di-J/ψ yield and also the signal to background estimates previously described. The new cuts perform much better than the old ones, particularly in terms of di-J/ψ yield. In addition the signal to background estimate for the new set of cuts is much improved.

	'Old' cuts	'New' cuts	Original analysis cuts
4μ yield	63846 ± 253	241556 ± 490	806663 ± 900
Di-J/ψ yield	246 ± 16	464 ± 22	926 ± 30
Signal to background estimate	3.8 ± 1.9	5.9 ± 2.4	6.0 ± 2.4

Table 6.2: Table showing the 4μ and di-J/ψ yields and signal to background estimates for the two different sets of cuts, and the original analysis. The 4μ yield is taken from the number of candidates which pass all cuts whilst the di-J/ψ yield is the number of candidates remaining after J/ψ mass windows are imposed. The signal to background estimate (found from the formula $S/\sqrt{S+B}$, where S is the signal estimate and B is the background estimate) is taken from the the number of J/ψ_2s once J/ψ_1 has been previously found. Fits to signal and background on the J/ψ resonance peak allow for this number to be estimated.

The numbers given in table 6.2 are valid for di-J/ψ mass plots with and without the J/ψ mass constraint, as the mass constraint is only applied once the candidate passes the original J/ψ mass window.

Given all these factors, especially the greater di-J/ψ yield, the new, more refined, cuts have been shown to be a better choice than the previous cuts. These cuts can now be compared to those used in the original analysis.

6.3.12 Comparison with the previous analysis

Now that a suitable set of cuts have been decided upon, they can be compared to the original analysis and original cuts to see whether there are any changes in the di-J/ψ mass distribution and whether the previously observed excess in the di-J/ψ spectrum is confirmed or not. This will be done by taking the original cuts and then using them in this analysis and then comparing the results with both the original plot (figure 6.1) and the mass distributions for the final set of cuts as shown in figures 6.39 and 6.40, without and with the J/ψ mass constraints respectively.

The original analysis used the following cuts on the muons, dimuons and 4μ states:

- Track $p_T > 1$ GeV/c
- Track $p_T > 1.5$ GeV/c if muon $nseg > 0$
- $nCFT > 0$
- At least one $nseg = 3$ muon in each dimuon
- 4μ vertex $\chi^2 < 36$
- Lifetime significance, $\frac{L_{xy}}{\sigma_{Lxy}} < 5$

The $nseg = 0$ muons use the same definitions to define the calorimeter only muons as described in the section above. The lifetime significance is defined as being the lifetime in the transverse plane, L_{xy}, divided by the error on that lifetime, σ_{Lxy}, and is there to ensure that the final sample contains di-J/ψ candidates that come from short lived parent particles - the equivalent in the analysis described above is the impact parameter < 0.1 cm cut. The same J/ψ mass window as used in the author's analyses, 2.9 to 3.3 GeV/c^2, will be used to create all the following plots for consistency.

Using these cuts the usual array of plots can be constructed. Figure 6.41 shows the kinematic variables and vertex χ^2 for those di-J/ψ candidates which pass both the

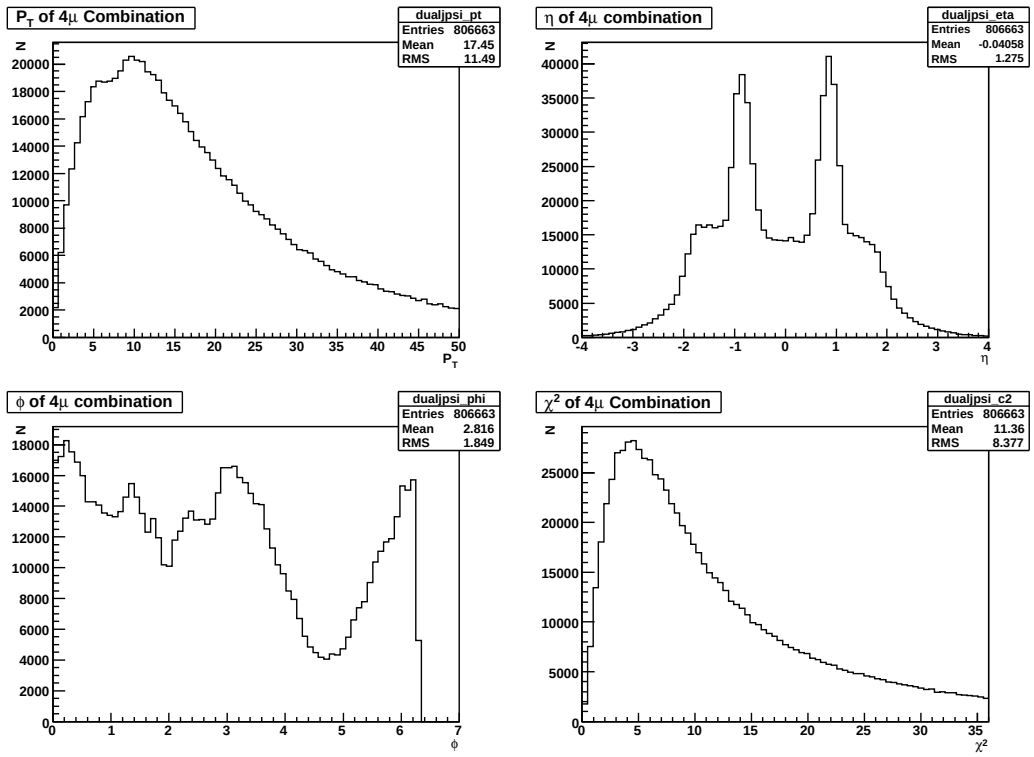

Figure 6.41: Kinematical plots for the di-J/ψ candidates produced using the cuts from the original analysis. From the top left, these plots are di-J/ψ p_T, di-J/ψ η, di-J/ψ ϕ and di-J/ψ χ^2. The peaks in η around $\eta = \pm 1$ are due to the reduced coverage of the calorimeter in this region allowing a greater number of muons to pass through to the muon system (and in particular lower momentum muons). The dip in ϕ between 3.5 and 5.5 is due to the reduced PDT coverage at the bottom of the detector to make way for structural supports. Both of these effects are observed in each of the individual muon kinematic plots too, and after combination of the four muons to create the 4μ state the effects are still present.

cuts and J/ψ mass windows. Similarly, figure 6.42 shows the dimuon mass distributions for those di-J/ψ candidates which pass the cuts. None of the distributions shown in these two figures reveal any anomalies, or unexpected features.

Finally, the di-J/ψ mass distribution for the original analysis' cuts can be created and compared to the sideband background for those cuts (as used in the original analysis), and can be seen in figure 6.43. A possible signal excess at 13.7 GeV/c^2, compared to the sideband background estimation, can be seen in figure 6.43, but there are also further possible excesses at higher di-J/ψ masses. Fitting the signal, S, at 13.7 GeV/c^2 with a Gaussian and using a 1st order polynomial to fit the background, B, an estimation of the signal significance can be made using the relationship $S/\sqrt{S+B}$ as in the original analysis. This fit can be seen in figure 6.44.

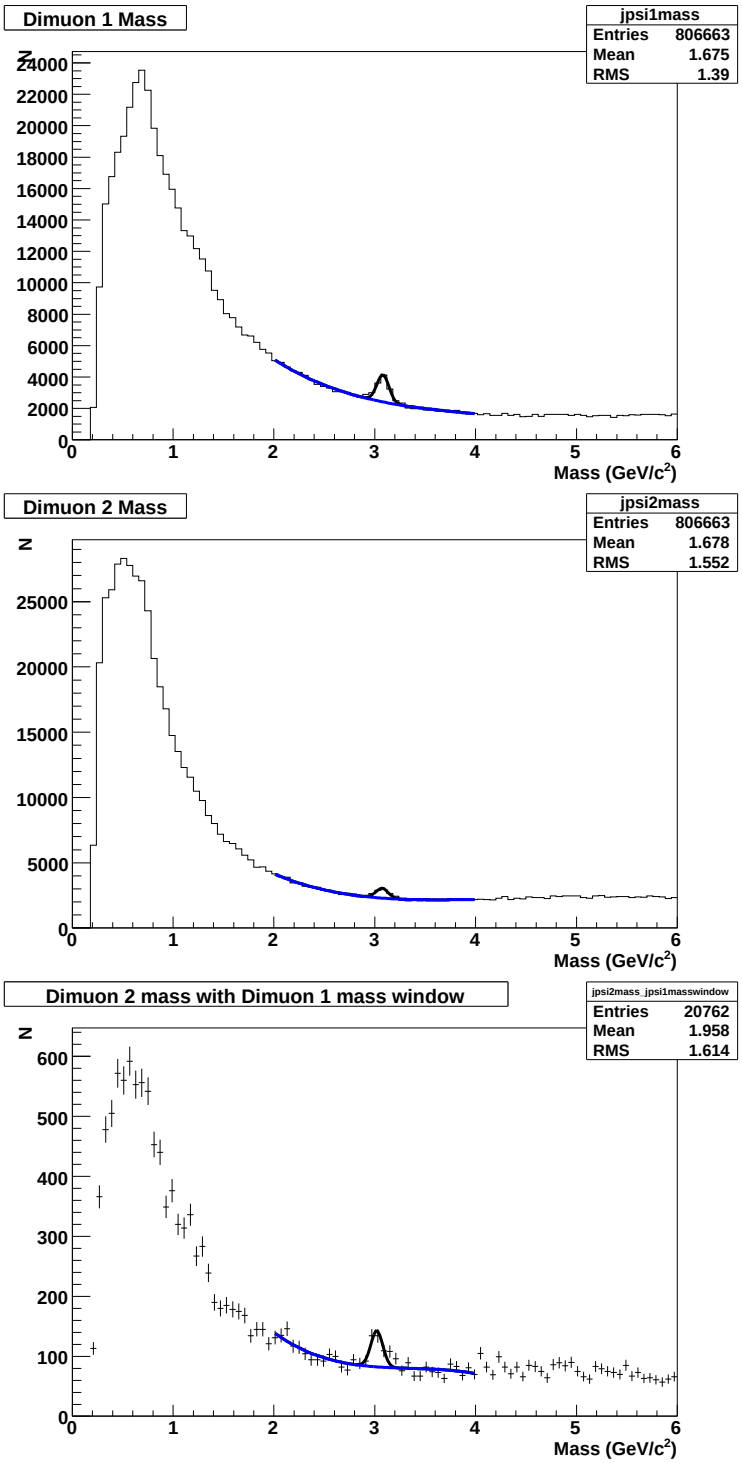

Figure 6.42: Dimuon mass plots for successful di-J/ψ events using the cuts from the original analysis. Here are shown dimuon 1 (top), dimuon 2 (middle) and dimuon 2 after placing a J/ψ mass window cut on dimuon 1 (bottom). After J/ψ mass cuts are imposed 926 $\pm$ 30 di-J/ψ candidates remain.

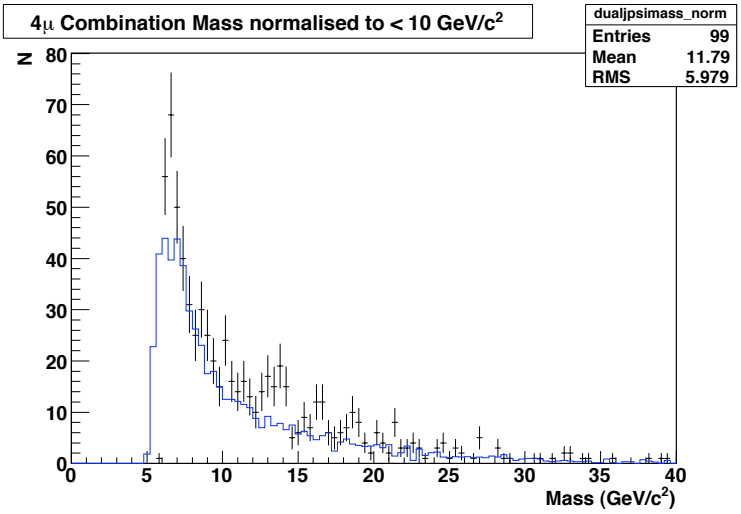

Figure 6.43: Normalized di-J/ψ mass plot for both signal (black) and sideband background (blue). Plots are normalized to the same number of candidates below 10 GeV/c^2. These plots were produced using the original analysis' cuts.

Calculating the significance leads to the result that the signal significance is 1.6σ.

A comparison of the author's final choice of cuts to the original analysis can be seen in figure 6.45. In this figure it can be seen that the finalised cuts from both analyses produce similar mass distributions, however the original analysis produces a higher yield of di-J/ψs, but due to fewer quality cuts being imposed the quality of the di-J/ψs can be questioned. Compared to the plot shown in figure 6.1, this distribution looks similar, but without the clear excess around 13.7 GeV/c^2 seen in the first analysis. The di-J/ψ yield and signal to background estimates for the original analysis' cuts are shown in table 6.2.

The optimized cuts reveal no excess where the original analysis observed one [76], whilst reusing the original cuts on a larger data set (2.8 fb^{-1} versus 1 fb^{-1}) results in much reduced signal significance around the excess at 13.7 GeV/c^2. Although the low mass region of the two sets of cuts shown in figure 6.45, the author's optimized cuts and the original cuts used, is different between the different analyses, likely due to a combination of the isolation and ΔR_A cuts, the higher mass ranges (>10 GeV/c^2) are the same within errors, with the exception of the slight excess at 13.7 GeV/c^2. some of the remaining excess seen in figure 6.43 could be explained by the lack of a ΔR_A cut.

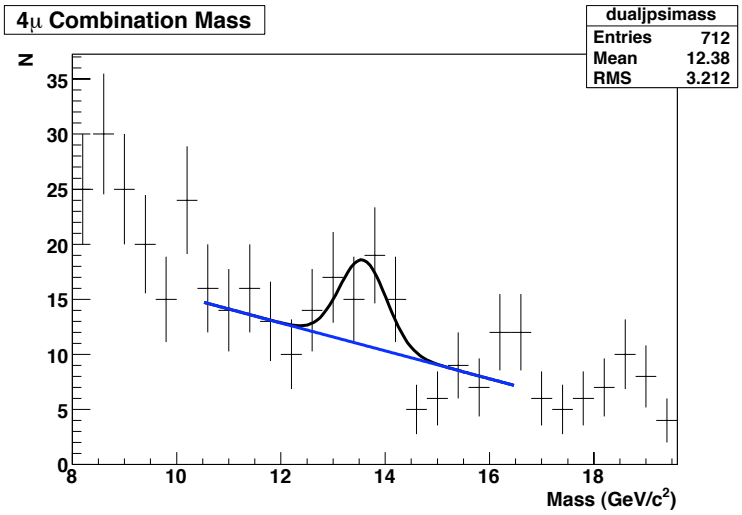

Figure 6.44: Fit to the excess around 13.7 GeV/c^2 in the di-J/ψ mass range. The signal is in black and the linear background fit in blue. Excess significance calculated to be 1.6σ.

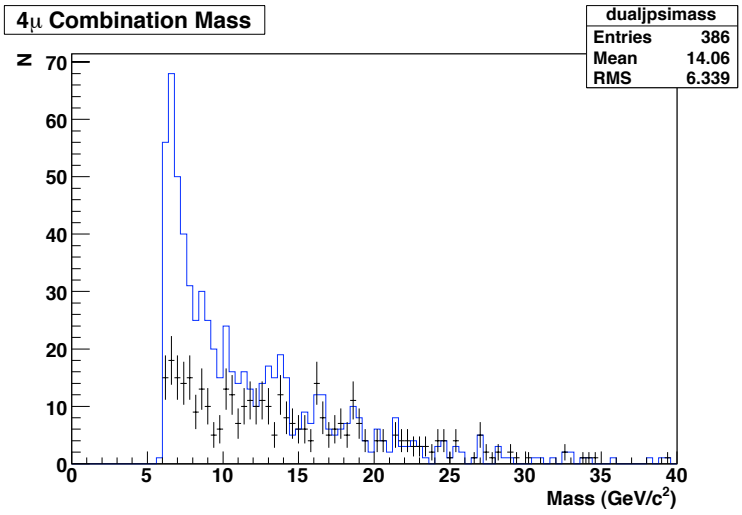

Figure 6.45: Comparison of the original analysis (blue) and the optimized set of cuts (black) with a di-J/ψ mass applied. The original analysis has a better yield of di-J/ψ candidates, however, no evidence of an excess is seen in either plot.

Figure 6.17 shows the di-J/ψ mass plot for those events which fail the $\Delta R_A > 10$ cm cut, and in this plot it can be seen that there is a significant number of di-J/ψ candidates that lie around the 13.7 GeV/c^2 mass range. This could indicate that part of the original excess could be due to charge sharing between PDTs in the muon system, whereby the charge deposited by one charged particle would be spread amongst two PDTs, both of which are reconstructed as individual muons. Another possible reason for the excess could be the older p14 version of the reconstruction software, d0reco, used for part of the 1 fb^{-1} data set in the original analysis. The earlier version of the software does not have the better quality calibrations and algorithms used in d0reco versions p17 and p20, especially in relation to the improved primary vertexing routines included in p17 and above, and so this could result in differences in the overall mass distributions.

6.3.13 Conclusions

This chapter has demonstrated two new sets of cuts that can be used, and have been used, as the basis to test a previous di-J/ψ analysis. The new cuts involve the use of both track and muon quality cuts that were not present in the previous analysis, as well as extra cuts to discern that the final di-J/ψ sample contains distinct tracks and muons. These cuts are imposed to try to remove all possible reasons for the previously seen excess, including detector effects, mis-reconstruction of muons and tracks and mis-identification of muons.

Figure 6.39 shows the di-J/ψ mass distribution for the set of cuts that were deemed most usuable for this analysis. These cuts can be compared to both the original analysis itself, shown in figure 6.1, and a reproduction of the original analysis using those cuts with the fuller dataset, shown in 6.43. With a larger data set, the signal excess is observed to shrink from $>5\sigma$ to 1.6σ when the cuts are reproduced. Combined with the optimized cuts derived by the author, the validity of the original observed signal excess is brought into doubt.

The work done here can be used in further studies into low momentum multi-muon studies, in particular for studies into di-J/ψ production cross sections, where the

cross section is dependent upon the p_T of the di-J/ψ and the fragmentation model in use (color singlet or color octet models). To do so, a calculation of the production cross-section will need to be made for a range of p_T values, divided into bins of different widths to ensure enough statistics in each bin to calculate a cross-section, in order to obtain the desired di-J/ψ cross-section versus p_T distribution. To make the cross-section calculation detailed efficiency studies would need to be conducted, for example measuring triggering and detector efficiencies and the di-J/ψ reconstruction efficiency, as well as the total luminosity of the sample calculated. With these values, and knowledge of the number of di-J/ψ events in the various p_T bins available, a cross-section can be found, and hence the di-J/ψ cross-section versus p_T distribution be obtained. This can then be compared to theory predictions and a final result be derived.

Even though the cuts were derived using J/ψ states and di-J/ψ analyses, they should be valid for any dimuon state and any 4μ state, in particular the cuts used to prevent mis-identification of muons. Some of the cut studies used here can also be used for high momentum multi-muon studies too, for example in new phenomena studies where dimuon production is increased through the introduction of beyond the Standard Model physics.

Chapter 7

Conclusions

7.1 Summary

There are many questions remaining in High Energy Physics, and new questions are being raised all the time, not least of all from the observation of resonance structures in a given distribution that are not predicted by theory. The recent measurement of B_s mixing by the DØ [1] and CDF [2] experiments is one of the questions that experimental evidence has been able to answer, and DØ is working to confirm that result. Analysis of the different charmonium states, and the J/ψ in particular, has allowed for the discovery of both the c and b quarks as well as the discovery of a myriad other particles. Analysis of the di-J/ψ state allows for scientists to both test theories of fragmentation, the color singlet or color octet models, and to search for new particles and states.

However, to find answers to these questions, or to test the validity of existing answers, excellent analysis equipment is required and in the field of High Energy Physics this means a well-performing accelerator and detector, and in this case it is the Tevatron accelerator and DØ detector. Both the Tevatron and DØ have been performing well, with the Tevatron delivering ~ 50 pb^{-1} a week and peak luminosities of $> 3\text{x}10^{32}$ cm^{-2}s^{-1} regularly. DØ is recording data with an efficiency of over 90%. One of the most important parts of the DØ detector is the data acquisition

and triggering system. Fast and efficient algorithms run at all triggering levels are key to being able to both collecting quality data relevant to physics analysis and to maintaining the high level of data recording efficiency.

Studies conducted on the p16 release of the Level 3 triggering software in order to reduce the time taken for the Level 3 tracking software to run. These studies included the production and testing of a trimmed dead fibre file, designed to improve tracking efficiency by accounting for dead fibres within the CFT, as a compromise between the efficiency gain the file provided and the large increase in processing time that came with it. The final decision was made to run the Level 3 tracking algorithms without any dead fibre file present. The p16 studies also involved investigations into the dependence of the z and $x-y$ vertexing tools upon the minimum p_T of the tracks used as input to the vertexers. It was found that whilst both vertexers displayed a loss in vertex finding efficiency as the minimum p_T was raised, the efficiency drop was much more severe for the $x-y$ vertexer than the z vertexer. As such filters which use the z vertexer alone had the minimum track p_T raised to 3 GeV/c, and filters which required the $x-y$ vertexer used the default p_T cut of 0.5 GeV/c. Both of these studies helped to reduce the time taken by Level 3 on average per event.

The p17 release of the Level 3 software required full testing and certification before it could be placed onto the Level 3 farms. Tracking improvements in p17 included improvements to the SMT algorithm in the Level 3 tracking software and improvements to the SMT unpacker itself. These resulted in a tracking efficiency improvement of $\sim$10%. Further studies into tracking and vertexing dependence upon both the track p_T cut and luminosity revealed both reduced tracking time and efficiencies for increasing luminosity and p_T cut, whilst the z vertexer was shown to improve in efficiency with increased luminosity, but decrease with p_T cut and the $x-y$ vertexer's efficiency decreased with both increasing luminosity and p_T cut.

The p17 Level 3 software ran online until the end of Run IIa in February 2006 when the Run IIb upgrade took place. One of the many upgrades undertaken was the replacement of the Run IIa tracking software with new optimized Run IIb tracking algorithms, `L3TCFTTrack`, that would better cope with the increasing luminosity

being delivered by the Tevatron. The new Level 3 tracking software provides both an improvement to tracking efficiency of about 10% and a reduction in processing time of about 15% compared to the Run IIa tracking software for the same data sample. The $x-y$ vertexing algorithm requires both excellent track and track error information with which to perform its calculations. As such a new set of track errors were derived by parameterizing them in terms of p_{scat} and the number of SMT hits associated to a track (figure 4.4 and table 4.2). These new errors helped to improve the vertex resolution in Monte Carlo by $\sim$0.5 μm compared to incorrect errors, and increase the mean number of tracks associated to the vertex by $\sim$0.5.

The Run IIb upgrade also saw the installation of a new silicon sub-detector, Layer 0, within the existing SMT. The inclusion of Layer 0 readout into the existing Level 3 SMT unpacking software, `L3TSMTUnpack`, and its subsequent use by the Level 3 Run IIb tracking software in its SMT tracking algorithms, has resulted in vastly improved overall track DCA resolutions ($\sim$50% improvement). After retuning the DCA errors (figure 5.11 and table 5.2), due to the inclusion of Layer 0, it was found that vertex resolutions improved by $\sim$4.5 μm on average and the mean number of associated tracks increased by 1.52 in the data sample. Improvements in both the vertex resolution and the mean number of associated tracks were also observed in the Monte Carlo sample.

An initial study into the di-J/ψ channel revealed an anomalous peak in the di-J/ψ mass spectrum at $\sim$13.7 GeV/c^2 (figure 6.1) which had a significance $> 5\sigma$ [76], and a confirmation study was performed to verify the anomalous peak. An initial set of cuts were derived using studies of J/ψs whilst remaining blind to the final di-J/ψ mass. However, these cuts were found to be too harsh and, in the case of the opening angle, α, cut, shaping the lower end of the mass spectrum when applied to the di-J/ψ system (figure 6.25), and so an alternative set of cuts were required. These new cuts were derived by investigating the signal to background and total yields of the di-J/ψ system, whilst still remaining blind to the final mass. Comparison of the di-J/ψ mass spectrum to the sideband background, using 2.8 fb^{-1} of data, revealed no significant excess around 13.7 GeV/c^2 (figure 6.39). Replicating the cuts from the original analysis on the new larger data set saw a reduction in the significance

of the excess around 13.7 GeV/c^2 to 1.6σ (figure 6.43) and comparison between the author's optimized cuts and the cuts from the original analysis reveals no clear excess around the anomalous resonance in the spectrum (figure 6.45).

The work described in this thesis has contributed significantly to the physics output of the DØ experiment, both in terms of developments and improvements made to the online triggering system and analysis of data collected by the detector.

7.2 Future work

The Layer 0 modifications made to the Level 3 SMT unpacker, and the associated DCA errors, have been used to collect over 3 fb^{-1} of high quality data to date. There are currently no plans to further modify any of the core Level 3 tracking code and as such this means the Layer 0 modifications will be online until the end of Run II. Whilst new SMT pedestal parameterizations may be undertaken and dead HDIs brought back into (or taken out of) the SMT readout, the Layer 0 changes made to the unpacking code is independent of these changes. Should any major modifications be made to the Run IIb tracking software, however, there exists the possibility that new DCA errors will need to be derived, especially if modifications are made to the SMT tracking algorithms, but as previously stated there are currently no plans to further change the Level 3 tracking software.

The author's optimized cuts derived for the di-J/ψ confirmation analysis reveal no significant excess in the di-J/ψ mass spectrum. Although no unpredicted di-J/ψ resonance was observed, the cuts derived here can easily be used in searches for other di-J/ψ resonance states, for example $\eta_b \rightarrow J/\psi J/\psi$. In addition the first set of cuts derived using J/ψ states could be easily transferred over to any search analysis which was using a J/ψ decay product as one of the search states. However the cut design philosophy used here was based around a need to eliminate all possible sources of track and muon contamination from the data, so whilst this is advantageous to any search analysis, some of the cuts may need refining first, for example the cuts eliminating the muon 'spikes' in $\eta - \phi$ could be relaxed slightly, or the isolation

cut further refined to perform the same function as it currently does whilst also improving the yield.

The aim of the original di-J/ψ analysis was to derive the di-J/ψ production cross-section as a function of p_T, and thus discern whether the di-J/ψ production was through the color singlet or color octet mechanisms (figure 1.10). As such a logical progression of the work described here is to use the di-J/ψ sample produced to derive a di-J/ψ cross-section for different ranges of p_T. To do so, detailed efficiency studies would need to be conducted, for example measuring triggering and cut efficiencies, as well as the total luminosity of the sample calculated. The question of which mechanism is used for $c\bar{c}$ production is still important and hotly debated and can hopefully be answered at either the Tevatron or at the LHC [86].

References

[1] V. M. Abazov *et al.*, "First direct two-sided bound on the B_s^0 oscillation frequency," *Phys. Rev. Lett.* **97** (2006) 021802, `hep-ex/0603029`.

[2] A. Abulencia *et al.*, "Observation of $B_s^0 - \overline{B_s^0}$ oscillations," *Phys. Rev. Lett.* **97** (2006) 242003, `hep-ex/0609040`.

[3] D. Griffiths, "Introduction to Elementary Particles,". John Wiley & Sons, 1987, ISBN 0-471-60386-4.

[4] F. Halzen and A. Martin, "Quarks and leptons: An introductory course in modern particle physics,". John Wiley & Sons, 1984, ISBN 0-471-81187-4.

[5] S. Weinberg, "A Model of Leptons," *Phys. Rev. Lett.* **19** (1967) 1264–1266.

[6] "Combination of CDF and DØ Results on the Mass of the Top Quark," `hep-ex/0903.2503`.

[7] C. Amsler *et al.*, "Review of particle physics," *Phys. Lett.* **B667** (2008) 1.

[8] E. Noether, "Invariante Variationsprobleme," *Nachr. D. Knig. Gesellsch. D. Wiss. Zu Gttingen, Math-phys. Klasse* (1918) 235–257.

[9] P. W. Higgs, "Broken symmetries, massless particles and gauge fields," *Phys. Lett.* **12** (1964) 132–133.

[10] P. W. Higgs, "Broken Symmetries and the Masses of Gauge Bosons," *Phys. Rev. Lett.* **13** (1964) 508–509.

[11] P. W. Higgs, "Spontaneous Symmetry Breakdown without Massless Bosons," *Phys. Rev.* **145** (1966) 1156–1163.

[12] "Physics of and with Leptons," `http://www-zeus.physik.uni-bonn.de/~brock/feynman/vtp_ws0506/index.html`.

[13] M. Kobayashi and T. Maskawa, "CP Violation in the Renormalizable Theory of Weak Interaction," *Prog. Theor. Phys.* **49** (1973) 652–657.

[14] L. Wolfenstein, "Parametrization of the Kobayashi-Maskawa Matrix," *Phys. Rev. Lett.* **51** (1983) 1945.

[15] E. Barberio *et al.*, "Averages of $b-$hadron and $c-$hadron Properties at the End of 2007," `hep-ex/0808.1297`.

[16] T. Barnes, "The XYZs of charmonium at BES," *Int. J. Mod. Phys.* **A21** (2006) 5583–5591, `hep-ph/0608103`.

[17] F. Abe *et al.*, "J/ψ and $\psi(2S)$ production in $p\bar{p}$ collisions at $\sqrt{s} = 1.8$ TeV," *Phys. Rev. Lett.* **79** (1997) 572–577.

[18] E. L. Berger and D. L. Jones, "Inelastic Photoproduction of J/ψ and Υ by Gluons," *Phys. Rev.* **D23** (1981) 1521–1530.

[19] R. Baier and R. Ruckl, "Hadronic Production of J/ψ and Υ: Transverse Momentum Distributions," *Phys. Lett.* **B102** (1981) 364.

[20] G. T. Bodwin, E. Braaten, and G. P. Lepage, "Rigorous QCD analysis of inclusive annihilation and production of heavy quarkonium," *Phys. Rev.* **D51** (1995) 1125–1171, `hep-ph/9407339`.

[21] E. V. Shuryak, "The Structure of Hadrons Containing a Heavy Quark," *Phys. Lett.* **B93** (1980) 134–136.

[22] E. V. Shuryak, "Hadrons Containing a Heavy Quark and QCD Sum Rules," *Nucl. Phys.* **B198** (1982) 83.

[23] N. Isgur and M. B. Wise, "Weak Decays of Heavy Mesons in the Static Quark Approximation," *Phys. Lett.* **B232** (1989) 113.

[24] N. Isgur and M. B. Wise, "Weak Transition Form-Factors Between Heavy Mesons," *Phys. Lett.* **B237** (1990) 527.

[25] N. Isgur and M. B. Wise, "Spectroscopy with heavy quark symmetry," *Phys. Rev. Lett.* **66** (1991) 1130–1133.

[26] C.-F. Qiao, "J/ψ pair production at the Tevatron," *Phys. Rev.* **D66** (2002) 057504, hep-ph/0206093.

[27] B. Aubert *et al.*, "Observation of the bottomonium ground state in the decay $\Upsilon_{3S} \to \gamma\eta_b$," *Phys. Rev. Lett.* **101** (2008) 071801, hep-ex/0807.1086.

[28] E. Braaten, S. Fleming, and A. K. Leibovich, "NRQCD analysis of bottomonium production at the Tevatron," *Phys. Rev.* **D63** (2001) 094006, hep-ph/0008091.

[29] G. Hao, Y. Jia, C.-F. Qiao, and P. Sun, "Hunting η_b through radiative decay into J/ψ," *JHEP* **02** (2007) 057, hep-ph/0612173.

[30] The LEP Electroweak Working Group, "A Combination of Preliminary, Electroweak Measurements and Constraints on the Standard Model," http://lepewwg.web.cern.ch/LEPEWWG/plots/winter2009/.

[31] U. Ellwanger, M. Rausch de Traubenberg, and C. A. Savoy, "Phenomenology of supersymmetric models with a singlet," *Nucl. Phys.* **B492** (1997) 21–50, hep-ph/9611251.

[32] V. M. Abazov *et al.*, "Search for NMSSM Higgs bosons in the $h \to aa \to \mu\mu$ $\mu\mu$, $\mu\mu$ $\tau\tau$ channels using $p\overline{p}$ collisions at $\sqrt{s} = 1.96$ TeV," hep-ex/0905.3381.

[33] S. Abachi *et al.*, "Observation of the top quark," *Phys. Rev. Lett.* **74** (1995) 2632–2637, hep-ex/9503003.

[34] FNAL Accelerator Division, "Accelerator concepts," *Rookie Books* http://www-bdnew.fnal.gov/operations/rookie_books/rbooks.html.

[35] "The MiniBooNE Experiment," `http://www-boone.fnal.gov/`.

[36] "The SciBooNE Experiment," `http://www-sciboone.fnal.gov/`.

[37] "The NuMI Experiment," `http://www-numi.fnal.gov/`.

[38] J. Marriner, "Stochastic cooling overview," *Nucl. Instrum. Meth.* **A532** (2004) 11–18.

[39] I. Meshkov and A. Sidorin, "Electron cooling," *Nucl. Instrum. Meth.* **A532** (2004) 19–25.

[40] FNAL Accelerator Division, "Run II Parameter List," `http://www-bdnew.fnal.gov/runII/parameters.pdf`.

[41] FNAL Accelerator Division, "Collider Run II Peak Luminosity," `http://www-bdnew.fnal.gov/operations/lum/lum.html`.

[42] FNAL Accelerator Division, "Collider Run II Integrated Luminosity," `http://www-bdnew.fnal.gov/operations/lum/lum.html`.

[43] V. M. Abazov *et al.*, "The Upgraded DØ Detector," *Nucl. Instrum. Meth.* **A565** (2006) 463–537, `physics/0507191`.

[44] A. Evdokimov, "Tracking and Preshower Detectors," Talk given to the DØ collaboration, June 2009.

[45] S. Abachi *et al.*, "Beam tests of the DØ uranium liquid argon end calorimeters," *Nucl. Instrum. Meth.* **A324** (1993) 53–76.

[46] A. Ito, "DØ Muon System," Talk given to the DØ collaboration, June 2009.

[47] V. M. Abazov *et al.*, "Run IIb upgrade technical design report," FERMILAB-PUB-02-327-E.

[48] DØ Layer 0 Silicon Group, "DØ Layer 0 Conceptual Design Report," DØ Note 4415.

[49] M. S. Weber, "A new inner layer silicon micro-strip detector for DØ," *Nucl. Instrum. Meth.* **A566** (2006) 182–184.

[50] M. Abolins *et al.*, "The run IIb trigger upgrade for the DØ experiment," *IEEE Trans. Nucl. Sci.* **51** (2004) 340–344.

[51] M. Abolins *et al.*, "Design and Implementation of the New DØ Level-1 Calorimeter Trigger," *Nucl. Instrum. Meth.* **A584** (2008) 75–97, `arXiv/0709.3750`.

[52] D. Smirnov, "Status of the DØ fiber tracker and preshower detectors," *Nucl. Instrum. Meth.* **A598** (2009) 94–97.

[53] D. Whiteson, "Global track finding at Level 3," DØ Note 3808.

[54] Level 3 CFT unpacking tool, `http://www-d0.fnal.gov/d0dist/dist/packages/l3fcftunpack/`.

[55] R. A. Illingworth, "Development of trigger software for the silicon and fibre trackers and a study of B meson lifetimes for the DØ experiment," (2002), FERMILAB-THESIS-2002-59.

[56] P. Hough, "Machine Analysis of Bubble Chamber Pictures," *International Conference on High Energy Accelerators and Instrumentation* (1959) p554–559.

[57] A. Khanov, "HTF: Histogramming Method for Finding Tracks. The Algorithm Description," DØ Note 3778.

[58] D0reco reconstruction package, `http://www-d0.fnal.gov/computing/algorithms/howto/howtoreco.html`.

[59] G. Borrisov, "Technical Details of AA Tracking," Talk given at DØ tracking workshop, 6th December 2005.

[60] H. Greenlee, "The DØ Interacting Propagator," DØ Note 4293.

[61] H. Greenlee, "The DØ Kalman Track Fit," DØ Note 4303.

[62] Level 3 Impact Parameter Jet B-tag page, `http://www-d0.fnal.gov/computing/algorithms/level3/b-tagging/L3Btag.html`.

[63] C. P. Barnes, "Development of vertexing and lifetime triggers and a study of B_s mixing using hadronic decays at DØ," (2005), FERMILAB-THESIS-2005-19.

[64] Level 3 tracking analysis tool, `http://www-d0.fnal.gov/d0dist/dist/packages/l3ftrack_analysis/`.

[65] Level 3 jet tool documentation, `http://www-d0.fnal.gov/computing/algorithms/level3/jets/L3TJet_overview.html`.

[66] T. P. Scanlon, "B^- tagging and the search for neutral supersymmetric Higgs bosons at DØ," (2006), FERMILAB-THESIS-2006-43.

[67] C. Buszello, "Study of possible enhancements of the L3 global tracker," DØ Note 4636.

[68] R. Beuselinck, "The Run IIb Level 3 Tracking Tool," DØ Note 5452.

[69] D. Bloch, "Performance of the JLIP b-tagger in p14," DØ Note 4348.

[70] M. Sanders, "Beam Position Monitoring in Real Time," DØ Note 4755.

[71] T. Sjostrand, L. Lonnblad, S. Mrenna, and P. Skands, "Pythia 6.3 physics and manual," `hep-ph/0308153`.

[72] E. Barberis *et al.*, "Summary of modifications to the SMT software readout/geometry," DØ Note 3780.

[73] D. Bauer and R. Illingworth, "L3 Trigger: Clustering in the SMT," DØ Note 3822.

[74] T. Christoudias, "Search for the Standard Model Higgs boson in the missing energy Topology with DØ," (2009), FERMILAB-THESIS-2009-32.

[75] BANA Analysis Suite, `http://www-d0.fnal.gov/Run2Physics/ckm/d0_private/bgv/aa/bana.htm`.

[76] C. Buszello, "Properties of J/ψ pairs," Talk given at B-physics group meeting, April 2006.

[77] D. J. Lange, "The EvtGen particle decay simulation package," *Nucl. Instrum. Meth.* **A462** (2001) 152–155.

[78] J. J. Aubert *et al.*, "Experimental Observation of a Heavy Particle J," *Phys. Rev. Lett.* **33** (1974) 1404–1406.

[79] J. E. Augustin *et al.*, "Discovery of a Narrow Resonance in e^+e^- Annihilation," *Phys. Rev. Lett.* **33** (1974) 1406–1408.

[80] S. W. Herb *et al.*, "Observation of a dimuon resonance at 9.5-GeV in 400-GeV proton - nucleus collisions," *Phys. Rev. Lett.* **39** (1977) 252–255.

[81] P. Calfayan *et al.*, "Muon Identification Certification for p17 data," DØ Note 5157.

[82] V. M. Abazov *et al.*, "Observation of ZZ production in $p\bar{p}$ collisions at $\sqrt{s} =$ 1.96-TeV," *Phys. Rev. Lett.* **101** (2008) 171803, `hep-ex/0808.0703`.

[83] C. Jarvis, N. Hadley, and M. Sanders, "A search for $p\overline{p} \to ZZ \to l^+l^-l'^+l'^-$," DØ Note 5081.

[84] V. M. Abazov *et al.*, "Direct observation of the strange b baryon Ξ_b^-," *Phys. Rev. Lett.* **99** (2007) 052001, `hep-ex/0706.1690`.

[85] DØ Collaboration, "Reconstruction of B hadron signals at DØ," DØ Note 4481.

[86] C.-F. Qiao, L.-P. Sun, and P. Sun, "Testing Charmonium Production Mechanism via Polarized J/ψ Pair Production at the LHC," `hep-ph/0903.0954`.